Best Practice Document

Purpose

A document describing the "best practices" in the diagnosing and monitoring of convective storms using satellite remote sensing, with an emphasis on the use of geostationary satellites, specifically Meteosat Second Generation

For EUMETSAT Convection Working Group

Editors

John Mecikalski
Kristopher Bedka
Marianne König

Version 2.0 of 01 July 2012

Abstract

This document describes satellite based nowcasting methods, as they are presented and discussed in the framework of the EUMETSAT – ESSL Convection Working Group.

The nowcasting applications range from describing the pre-convective atmosphere to the early detection of growing Cumulus clouds and to fully developed convective storms, here focusing on the storm top signatures.

Contents

LIST OF ACRONYMS

ABI	Advanced Baseline Imager
ATBD	Algorithm Theoretical Basis Document
AVHRR	Advanced Very High Resolution Radiometer
BT	Brightness Temperature
BTD	Brightness Temperature Difference
CAPE	Convective Available Potential Energy
CbTRAM	CumulonimBus TRacking And Monitoring
COALITION	Context and Scale Oriented Thunderstorm Satellite Predictors Development
CI	Convective Initiation
CII	Combined Instability Index
DLR	Deutsches Zentrum fur Luft- und Raumfahrt
EUMETSAT	European Organization for the Exploitation of Meteorological Satellites
FAA	United States Federal Aviation Administration
GEO	Geostationary
GLM	NOAA GOES-R Series Geostationary Lightning Mapper
GOES	Geostationary Operational Environmental Satellite
HRV	High Resolution Visible
IF	Interest Field
IR	Infrared
IRS	Meteosat Third Generation Infrared Sounder
IRW	~11 μm Infrared Window Channel
LEO	Low Earth (i.e. Polar) Orbiting
LI	Lifted Index
MCS	Mesoscale Convective System
MODIS	Moderate Resolution Imaging Spectroradiometer
MPEF	Meteorological Product Extraction Facility
MTG	Meteosat Third Generation
NASA	National Aeronautic and Space Administration
NLDN	National Lightning Detection Network
NOAA	National Oceanographic and Atmospheric Administration
NPP	NPOESS Preparatory Project
NWP	Numerical Weather Prediction
NWC-SAF	EUMETSAT Satellite Application Facility in Support to Nowcasting and very Short Term Forecasting
RDT	NWCSAF Rapidly Developing Thunderstorms Algorithm
SAWS	South African Weather Service
SEVIRI	Spinning Enhanced Visible and Infra-Red Imager
OT	Overshooting Top
TPW	Total Precipitable Water
TRMM	Tropical Rainfall Measurement Mission
UTLS	Upper Tropophere / Lower Stratosphere
VIS	~0.6 μm Visible channel
WV	Water Vapour absorption channel in the 6 to 7 μm region

1 INTRODUCTION

The term "pre-convective environment" refers to the 4-D thermodynamic and wind field present before convective initiation (CI) occurs. Multispectral satellite radiances can be used in combination with temperature and moisture profiles from a NWP model to provide an estimate of convective instability and moisture availability in near-real time, which is a significant advantage over 12-hour resolution and often coarsely spaced rawinsonde profiles. A combination of WV imagery, satellite-derived winds, and NWP model wind forecasts can be used to identify jet stream wind speed and vorticity maxima and regions with upper level divergence and low level convergence, which are key forcing mechanisms for convective storms. A forecaster can use these methods to estimate locations of future convective development and potential storm severity with a 6+ hour lead-time.

The term "convective initiation" refers to the process where an existing cumulus cloud begins rapid vertical growth. During the CI process, a convective cloud top cools and eventually glaciates. Precipitation is often first detected by ground based weather radar somewhere within the cloud when this glaciation occurs. A variety of methods have been recently developed to objectively identify convective clouds, derived cloud-top time trends, and make CI nowcasts using time sequences of multispectral imagery. The definition of CI has been largely based on observations from other ground-based instrumentation such as the first detection of a 35 dBZ radar echo from S-band weather radar, or the first occurrence of lightning at the surface or somewhere within the cloud. Depending on the data source used to define CI and the vigour of convective development, existing methods have been shown to offer up to a 90-minute CI nowcast lead-time.

The term "mature convective storm" refers to an individual or organized cluster of convective clouds with tops at or above their local equilibrium level. They can range in size and organization from a single air-mass thunderstorm to a mesoscale convective system. Mature convective storms feature a region of strong vertical motions or "updrafts" that advect ice hydrometeors into the upper troposphere and lower stratosphere (UTLS). Convectively induced momentum and the prevailing jet stream wind transports hydrometeors laterally in the tropopause region, producing a cirrus "anvil" cloud.

A thorough review of the literature in conjunction with experiences of the EUMETSAT - ESSL Convection Working group suggest the practices described in this document for using geostationary imaging satellite data to diagnose and nowcast convection.

It should be noted, however, that satellite data alone do not provide sufficient information to develop and derive many of the methods/products described here. Ancillary data from numerical weather prediction (NWP) models, surface type models (notably surface emissivity maps) are needed for many of the described processes, together with assumptions on the radiative transfer in the atmosphere or on cloud microphysical properties.

Though the literature shows that satellite imagery and derived products clearly add value to the convective storm nowcast process, satellite offers only one of many datasets a forecaster should use to make nowcast decisions. NWP output, surface METAR observations, rawinsonde profiles, ground-based weather radar, lightning detections, ground-based vertical profiling instrumentation all have a significant role during some phase of the nowcast process.

Signatures in the visible and infrared channel imagery provide indications that a storm is severe and/or hazardous for aviation interests. The term "severe" will be used to describe a storm that produces high winds (>25 ms^{-1}), large hail (> 2 cm), or tornadoes, which is a common definition used within the European Severe Weather Database (ESWD) and NOAA Storm Prediction Center storm reports. Some studies in the peer-reviewed and conference literature also describe storms that produce heavy rainfall as "severe." This will not be used to define a severe storm in this document since heavy rainfall can be also produced by slow moving, long-duration stratiform or slantwise-convective events.

2   PRE-CONVECTIVE ENVIRONMENT: WHERE WILL STORMS FORM, HOW DO WE OPTIMALLY USE SATELLITE AND NWP?

2.1   Introcuction

Forecasting for the first 12 h requires extensive use of remote sensing tools including radar, lightning networks and satellite. Operational forecasters need easy, simple ways to integrate all relevant data to make very short-range forecasts and nowcasts of convective activity.

Quantitative assessment of instability and vertical displacements of the air mass for diagnosis of pre-convective environment has been applied by using satellite derived instability indices from GOES data were reported by Rao and Fuelberg (1997). For Meteosat Second Generation (MSG), a similar method exists and is described in Koenig and de Coning (2009). The air mass parameters can be used to issue severe weather warnings if the corresponding index exceeds a certain threshold. These thresholds are usually determined empirically and should not be regarded as fixed values – they may vary from season to season and from region to region. A skilled local forecaster is absolutely necessary for a correct interpretation of the provided indices.

2.2   The MSG Global Instability Index (GII) Product

Despite the role that numerical weather prediction models play to give general guidance on where favorable conditions are found for the onset of convection, more detailed information on the exact location and severity of convective storms is needed. If model and satellite data can be combined it will offer greater spatial as well as temporal guidance closer to the time of convective activity. In addition, the satellite derived instability fields can point at areas where the numerical model forecasts do not well capture the actual developments, e.g. the instability product may show different gradients and/or different intensities of instability. One way of achieving this is through the Global Instability Indices (GII) product, where MSG fields and model fields are combined into one product to provide instability indices, independent of upper air sounding sites (Koenig and de Coning, 2009). The GII product specifically provides the instability indices "Lifted Index" and K-Index", together with the total precipitable water and the precipitable water content in three layers, defined as

T	: air temperature at the indiciated pressure level (500, 700, 850 hPa)
TD	: dew point temperature at the indicated levels
TPW	: total precipitable water
LPW	: layer precipitable water
q(z)	: humidity at height level z
sfc:	: surface
toa:	: top of atmosphere
level 1,2	: level boundaries for the layer precipitable water

$T^{\text{lifted from surface}}$ in the definition for the Lifted Index referes to the temperature an air parcel would have if it were lifted from the surface (usually taken as lowest 100 hPa) to 500 hPa

An air mass is usually identified as unstable if the Lifted Index is negative and if the K-Index exceeds ~20°C.
The LPW values are provided for the lower layer (surface – 850 hPa), the middle layer (850 – 400 hPa) and the upper atmospheric layer (above 400 hPa).

Figure 2.2-1 shows the Lifted Index, the K-Index and the Total Precipitable Water product for the entire MSG field of view. The data is available in real-time, every 15 minutes, averaged over 3×3 MSG pixels. For the MSG rapid scan service (covering Europe every 5 minutes), the same product is available on a pixel resolution, every 5 minutes.
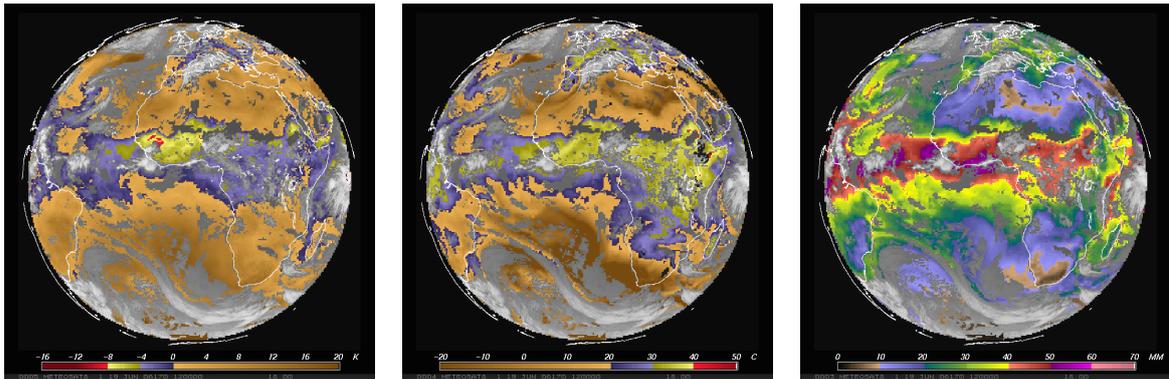
Figure 2.2-1: Full disk view of the MSG product Lifted Index (left), K-Index (centre) and Total Precipitable Water. Grey levels indicate the presence of clouds where no product could be retrieved.

These types of retrievals of instability and air mass parameters have been used operationally since 1988 using first the GOES VISSR Atmospheric Sounder (VAS) instrument and later the GOES Sounder (Hayden, 1988; Huang *et al*., 1992; Rao and Fuelberg, 1997; Menzel et al., 1998; Dostalek and Schmit, 2001; Schmit et al., 2002). The basic principle of such retrievals is that the additional information content of the satellite (infrared) measurements is used to locally change the NWP profiles, especially concerning low level moist
ure (inferred from the split window channels), and mid- and upper level moisture (using water vapour channels), together with the surface skin temperature (using a window channel). Figure 2.2-2 and Figure 2.2-3 show examples of how forecasts can be changed when combined with the real-time satellite observations.
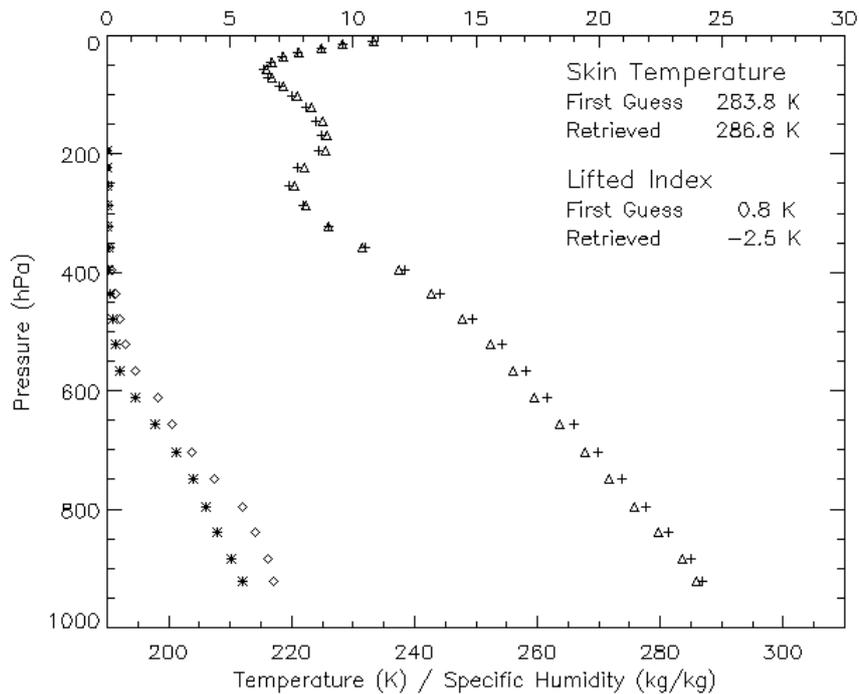
Figure 2.2-2: Example of a forecasted temperature (Δ) and humidity (∗) profile, and how it was changed after combined with the satellite observations (◊ and +, resp.). The legend in the top right shows how the surface skin temperature was changed from 283.8K to 286.8K, and how the Lifted Index was changed from a forecasts stable value of +0.8 K to unstable conditions of -2.5K.
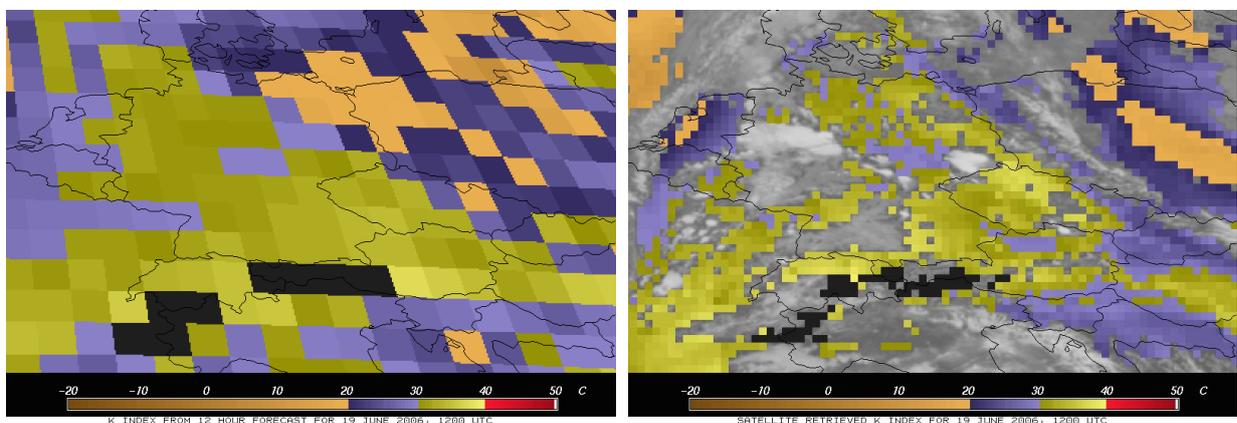
Figure 2.2-3: Example of how the MSG instability retrieval changed the forecasted values: The left panel shows the K-Index, as forecasted by ECMWF (12 hour forecast), on the 1 deg latitude/longitude grid. The right panel shows how this forecast was changed by the additional satellite information: The zone of high K-Index values (> 30°C) extended considerably further east than forecasted, into East Germany and western Poland. In this particular case, the MSG retrievals were well supported by the local radiosoundings.

The greatest advantage of these fields is the added capability of the nearly continuous monitoring of the instability fields guaranteed by the MSG 15 min repeat cycle. This provides forecasters with new information much more frequently than the twice-daily soundings at only a limited number of radiosonde stations. The instability product is aimed at helping forecasters to focus their attention on a particular region, which can then be

9

monitored more closely by other means such as satellite imagery and/or radar data. The indices can only assess the likelihood of convection within the next few hours, and should be seen in combination with measures of other triggering and/or lifting mechanisms. Another advantage is that such a product can also be used in data sparse regions over Africa where upper air ascents are not always available.

2.3   The SEVIRI Physical Retrieval (SPhR) Product of the NWC-SAF

The SEVIRI Physical Retrieval (SPhR) product has been developed within the NWC SAF context aiming to support Nowcasting applications. It is based in the code provided by CIMSS at the University of Wisconsin-Madison.

The aim of the SPhR is to provide information on the water vapour in a vertical column of unit cross-section area in several layers in the troposphere and to provide some instability indices. These parameters are calculated from the retrieved profiles of temperature and humidity. The SPhR algorithm performs the physical retrieval of the atmospheric temperature and moisture profiles as well as the surface skin temperature for one clear sky SEVIRI pixel, or a configurable Field-Of-Regard (FOR) containing M x M pixels. The main outputs are:
  • Total Precipitable Water (TPW): Surface Pressure - Top of atmosphere
  • Boundary Layer Precipitable Water (BL): Surface Pressure hPa - 850 hPa
  • Middle Layer Precipitable Water (ML): 850 hPa -500hPa
  • High Layer Precipitable Water (HL): 500 hPa -Top of atmosphere
  • Lifted Index (LI)
  • Showalter Index (SHW)
  • K-Index (KI)

Besides the main outputs, the differences between TPW, BL, ML, HL, LI, SHW and KI parameters calculated with the retrieved profiles of temperature and humidity and the ones calculated from the background NWP (after the spatial, temporal and vertical interpolation to SEVIRI) profiles are also written in the SPhR HDF-5 file.

Due to the fact that SPhR is run locally and in order to allow users to debug their local installations or generate new parameters or instability indices, the temperature and specific humidity profiles can be written in SPhR binary files if users desire. The main advantage is the spatial, temporal and vertical collocation of these (T, q) profiles allowing debugging activities, vertical cross sections, 3D visualizations, and generation of validation datasets among other applications.

SPhR products are only available over "clear" FORs and due to it is an iterative physical retrieval, computation is relative expensive and an increase in the width of the FOR could be necessary in large region processing. The SPhR software has been designed to be able to process in real time any region defined by the user inside the MSG Full Disk and to be able to run at pixel by pixel scale, specially in the case of processing a small region. But due to this is a very demanding CPU process and there is more products in the NWC SAF packages, in the default SPhR configuration file the width of the FOR is 3. For large regions the users can easily change the width of the FOR that is a configurable parameter in the ASCII PGE13 Model Configuration File and they can also adjust some key parameters.

The SPhR product has been validated over the MSG Full Disk. The whole validation can be found in the PGE13 SPhR Validation Report on the NWC SAF web page. The best improvements with the SPhR algorithm are obtained on humidity profiles over mid and upper levels. Due to limitations in the NWC SAF library, current version only allows the use of background NWP on fixed pressure level but as a main improvement SPhR will allow using NWP with better vertical resolution on hybrid levels GRIB files on CDOP-2 phase. Thus, improvements in vertical and horizontal resolution in the background NWP information will allow improvements in the SPhR product and in the monitoring of precipitable water and instability regions. Figure 2.3-1 shows an example of the SPhR output.

The product is locally obtained a short time after the SEVIRI image is available and it can be obtained operationally every 15 minutes (or 5 minutes in case of Rapid Scan mode). The intensity and temporal change in the magnitude of the SPhR fields can be key information to establish the severity on the convection that will be triggered later when the clouds begin, so the possibility of creating loops in real time with the SPhR outputs allows the monitoring of key ingredients in pre-convective environments before cloudiness is developed.

The differences with the NWP background allow monitoring the added value of SPhR algorithm and delimiting regions that will require special attention by the forecaster. Thus, the better the vertical and horizontal resolutions in the background NWP is used, the better humid and unstable regions will be delimitated. The option to save the profiles allows the calculation of other instability parameters and with an adequate software monitoring, humidity and unstable regions in 2D or 3D.

The NWP model provides the surface pressure used in the SPhR. The better resolution the surface pressure field is, the lower the error will be. The emissivity is fixed from IREMIS dataset. Over mountain regions with large difference between the topography and the NWP topography, the result can exhibit large errors. The same happens in desert pixels, where the distance on skin temperature between the NWP first guess and the actual skin temperature could be high. Similar behaviour is expected on very hot or cold pixels over non-desert land pixels. In this case our experience when the change in the supply of the background NWP from ECMWF every 6 hours from t+00 to t+24 with 0.5°x0.5° resolution has been changed to ECMWF every 3 hours from t+00 to t+24 with 0.125°x0.125° resolution has improved clearly the quality of the PGE13 SPhR outputs. The following improvement should be change from 15 pressure levels GRIB to 91 hybrid levels GRIB (as example it is foreseen that ECMWF will increase the number of hybrid level to 144). In general, a more accurate background profile will lead to a more accurate retrieval.
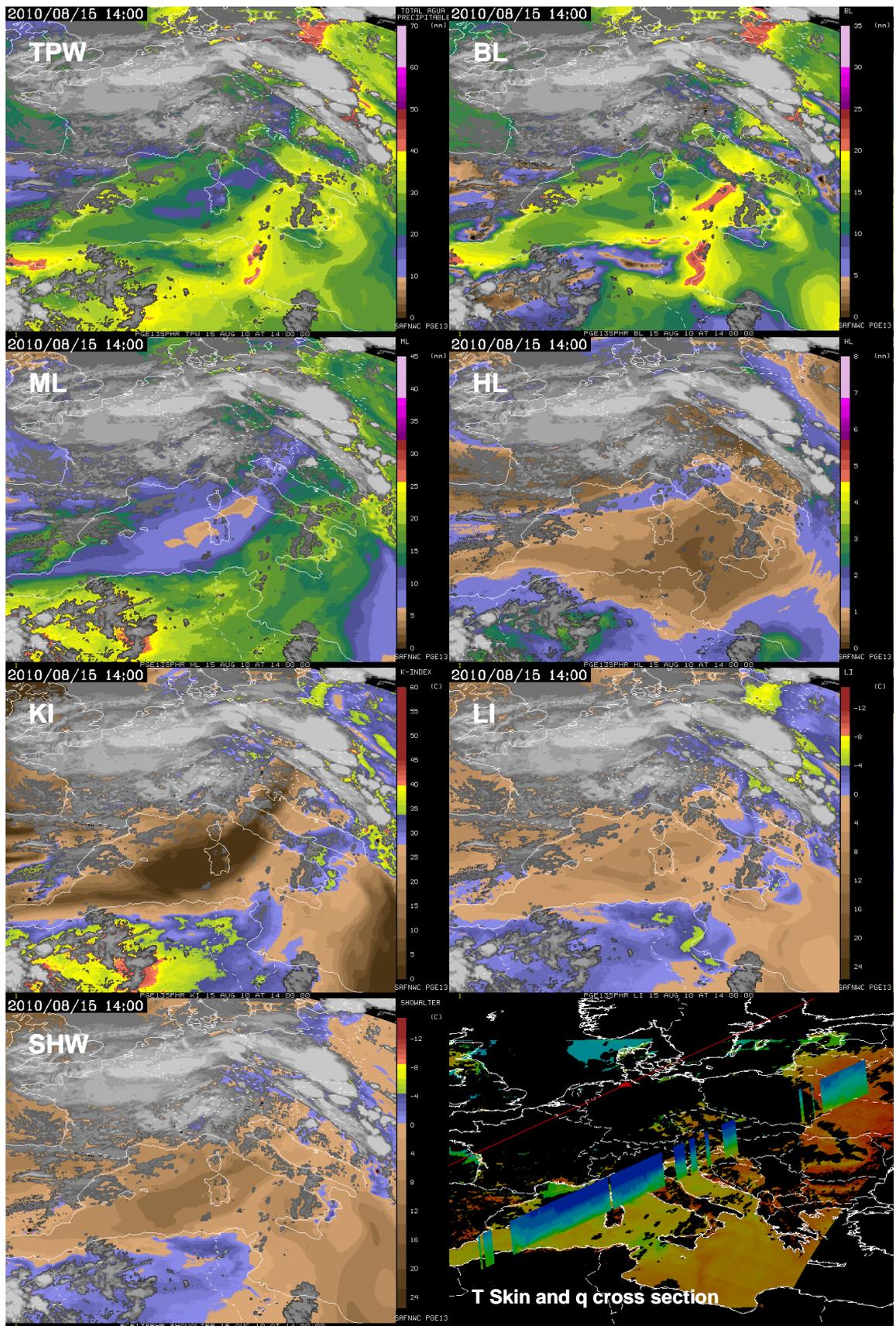
Figure 2.3-1: SPhR outputs and T Skin and q cross-section at 1400 UTC for the storms of 15th August over central Europe.

2.4   Combined Instability Index (CII) Work Performed at SAWS

A local version of the GII code was installed at the South African Weather Service (SAWS) in September 2007. A local mesoscale model (the local version of the Met Office Unified Model) with a 0.1° latitude/longitude resolution is used for this local processing, allowing for a configurable number of pixels and allowing the calculation of other indices, e.g. the Mixed K-Index or the Mixed Total Totals, as defined by

T   : air temperature at the indiciated pressure level (500, 700, 850 hPa)
TD   : dew point temperature at the indicated levels

Mixed Total Totals / Mixed K Index:
T850 (TD850) in the equations are substituted by the average
temperature (dew point) between the surface and 825 hPa to account
for high terrain

This local version of the GII is called the Regional Instability Indices (RII). The RII product does not cover the entire MSG footprint, but only the domain of the Unified Model run in South Africa – i.e. southern Africa and adjacent ocean areas (Figure 2.4-1).
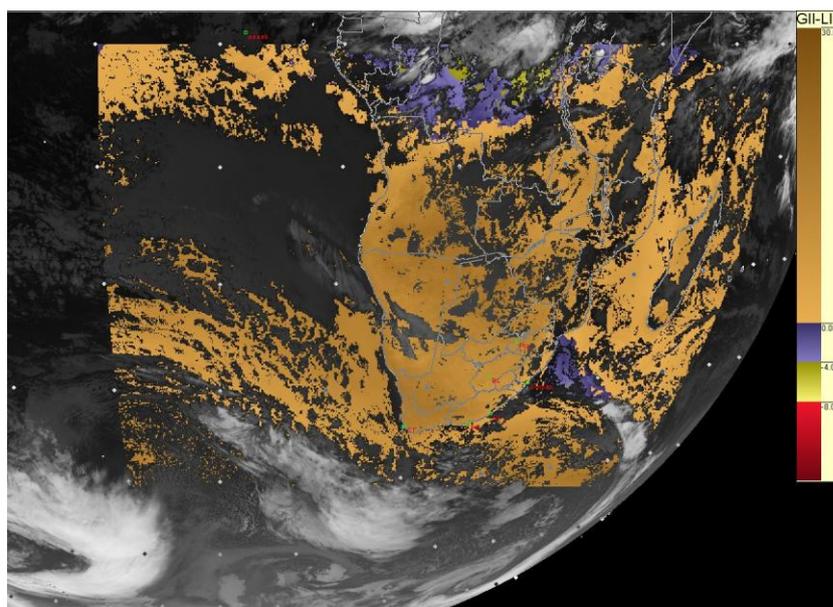
Figure 2.4-1: Visualisation of the South African RII Lifted index with the MSG IR channel as background image, depicting the processing domain.

A quantitative evaluation method has been developed in South Africa to show the forecast/nowcast capability of the RII parameters when compared to the occurrence of lightning over the country. A contingency table approach (Wilks, 2005) was used to calculate the Probability of Detection (POD), False Alarm Ratio (FAR), Probability of False Detection (POFD) and Hanssen−Kuipers discriminant (HK) for Mixed K index, Mixed Total Totals, Lifted Index as well as Total Precipitable Water for 50 selected cases in the summers of 2007/2008 and 2008/2009, finding a POD of 75-80% and a FAR of 30-35%.

13

In working towards the aim of a single probability map for convection, the occurrence of lightning was chosen as a way to evaluate the RII, it was used as a stepping-stone in the combination of four individual parameters: (Lited Index, Mixed K-Index, Mixed Total Totals Index, Total Precipitable Water). The frequency of lightning occurrence was thus calculated for values of each of the individual indices. For each index, the time average between the 0600 and 0900 UTC fields was found for each of the 50 case study days. This was compared to the occurrence of lightning between 1200 and 2100 UTC later in the same day. The results of these calculations are given in terms of cumulative frequency, i.e. the frequency of lightning occurrence for all the values of the RII below a particular threshold. A combination involving the cumulative frequencies of lightning related to some combination of the four indices, rather than the indices themselves, allows the final "index" to be expressed in terms of percentage probability

Topographic effects were included by creating another look-up table between location altitude and observed lightning, thus relating topography to the probability of lightning occurrence.

All these tables set the scene to combine the four indices and topography into one parameter. A performance related weight was assigned to the individual parameters in the combination process. Since the HK discriminates how well the 'yes' events are distinguished from the 'no' events, it is a good choice as weighting factor. Together with the cumulative frequency values for all meaningful values of each index, the HK value for that value is taken into account as a weighting factor.

The Combined Instability Index (CII) was then defined as an 80% contribution by the lightning frequencies of the four indices and a 20% contribution by those related to topography. The 80 and 20% division is merely due to the five factors that are considered. The contribution related to each value of each individual index is the product of its cumulative frequency value and its ability to distinguish the 'yes' and 'no' events through the Hanssen–Kuipers discriminator (de Coning et al. 2010).

One aspect that is not embedded into the CII is the movement of weather systems. It is acknowledged that storm motion plays a role in very short range forecasting; however, it falls outside the purpose of the development of the CII.

Table 2.4-1 summarises the advantages and limitations of the CII approach. Figure 2.4-2 shows an example of the four individual indices and the combined CII.

| Advantages	Limitations
A single probabilistic map combines instability, moisture and orographic lift into one parameter. There is no need to consider four different parameters each with their own respective thresholds.	The CII can only be calculated in cloud free conditions. Real time radar and satellite images should be used to determine the characteristics of clouds once development has started.
More than 3 h lead-time for convection and/or lightning activity is provided	The CII is a tool developed through the South African summer months (October to March) with the aim to predict convection. It is not intended to be used for stratiform rain and has not been tested for early spring (August and September) conditions.
The CII incorporates an instability measure (MK, MT and LI), moisture (Precipitable Water) as well as topographic enhancement as a lifting mechanism and thus has the required ingredients for convection (excluding dynamic lift).	The CII could be evaluated against the occurrence of lightning over South Africa only due to a lack of lightning observations over the rest of southern Africa. Lightning characteristics in other countries might be different. Nevertheless, visual comparison of the CII to convective development in southern Africa looks promising (using satellite imagery).
The statistics for the CII outperform the individual parameters in spite of the fact that lightning sometimes occurs in areas where CII could not be calculated due to cloud cover.	The evaluation of the CII (or any other parameter) against precipitation remains problematic since neither gauges, nor radar rainfall, nor satellite based precipitation estimates offer a complete and absolute reflection of convective precipitation on the ground.
CII can be displayed operationally every 15 min, as can the MSG images, through free software developed in-house in the SAWS. CII thus vastly improves on the availability and spread of upper air sounding sites when forecasters need to make a forecast of convection when the sky is still clear.	
In South Africa the day often starts with very little clouds and convection only develops later in the day when the surface heats up. Thus, CII can be used on many summer days. If most of the country is cloud free in the morning, the CII helps to delineate the areas with possibilities for convection from those where it will not happen. Once the clouds are present, the CII of the surrounding pixels together with satellite and radar images should be used in real time to monitor the development and decay of convection.	

Table 2.4-1: CII Summary

Figure 2.4-2: Example of three individual parameters (Total Precipitable Water, top left, K-Index, top right, Lifted Index, bottom left) and the Combined instability Index CII (bottom right), providing a percentage probability of lightning occurrence.

2.5 Forward (Temporally) Advection of Layer Averaged Fields: NearCasts

One method that has been used to nowcast conditions for thunderstorm development has involved transporting satellite-derived moisture and temperature fields over 1-6 hour timeframes to assess how stability patterns change and relate to new convective storm development. The objective of these "NearCasts" is to use information from current and future geostationary satellites to not only observe but to predict pre-convective environments conducive for hard-to-forecast, isolated convection 1-9 hours in advance. The method described here is that by Petersen et al. (2010). Wind data, as provided by a model forecast, are interpolated to locations of successful retrievals at multiple levels in the atmosphere. In a next step, these high-definition data are moved in a Lagrangian sense to future locations, using dynamically changing winds (taken from a numerical forecast) for 10 minute time steps. These new locations and their associated profile information are then gridded back to the satellite viewing geometry to produce "predicted" information on a variety of layer moisture and multi-layer stability parameters. A combination of subsequent satellite products and their respective transported values populate initially data void regions, i.e. where clouds obstructed the product processing.

This method is based on the meteorological quantities that GOES/MSG observe best, which include vertical and small-scale horizontal moisture variations, and to detect areas where convective instability develops. The equivalent potential temperature θ_E combines the

multi-layer moisture and temperature observations, from which convective instability can be defined as where

$$\Delta\theta_E/\Delta z \; < \; 0$$

θ_E: equivalent potential temperature
z: height coordinate

i.e. storms can be maintained. This requires areas where temperature lapse rate is weak and Precipitable Water (PW) decreases with height

$$\Delta PW/\Delta z \; < \; 0$$

The value of using data from multiple observation times is shown in Figure 2.5-1, prior to a major tornado outbreak in Oklahoma and Texas on 24/25 May 2011. The top panel shows the coverage of GOES retrievals from only one observation time (1300 UTC). Note particularly the data gap (dark area) over central Oklahoma and Texas in this of lower tropospheric PW analysis. When these observations are moved forward in time and combined with other successive observations taken hourly thereafter (and also projected forward, but for successively shorter periods of times, all valid at the same time), the accumulated number of data points available by 2200 UTC is approximately 10 times greater than that present at 1300 UTC alon. The combination of on-time data and multiple hours of projections of previous observations forward in space has (1) filled most of the data gaps present in the single-data-time displays (lower panel), and (2) provided redundancy and improved confidence in the clear regions of the analyses. It should be noted that at 2200 UTC, a major south-to-north line of convection had developed across Oklahoma extending into north-central Texas, exactly at the location of the moisture masimum shown in the lower panel. More importantly, if the NearCast analyses were not available and only on-time GOES data had been available to forecasters, no PW information would have been available in the area of thunderstorms due to the presence of clouds, obscuring the IR observations.

In addition to increasing areal data coverage in analyses, Figure 2.5-2 illustrates the value of the short-range NearCast predictions of areas likely to become either more or less likely to support convection. NearCasts (especially lower-level transport and stability tendencies) are especially useful for diagnosing initial storm growth and coverage. NearCasts also add significantly to the value of NWP guidance in helping determine where convection *will and will not* occur. This was the case for the 24-25 May case, where initial severe storm development occurred over central Oklahoma in late afternoon, followed by long-lived storms over Dallas, Texas in the early evening. By contrast, no convection was observed in the northeastern U.S. between Chicago Illinois and New York, although guidance showed a threat for storms in this area that affected aviation forecasts there, as susggested by the inset in the upper panel.
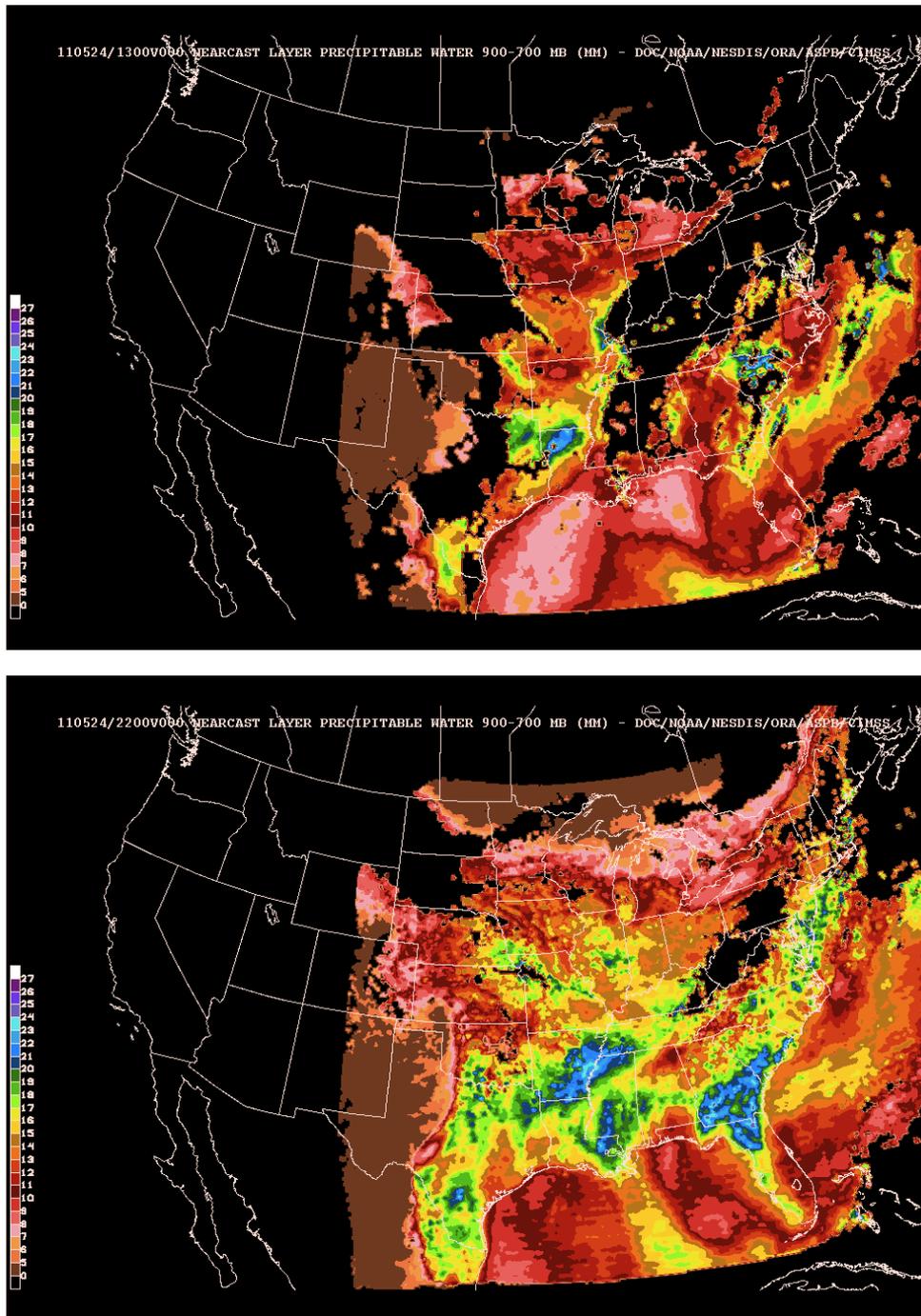
Figure 2.5-1: Illustration of the NearCast process: An individual retrieval of stability parameters (here: total precipitable water) for a given satellite observations shows large data void areas because of the presence of clouds. The top panel illustrates the product for 24 May 2011, 1300 UTC, retrieved from the GOES sounder observations. New observations are merged with trajectories of past data, thus populating the data sparse regions. The lower panel shows the merged product for all observations between 1300 and 2200 UTC.
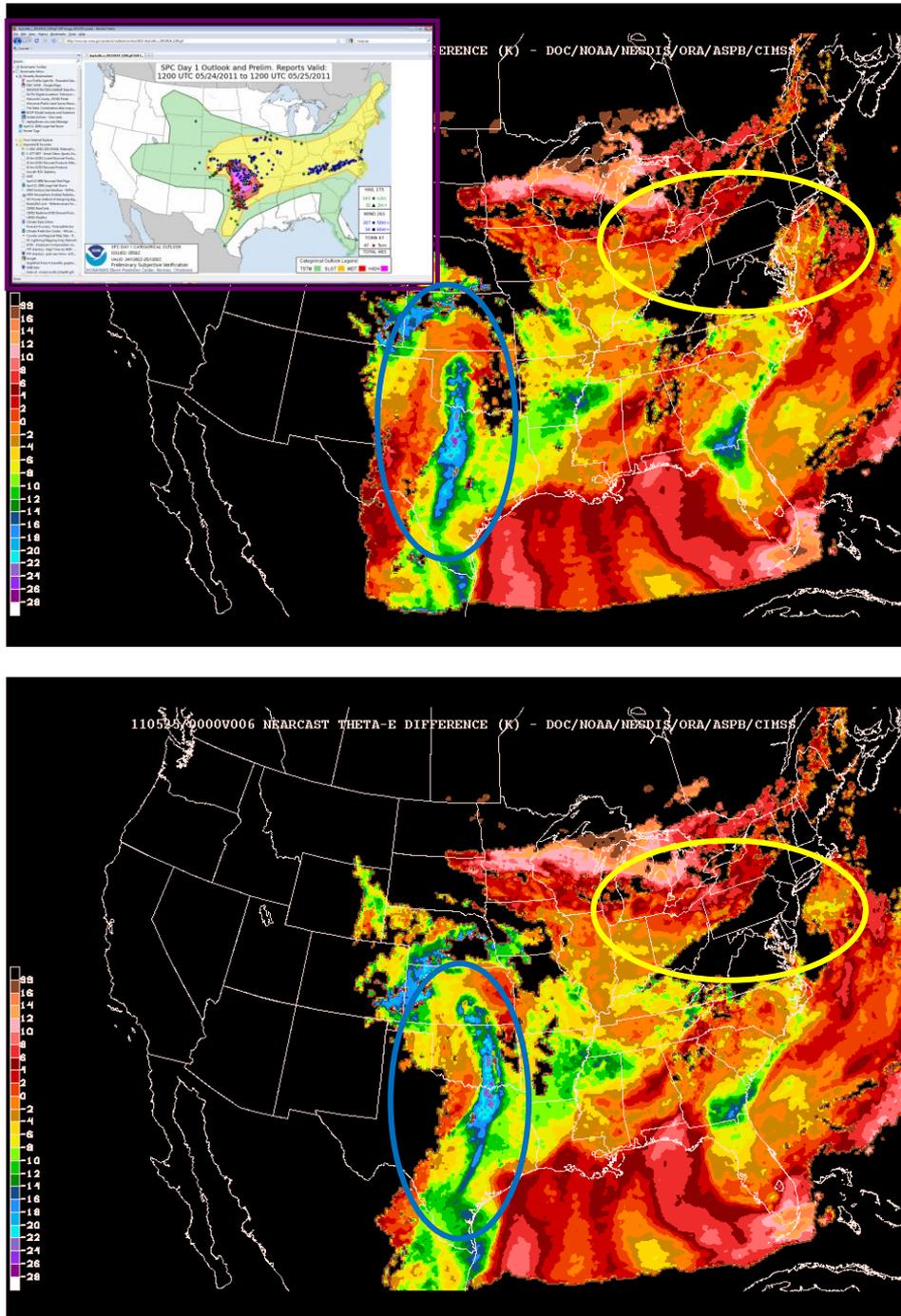
Figure 2.5-2: Storm outlook and observed events for 24 / 25 May 2011 (top panel inset), and 2 and 6 hours NearCasts based on the GOES Sounder data valid at 2000 UTC on 24 May (top) and 0000 UTC on 25 May, respectively. The NearCast shows the eastward motion and slight intensification of instability (in north-eastern Texas, blue circle) and the southward motion of stable air from the Great Lakes into Pennsylvania (yellow circle).

The NearCast products were developed to take advantage of the parameters that GOES observes best (e.g., 2-3 deep layers of moisture). Adding temperature data to produce θ_E improved further upon the moisture-only products and provided the basis for calculating Convective Instability as the difference in θ_E for a deep layer between the lower- and middle-troposphere. The choice of this parameter was consistent with many years of observations that convection tended to form along the trailing and especially leading edges of dry bands observed in water-vapor imagery. Although Convective Instability is unfamiliar to some forecasters, it is very similar to Lifted Index.

In the top panel of this example, a well-defined line of convectively unstable air was forecast to extend in a south-to-north arc across Oklahoma at 2000 UTC. In the next 4 hours (bottom panel), this line of weakest stability was predicted to move eastward while intensifying along its southern end, near Dallas. By contrast, stable air was forecast to move into the northeastern U.S. during the full period, inhibiting the growth of storms there. The NearCasts helped forecasters understand (1) where the low-level thermal/moisture patterns were most favorable, (2) how the differential transport of drier/cooler air aloft could increase the Convective Instability, (3) where stability *tendencies* (both positive and negative) were largest (e.g., near Dallas, Texas, where sustained convection was observed at this time, over northern Pennsylvania, where the lack of warm/moist air at low-levels inhibited convection and additionally over NE Colorado, where low-top supper cells formed as very cold/dry air moved over moderately warm/moist air at lower-levels,) and (4) how all of these Nearcasts related to the dryness patterns traditionally observed in GOES and SEVIRI moisture imagery.

2.6   Boundary Layer Moisture Inferences

A simple method of identifying the existence of low-level boundaries is through channel differences in the ~11 and 12 μm infrared channels. Below (**Error! Reference source not found.**) is an example of a NSSL-WRF simulated 11-12 μm band difference provided by CIRA. Both channels are currently available together on the MSG and other geostationary platforms. The 11 μm channel is a very clean window, and thus is very sensitive to surface temperature. The 12 μm channel radiances, however, are subject to some absorption due to water vapour. As most of the tropospheric water vapour is usually in the lower levels, the band difference is sensitive to low level moisture. As moisture moves into a clear pixel area, the 12 μm brightness temperature will decrease, whereas the 11 μm temperature should stay the same. When this occurs, the 11-12 μm channel difference will become strongly positive and indicates areas of moisture convergence or pooling, which can lead to destabilization and subsequent convective initiation.

It should be noted, however, that the 11-12 μm band difference can also be attributed to other parameters (e.g. moisture in higher levels, surface emissivity effects). The physical retrievals described in section **Error! Reference source not found.** do more properly take such secondary effects into account, i.e. the physical retrieval would provide a more accurate measure of the lower layer moisture.
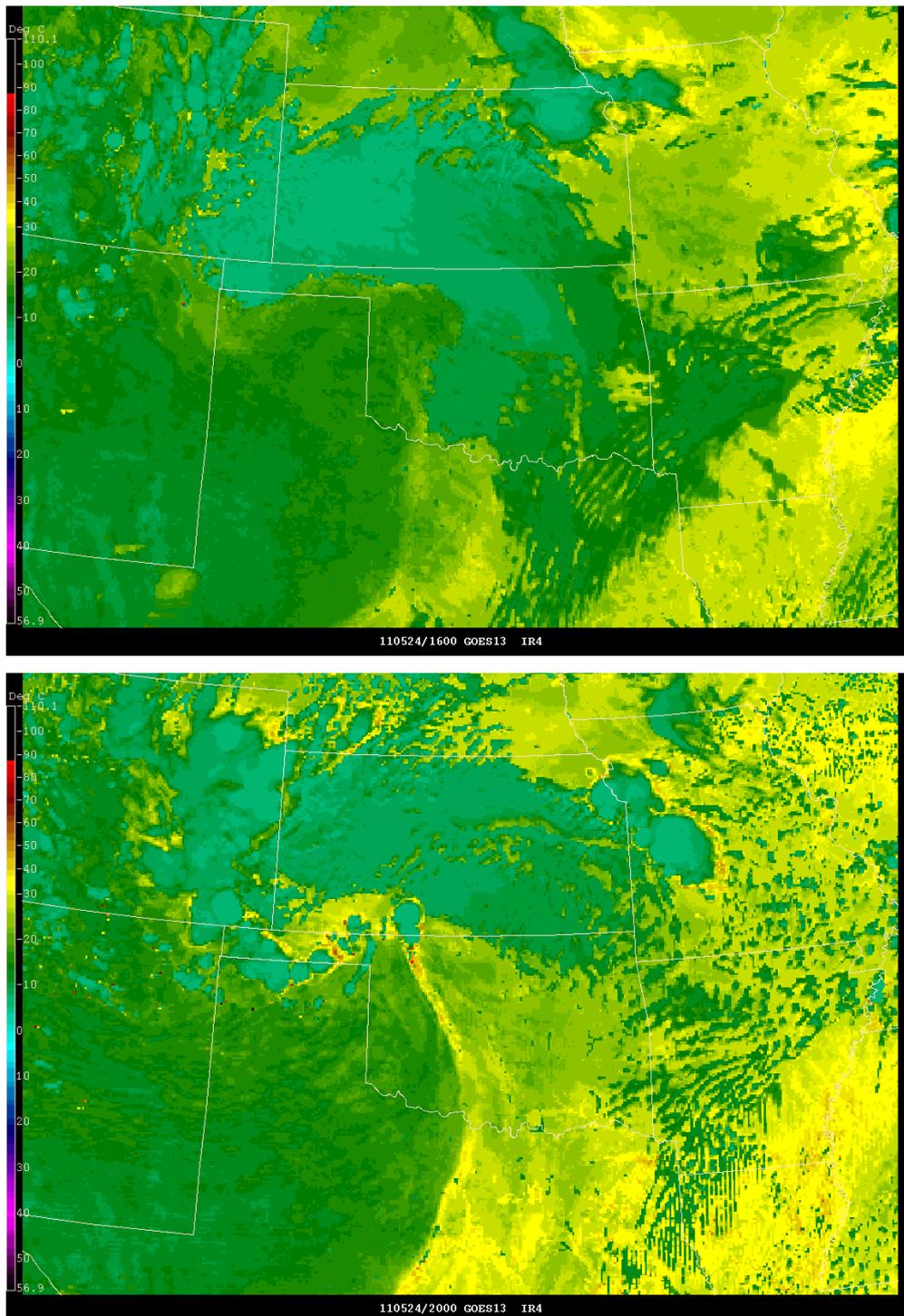
Figure 2.6-1: Simulations of the 11-12 μm band difference for 24 May 2011: At 1600 UTC (top), the channel difference is showing an area of low clouds (blue/green colours) beginning to dissipate over central Oklahoma. At 1900 UTC (not shown) these low clouds are completely dissipated and we can start to see some development of pooling moisture along the dry line in western Oklahoma and the triple point on the Oklahoma/Kansas border. By 2000 UTC (bottom), storms begin to initiate near the triple point and values in the channel difference become strongly positive just south along the dry line.

2.7 High Resolution Atmospheric Motion Vectors: NWC SAF High Resolution Winds product (HRW)

The NWC-SAF HRW product aims at providing detailed sets of Atmospheric Wind Vectors (AMVs, winds calculated through the displacement of tracers in consecutive satellite images), from up to seven MSG-SEVIRI satellite channels: HRVIS, VIS06, VIS08, IR108, IR120, WV062 and WV073 (since HRW v3.2, included in the NWC SAF software package v2012). Both cloudy and water vapour clear air AMVs are calculated for each MSG satellite slot (considering both "nominal scan mode" conditions and "rapid scan mode" conditions), 24 hours a day. HRW product output includes a pressure level definition among additional auxiliary information about how the product was determined (including a Quality index with an indication of its error in probabilistic terms).

The HRW product can be useful in nowcasting and very short range forecasting applications, in synergy with other data available to the forecaster, for the watch and warning of dangerous wind situations, the monitoring of the general flow, of low level convergence (when and where cumulus start to develop), of divergence at the top of developed systems, or other cases of small scale circulation or wind singularities. It can also be used in form of objectively derived fields, and assimilated in regional mesoscale analysis applications or NWP models.

The HRW output (BUFR bulletins) is similar to other AMV products generated by other satellite operators: The HRW winds and related parameters are calculated as individual vectors scattered throughout the processing region. No additional processing, e.g. interpolation to a regular grid or further meteorological analyses, is included.

AMVs can be calculated for up to two different tracer scales: "basic winds" and "detailed winds". The tracer dimension can be defined by the user, with a default value of 24 pixels for the basic dataset. Additional processing parameters can also be configured through the "HRW Model Configuration File", in particular the region to be processed, the MSG satellite for which AMVs are to be calculated, and the tracking and height assignment methods used (with "cross correlation" for tracking and "CCC (cress-correlation coefficient) method" for the height assignment as defaults).

Information on the cloud type and the pressure level related to the AMVs are calculated by default considering the output of Cloud Type and Cloud Top Temperature and Height products (also included in the NWC SAF software package), which have to be calculated before running the HRW product.

The HRW product has been validated in a region covering Europe and the Mediterranean Sea, with a mean Normalized Root Mean Square Vector Difference (NRMSVD) of 0.41 for HRW v3.2 AMVs. This is basically in line with the results of the AMVs produced by other Extraction Centres (like EUMETSAT central processing facilities), although with a much higher resolution of AMV data. The whole validation can be found in the "Validation Report of HRW product" at NWC SAF web page (www.nwcsaf.org).

The whole process of HRW algorithm includes the following steps:

1. Initialization of data: latitude/longitude/solar zenith angle matrices, NWP data, MSG/SEVIRI HRIT data, NWC SAF Cloud Type and Cloud Top Temperature and Height outputs.
2. Tracer calculation with two consecutive methods: Gradient and Tracer characteristics.
3. Tracer tracking with one of two different methods ("Euclidean distance" or "Cross correlation"), with the selection of up to three correlation centres.
4. Height level assignment through one of two different methods ("Brightness temperature interpolation method' or "CCC method").
5. Wind calculation, with the position of the initial tracer location and the final correlation centres.
6. Quality control and choice of the "Best wind" for each tracer with EUMETSAT Quality Indicator method.
7. Orographic flag calculation, which incorporating topographic information detects those winds affected by land influence.

An example of HRW v3.2 AMVs for 14 May 2010 at 1200Z is shown in

Figure 2.7-1; the colour coding is based on the pressure level of the AMVs and the MSG/SEVIRI channel used for the AMV extraction , respectively.
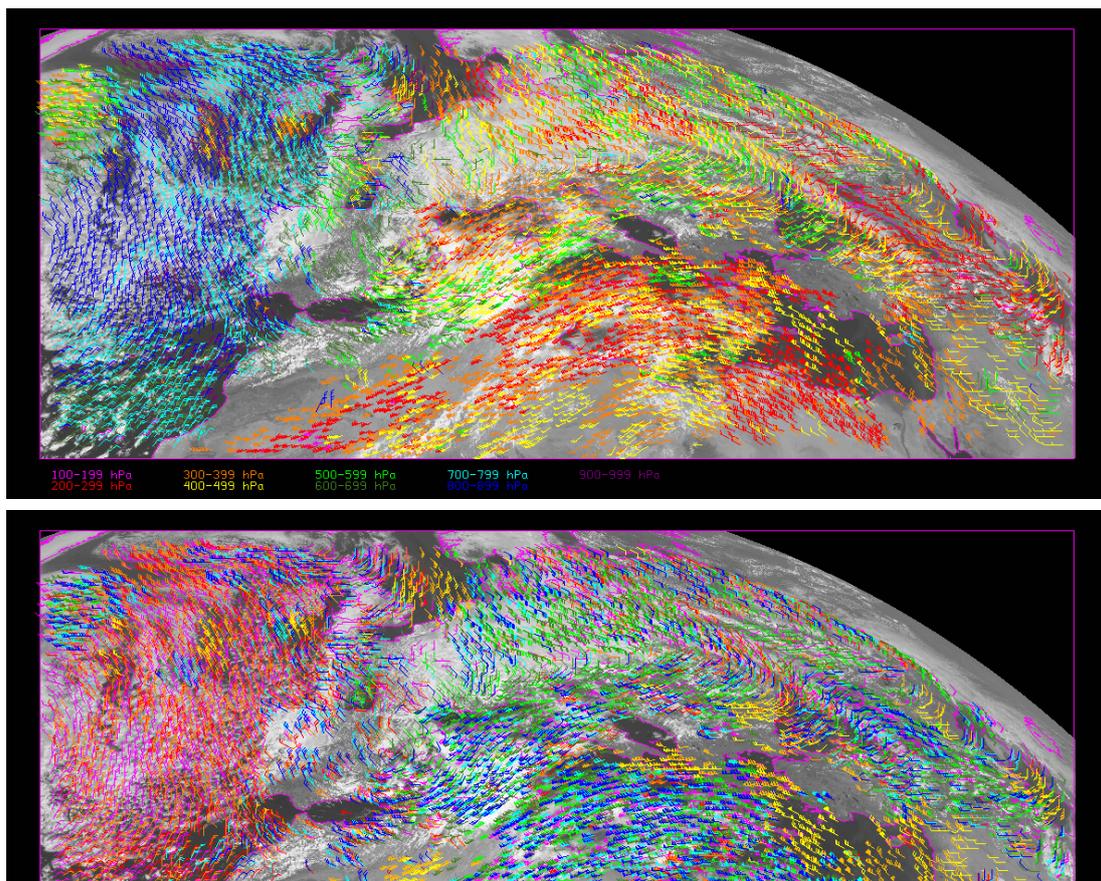
Figure 2.7-1: HRW v3.2 AMVs for 14 May 2010 at 1200Z.

The HRW product is obtained locally shortly after the MSG/SEVIRI image is available for every MSG satellite slot, considering both "nominal scan mode" and "rapid scan mode" (up to twelve times per hour).

The density of AMV data in the HRW output is higher than the one provided by the AMVs coming from other sources (like EUMETSAT central processing facilities), allowing a very detailed definition of the wind flow in both cloudy and clear air areas in the processing region, which can be very useful for a detailed watch of dangerous wind situations, a detailed monitoring of convergences and divergences (especially when related to convective cloud formation), and a detailed monitoring of small scale circulation and other wind phenomena.

Two main assumptions exist in the HRW algorithm considering its default configuration:

- The HRW height assignment depends on the NWC SAF cloud product outputs. Most of the error of HRW AMVs (around 75% of the Normalized Root Mean Square Vector Difference, NRMSVD) has been detected to be related to the height assignment in the default configuration of HRW product, but not only on the value of these cloud product outputs but also the way they are processed to define the pressure level for the AMVs related to each cloud type. Modifications in how the "CCC height assignment method" processes these cloud products in the near future expect to significantly reduce this error.
- The HRW algorithm is setu up such that there is a high dependency on the underlying NWP model. When inconsistencies appear between the observations and the model, both the definition of the "tracking area" in the second image through the wind guess (when it is used), and the quality control against the forecast are affected.

It should be noted that the amount of available AMV data is variable with time as it is related to the evolution with time of the traceable areas (cloudy or humidity patterns) in the processed region. Nevertheless, with the calculation since HRW v3.2 of AMVs from up to seven SEVIRI channels (including clear air areas in the water vapour channels), the problem is somewhat reduced.

Despite all these problems, there will always be areas where no suitable tracers were found and thus no AMVs were detected, which obviously does not automatically imply that there is no wind in these areas!

2.8   Mesoscale Atmospheric Motion Vectors for Moisture Convergence

Water vapour (WV) channels from current operational geostationary satellites provide forecasters with valuable information about the moisture and dynamical properties of the middle and upper troposphere. The remote sensing capabilities from geostationary orbits can complement the synoptic observational data and NWP output and provide positive impact on both qualitative and quantitative analysis of the atmospheric state and helps assessing factors for generation and maintenance of conditions which are favourable for convection. In Georgiev (2003), thermodynamic information about the boundary layer temperature/humidity (derived from 3-hourly synoptic surface observations) is combined with mid- to upper level moisture content (obtained by hourly satellite data in suitable WV channels). Based on this observational information, an index was proposed in addition to the well-known instability indices to serve as a measure of potential instability, marking conditions where warm moist surface air is capped by a deep mid- to upper-tropospheric dry layer. Such an approach can be useful as a tool to monitor pre-convection situations and convective activity, especially when radiosoundings are lacking.

Different authors have stressed the specific large-scale moisture features related to the environment of severe convection, which are seen on satellite WV imagery. Thiao et al. (1993) discussed conceptual models of several types of heavy precipitation situations, as observed in the WV imagery. A key element of their classification is the consideration of the process regarding the evolution of WV plumes, defined as movements of surges of well shaped bands of moisture. WV plumes are associated with the large-scale circulation at mid to upper levels, and take on a plume-like appearance in animated WV images. Thiao et al. (1993) classified the WV plumes, which are associated with extremely heavy rainfall, into four categories depending on the plume and jet stream structures. A conceptual model of non-plume/non-cyclonic circulation event is also considered in which the moisture is present on the WV imagery as a result of residual moisture from a previous system or WV plume, or as a result of moisture advected into the area.

The most extensive use of WV imagery in recent years has been to identify upper-level wind features such as short-wave troughs and to compare their location and intensity to those produced by numerical forecast models. For example, Weldon and Holmes (1991) compiled a catalogue of WV imagery for use in identifying a wide range of upper air features. The identification of these features arises from spatial patterns of brightness in the water vapour images (related to the variation of radiance with moisture content in the upper troposphere). Subjective adjustments to forecasts can be made from observed differences in the location and intensity of troughs, jets, and other features in satellite imagery to those in model analyses and forecasts.

Moisture boundaries visible in the WV (notably the 6.2 μm channel) imagery are often related to upper-level dynamic structures (see e.g. Weldon & Holmes, 1991; Santurette and Georgiev, 2005). *Figure 2.6-1*Figure 2.8-1 shows an example (Georgiev and Santurette, 2009): A jet stream moisture boundary is present (red arrow in (b)), together with a mid-level moisture boundary (blue arrow in (a)), which is related to a a mid-level jet (MLJ). As the wind information in (c) suggest. The vertical cross-section in (d) shows that this MLJ is a signature of the presence of a baroclinic zone (in the low-level field of wet-bulb potential temperature), i.e. of warm advection. The recognition of the mid-level jet signature on the WV imagery in the 7.3 μm channel enables diagnosing mid- to low-level thermodynamic environments which are favourable for intense convection (Santurette and Georgiev, 2007).
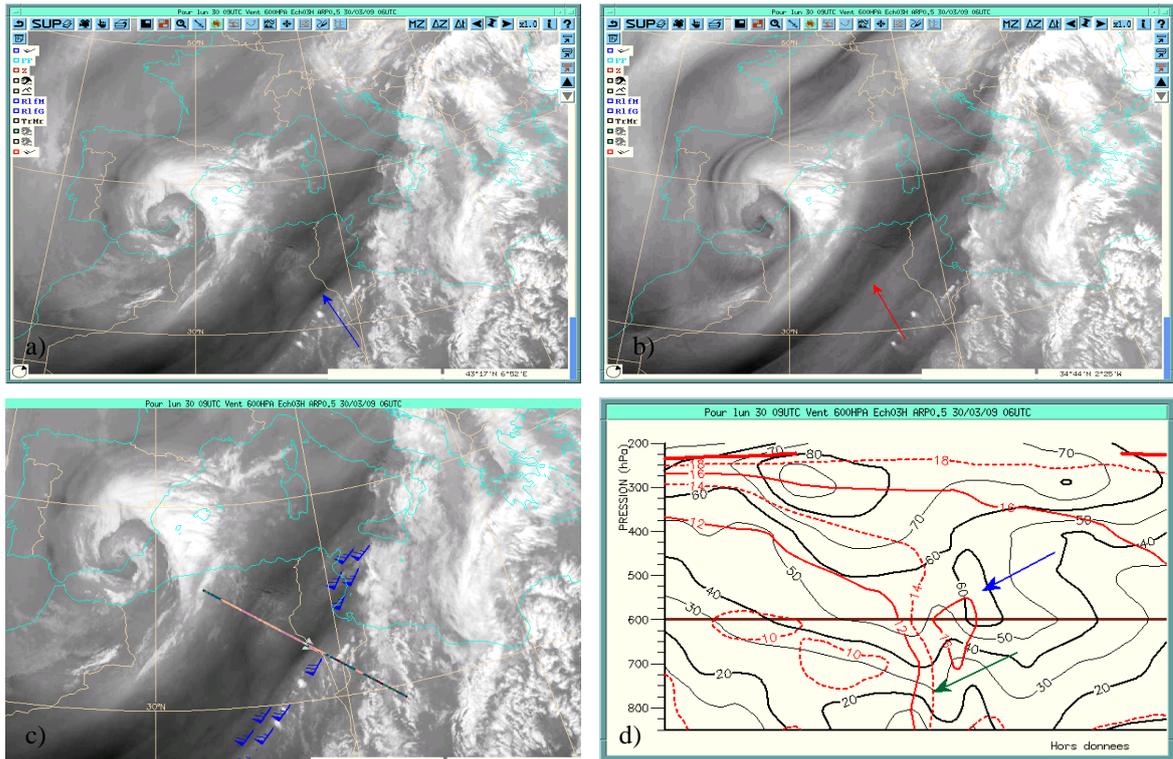
Figure 2.8-1: Jet stream moisture boundaries in a pre-convective environment as seen in MSG WV images on 30 March 2009 at 0900 UTC:
(a) WV 7.3 µm with a mid-level jet-stream moisture boundary (blue arrow),
(b) WV 6.2 µm with an upper-level jet-stream moisture boundary (red arrow)
(c) as (b), but with wind vectors at 600 hPa (blue, only > 60 kt).
(d) vertical cross-section of wind (black, an MLJ at the blue arrow, perpendicular to the line in (c)) and wet-bulb potential temperature (red(showing a low-level baroclinic zone (green arrow)

Figure 2.8-2 illustrates how the upper- and mid-level moisture boundaries on the imagery of the two WV channels of MSG are related to thunderstorm developments over the Mediterranean. Positive factors for convective development are present downstream right of a middle-level moisture boundary, seen in the WV 7.3 µm channel, associated with a low-level baroclinic zone as well as downstream left of an upper-level moisture boundary, seen in the WV 6.2 µm channel, at the left exit of an upper-level jet .
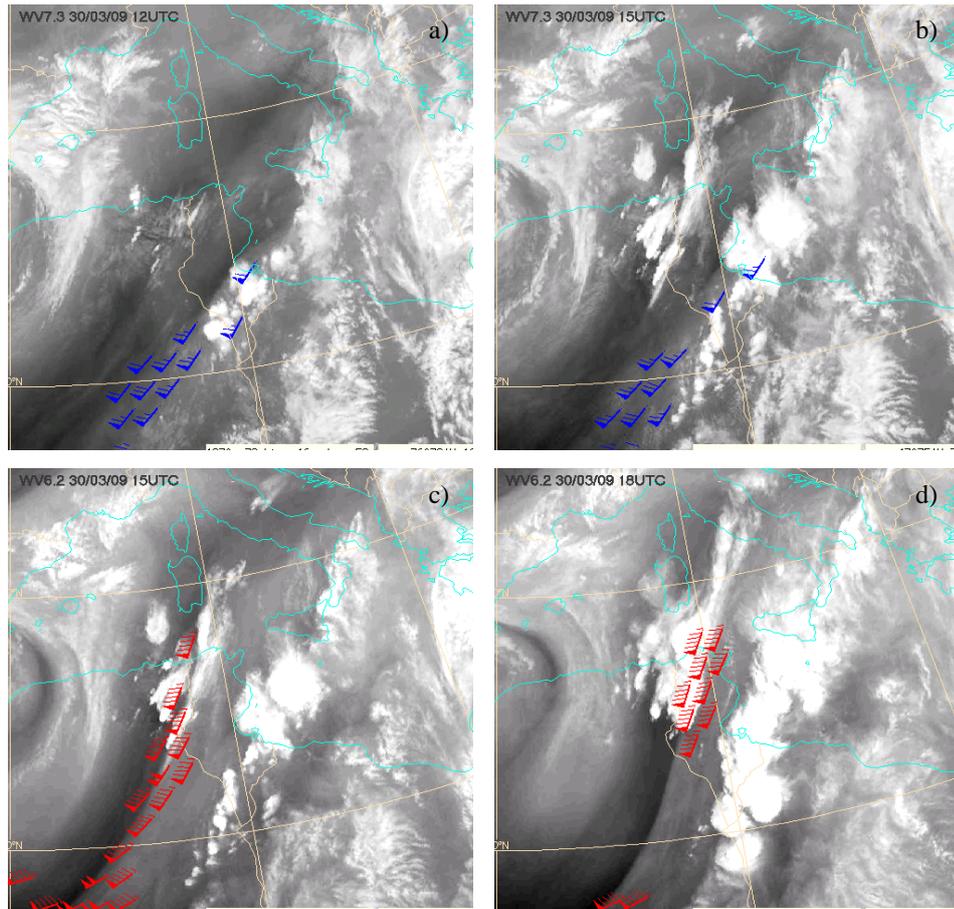
Figure 2.8-2: Convective developments on 30 March 2009 on 4 October 2005: Downstream right of a middle-level moisture boundary, seen in the WV 7.3 μm channel images, overlaid by wind vectors at 600 hPa (blue, only > 60 kt) in (a) at 1200 UTC and (b) 1500 UTC; Downstream left of an upper-level moisture boundary, seen in the WV 6.2 μm channel images, overlaid by wind vectors at 300 hPa (red, only > 90 kt) in (c) at 1500 UTC and (b) 1800 UTC.

In addition to the subjective use of water vapour imagery in forecasting, the imagery has been used quantitatively to provide estimates of the wind through movement of clouds and moisture features between successive images, where direct measures from weather balloons are lacking. Such atmospheric motion vectors are routinely derived by all operational meteorological satellite operators, mainly in support to numerical weather prediction.

Rabin et al. (2004) demonstrate how a satellite-derived wind algorithm can be used to detect mesoscale flow patterns. The winds are used to track upper air features such as jet maxima, and divergent regions where vertical air motion and convective development

might be enhanced. The automated technique relies on a forecast wind field to facilitate the location of common features between successive images. The forecast winds used are from the U.S. Navy Operational Global Atmospheric Prediction System (NOGAPS) model (Rosmond, 1992). By employing a model with relatively low spatial resolution such as the NOGAPS, the addition of higher resolution winds from the satellite is more clearly identifiable. Current implementation utilizes time interpolation to provide hourly updates of the background wind field between forecast output times. Since the mean height of wind vectors varies over a given region, it is necessary to interpolate the values to a constant altitude before evaluation of horizontal gradients required in the computation of kinematic parameters such as vorticity and divergence (Figure 2.8-3).

Displays of the mesoscale wind properties are available on the web for real time data and for archived cases. (http://cimss.ssec.wisc.edu/mesoscale_winds/). An example is given in Figure 2.8-3.
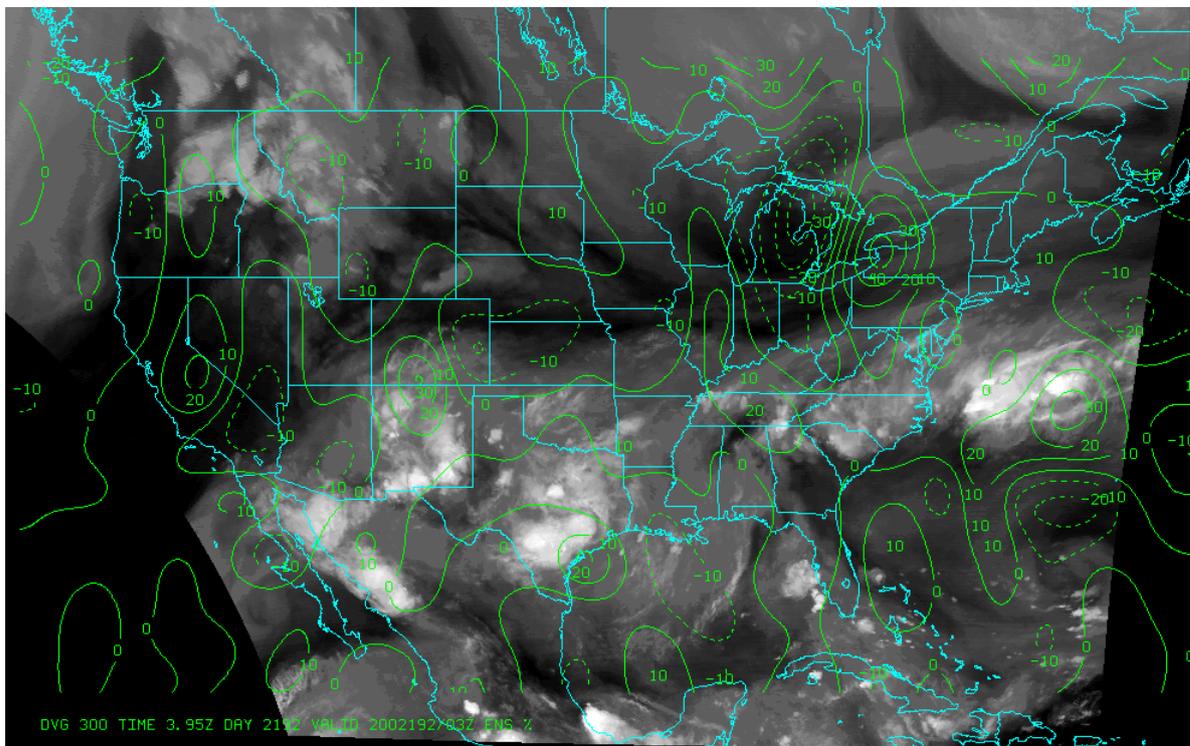
Figure 2.8-3: GOES-12 water vapour imagery and the derived divergence field (green, 10^{-5} s^{-1})for 12 July 20120, 0545 UTC.

A similar product exists for MSG, where the upper level divergence is computed form the derived WV atmospheric motion vectors (Schmetz et al., 2005).

Figure 2.8-4Figure 2.8-5: Classification of the eight different convection regimes observed in Figure 2.8-4 and their relation ot the satellite observed upper level divergence

shows an example of how this MSG divergence product is (visually) combined with the IR cloud top temperatures in such a way that divergent/convergent upper-level flow can be identified together with the onset of deep moist convection. Here, the convective cells are classified in 8 cases (Figure 2.8-5) according to the observed divergence at the location of their initiation and development (. An evaluation of many of such cases shows that 76% of all convective cells initiated at areas upper level divergence, 92% of all convective cells

further developed at areas of divergence, and in 15% of the cases, the upper level divergence is actually a result of the strong convection.
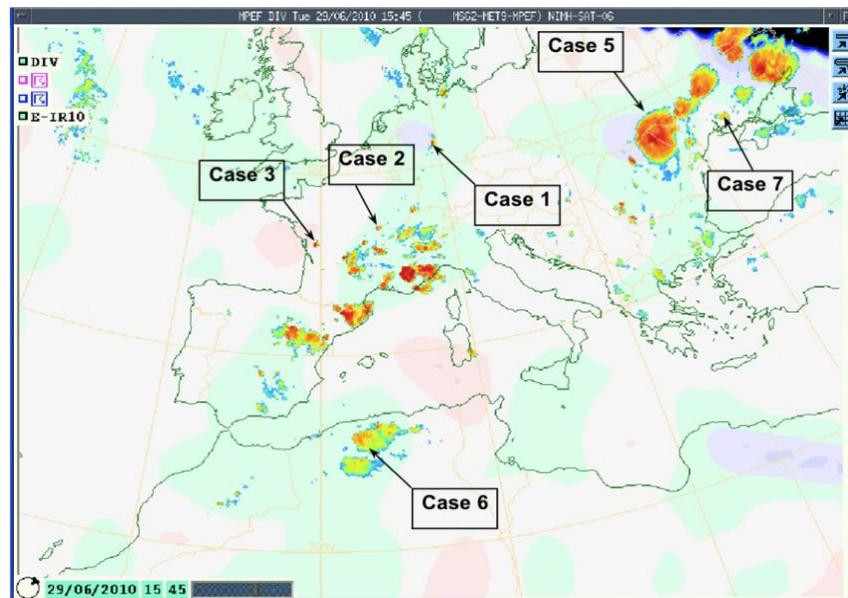

Figure 2.8-4: A study of the relation between the divergence field and deep moist convection. The convective cells are classified in 8 cases according to the location of their initiation and development regarding the divergence or convergence in the area as described by the satellite divergence product.
Colour legend of background shading: green to blue increasing divergence, lilac to red increasing convergence
Colour legend of cloud top temperatures: yellow: < -50 C, red: < -60 C

CASE 1	Convective cells initiating at an area of strong	Divergence	> +20 $10^{-6}s^{-1}$
CASE 2	at	weak Divergence	[+20 ÷ 0 $10^{-6}s^{-1}$]
CASE 3	at	weak Convergence	[0 ÷ -20 $10^{-6}s^{-1}$]
CASE 4	at	strong Convergence	[< -20 $10^{-6}s^{-1}$]
CASE 5	Convective cells developing at	strong Divergence	> +20 $10^{-6}s^{-1}$
CASE 6	at	weak Divergence	[+20 ÷ 0 $10^{-6}s^{-1}$]
CASE 7	at	weak Convergence	[0 ÷ -20 $10^{-6}s^{-1}$]
CASE 8	at	strong Convergence	[< -20 $10^{-6}s^{-1}$]

Figure 2.8-5: Classification of the eight different convection regimes observed in Figure 2.8-4 and their relation ot the satellite observed upper level divergence

It is recommended to diagnose the upper level divergence together with atmospheric instability information to anticipate where the convective updraft can be accelerated, Figure 2.8-6 provides an illustration: In this case, the atmospheric instability (represented by high CAPE value) is initially equally high over an area in Austria and in Ukraine, as seen in the 1445 UTC analysis. Over Ukraine, however, the upper level wind field suggest a

convergent flow, thus suppressing convection, while the upper level flow was diveregent over Austria. The IR image taken 4 hours later at 1845 UTC then well shows the convection over Austria, while now storms developed over Ukraine.
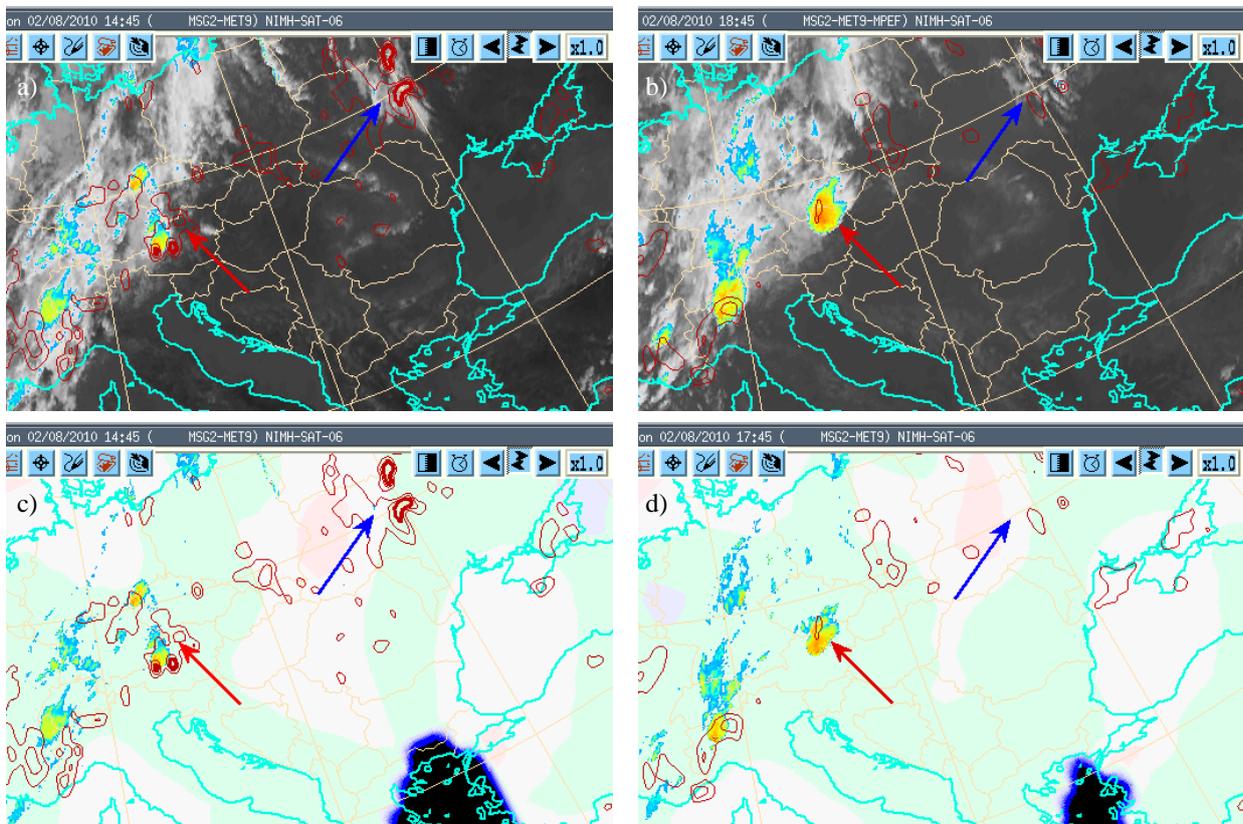
Figure 2.8-6: Combined use of atmospheric instability and upper-level divergence information.
Upper left: MSG IR image of 02 August 2012, 1445 UTC, with model CAPE fields superimposed (red contours, starting at 800 J/kg)
Upper right: MSG IR image of 1845 UTC on the same day shows the developed convection over Austria (red) and the suppression of convection over Ukraine (blue)
Lower left: MSG derived upper level divergence for 1445 UTC (green shows a divergent flow, red convergence)
Lower right: as lower left, but for 1745 UTC, showing the sustained convergent flow over Ukraine

The upper level divergence is also related to upper tropospheric potential vorticity (PV) anomalies, as shown in Figure 2.8-7. A strongly divergent flow may significantly contribute to formation of an intense convective development, when other upper level dynamical features are present (e.g. tropopause folding, jet stream).
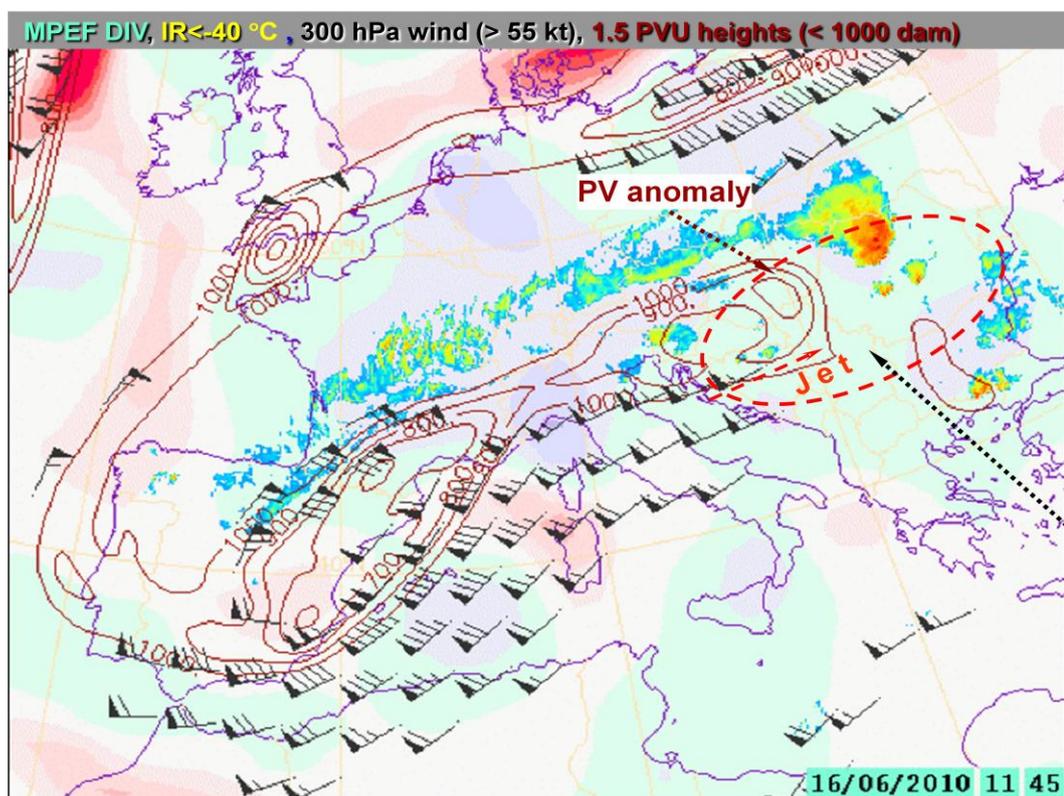
Figure 2.8-7: DIV product as forecast tool. In this example, a convective cell initiated at the left exit of a jet and divergence seen by MPEF DIV product: in the range $[+20.10^{-6} \text{ s}^{-1}]$. Data are shown at 1145 UTC on 16 June 2010.

The satellite WV imagery allows interpreting water vapour patterns in terms of dynamical processes in the atmosphere and their relation to diagnostics available from NWP models. In particular, the interpretation can be based on the close relationship between the WV (e.g. 6.2 μm) channel imagery and potential vorticity fields in the upper troposphere. Over Western Europe and the Mediterranean , the development of strong convective systems is usually associated with clear upper level synoptic forcing via advection of potential vorticity (PV) anomaly, in addition to a conditional instability of the atmosphere (Santurette and Georgiev, 2005). Using WV images superimposed onto NWP fields of PV and other dynamical parameters is a relevant tool for synoptic analysis in this context as depicted in Figure 2.8-8, showing MSG WV (6.2 μm) images on 30 June 2006 overlaid by

the 300 hPa wind field (only > 40 kt) and heights of the dynamical tropopause, which is represented by constant surface of PV = 1.5 PV-units (brown, only < 1000 dam).
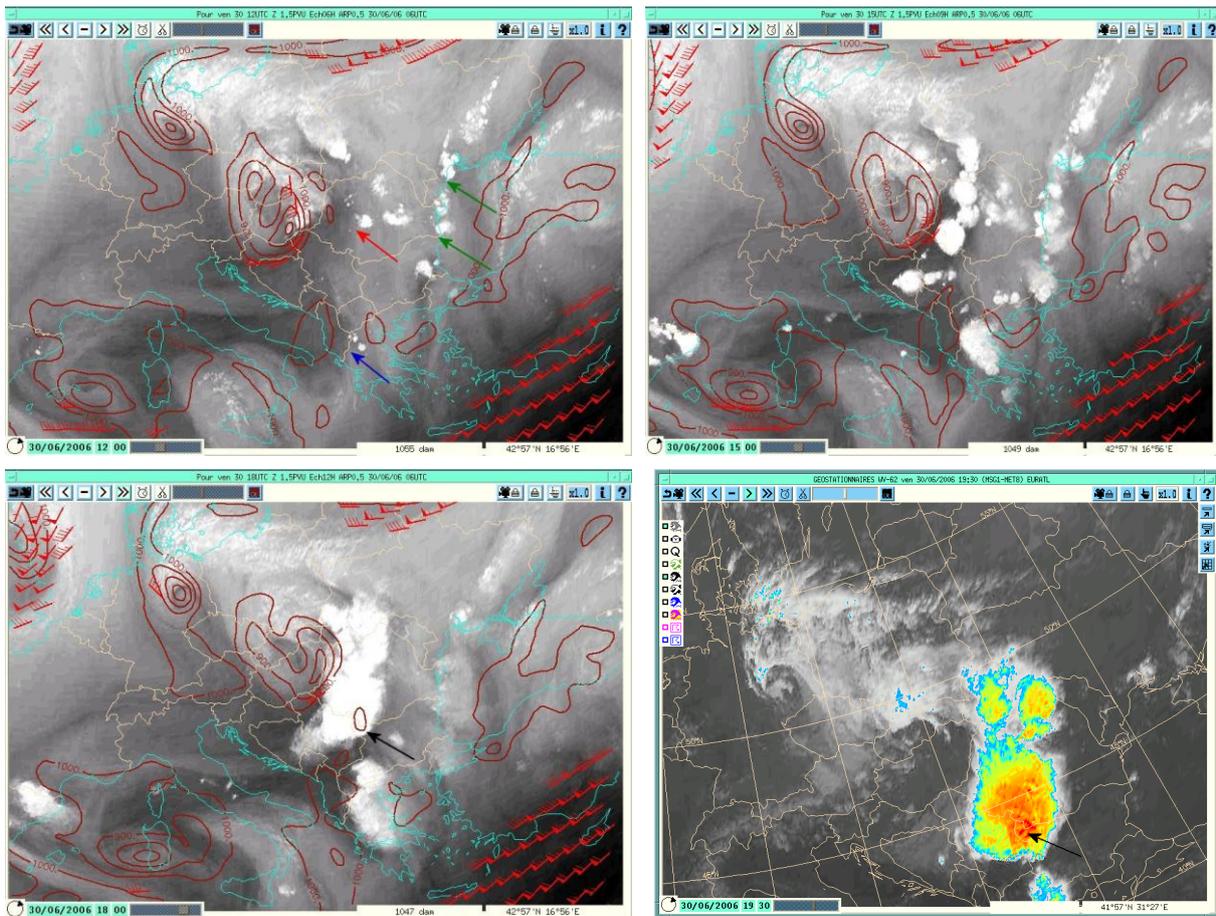
Figure 2.8-8: MSG WV images, PV and 300 hPa winds (PV and winds from the 12 UTC ARPEGE model run) for 30 June 2006
Upper left: 1200 UTC
Upper right: 1500 UTC
Lower left: 1800 UTC
The lower right image is the MSG IR image with colour coded cloud top temperatures, taken at 1930n UTC
(winds > 40 kt, PV < 1000 dam are plotted; for further explanation see text)

The WV images enablethe observation of conservative potential vorticity patterns, seen as WV image dark dry zones, which tend to be advected in areas of pre-convective low-level environment (Santurette and Georgiev, 2007). The leading boundary of such a dry zone is present at the position of the red arrow in Figure 2.8-8 (upper left panel). Lifting is induced

near travelling positive potential vorticity anomaly associated with a dynamic dry band seen in the WV images. As indicated in Browning et al. (2007), such PV anomalies are especially important because as well as inducing lifting, they also increase the convective available potential energy due to the pool of cold air at middle and upper levels.

The case shown in Figure 2.8-8 also illustrates the concept of Krennert and Zwatz-Meise (2003) identifying the transition zone of dark (dry) and light (moist) regions on Meteosat WV images as favoured areas for the initiation of deep moist convection over Europe. The validity of this concept was confirmed by Ghosh et al. (2008), regarding the initiation of convective cells of "Nor'westers", severe thunderstorms during pre-monsoon season (March, April, and May) in northeastern part of Indian subcontinent, showing that, in general, convective cells of Nor'wester have a strong tendency to be initiated along/near the edges of mid-upper atmospheric dryness, seen as dark WV imagery features, as the edges overrun a low-level moist air.

In addition to the WV image interpretation performed by Krennert & Zwatz-Meise (2003) and Ghosh et al. (2008), for prediction of convective development, the upper-level dry boundaries seen in the imagery should be considered with respect to the stage of their dynamic development (Georgiev and Kozinarova , 2009). According to their interpretation, three kinds of moisture boundaries, at which convective cells initiate, are identified in Figure 2.8-8 (upper left panel), are related to corresponding dry WV imagery patterns, according to the classification of Santurette and Georgiev (2005), as follows:

- A latent dry band/spot, at the position of the blue arrow: These features of medium gray (rarely dark gray) shades are associated with weak descending motions (or their absence) and a latent tropopause anomaly (a weak PV anomaly) but lack a jet. They may move in accordance with the upper-level wind field but they are not associated with further significant disturbance development, as long as they do not interact with a jet.
- Deformation dry band, at the position of the green arrows: These patterns may be associated with subsidence, but they are not connected with jets and PV anomalies. They are associated with deformation zones of the upper level flow. In a specific situation, the dry air aloft, associated with such dark features, may be conducive for convective development by generating instability.
- Dynamic dry band at the position of the red arrow: This is associated with strong subsidence, jet streams, and PV anomalies. Such a dynamically significant dry band is associated with significant subsidence and a tropopause dynamic anomaly.

As shown in the sequence of images in Figure 2.8-8a, Figure 2.8-8b and Figure 2.8-8c strong convection develops are especially associated with the moisture boundary at the leading edge of a dynamic dry zone, which is identified at the position of the red arrow in on Figure 2.8-8a. This WV image dynamic dry feature is related to an upper-level PV anomaly (low heights of the dynamical tropopause, Santurette and Georgiev, 2005), which tends to be advected in an area of a favourable pre-convective low-level environment. This case produced severe weather convective events over the north-western part of Bulgaria (at the black arrow in Figure 2.8-8c and Figure 2.8-8d).

3 CONVECTIVE INITIATION NOWCASTING: WHICH CLOUDS WILL BECOME THUNDERSTORMS IN THE NEAR FUTURE?

For the purposes of 0–1 hour convective initiation (CI) nowcasting studies, the definition of CI has exclusively been the radar precipitation echo intensity criteria of ≥30–40 dBZ (Browning and Atlas 1965; Marshall and Radhakant 1978; Schreiber 1986; Wilson and Schreiber 1986; Wilson et al. 1992; Wilson and Mueller 1993; Roberts and Rutledge 2003; Mecikalski and Bedka 2006; Mecikalski et al. 2010a,b). Radar echo intensities between –5 and ~10 dBZ, are associated with and used to identify convergence zones (Schreiber 1986; Weckwerth and Wakimoto 1992), whereas echo intensities >10–20 dBZ are likely the result of backscatter from small hydrometeors (Knight and Miller 1993), making intensities <30 dBZ not useful for validating thunderstorm nowcasting studies. The ≥30 dBZ criteria has subsequently been adopted and used in other CI–related research studies towards the formulation of operational algorithms (Walker et al. 2011a).

3.1 Convective Cloud Identification

The Berendes et al. (2008) convective cloud-typing algorithm is one of several cloud typing approaches, yet is specifically designed to identify only cumulus clouds in various stages of development. It is a statistical clustering approach toward the classification of cloud types within meteorological satellite imagery, specifically visible and infrared data. The method is based on the Standard Deviation Limited Adaptive Clustering (SDLAC) procedure, which has been used to classify a variety of features within both polar orbiting and geostationary imagery, including land-cover types, volcanic ash, dust and clouds of various types. The focus is then on classifying cumulus clouds of various types (e.g., "fair weather," towering, and newly glaciated cumulus, in addition to cumulonimbus).

The SDLAC algorithm has been demonstrated using GOES-12, MSG SEVIRI, and MODIS imagery. Results indicate that the method performs well, classifying cumulus similarly between MODIS, SEVIRI and GOES, despite the obvious channel and resolution differences between these three sensors. The SDLAC methodology has been employed in several research activities related to convective weather forecasting (e.g., SATCAST, see description below), which offers some proof of concept for its value.

The SDLAC clustering algorithm for GOES-12, MODIS and SEVIRI sensors is applied to produce a convective cloud mask for each data type. The clustering algorithm was applied to a set of images from each sensor and the resulting clusters were labelled as belonging to seven different classes. *Figure 3.1-1* shows a list of the classes along with associated colours that will be used in subsequent figures. The classes were defined based upon visually identifiable features in the image. Note that the main goal was to identify convective clouds ("towering cumulus" and "cumulus") in various stages for use in convective nowcasting systems. Toward that end, minimal effort was made to distinguish cloud types beyond convective types and they have been grouped into general categories such as "ice cloud" and "Non-convective water cloud". Two additional classes, "glaciated mature convection" and "overshooting convective tops," are also being examined for possible application in turbulence studies.
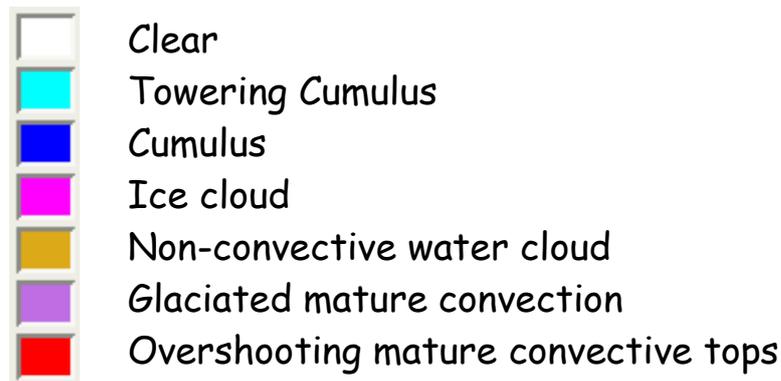
Figure 3.1-1: Classes defined by the SDLAC convective cloud mask.
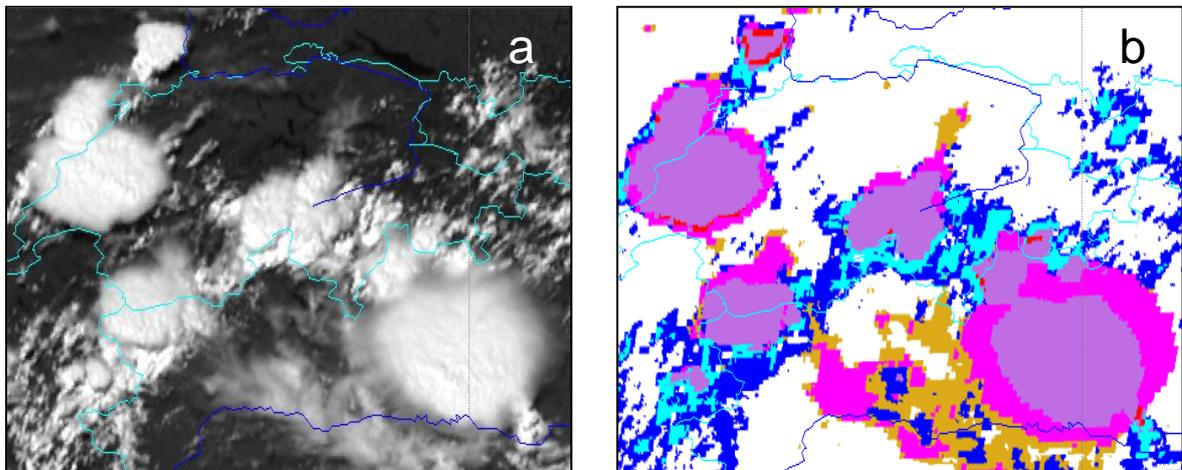
Figure 3.1-2: a) MSG SEVERI image (channel VIS 0.6) centred over northern Italy taken at 1310 UTC 25 June 2006 and b) SDLAC convective cloud mask, refer to Figure 3.1-1 for colour code labels.

An MSG SEVIRI example over northern Italy is shown in Figure 3.1-2 with channel VIS 0.6 shown in (a) and the SDLAC results in (b). Visual examination shows that similarly to the GOES case, the MSG SDLAC mask detects convective clouds well. Additionally, the MSG example contains an area labelled "glaciated mature convection" which represents visually diffuse ice clouds at very low temperatures above a large convective cloud. Some of the "bumpy" texture of the cumulus cloud can be seen through the ice cloud due to gravity waves from the convective updraft penetrating the tropopause. The additional channels in the MSG SEVIRI sensor may be providing more information about cloud phase to help make a better distinction than the GOES version.

The tropopause penetrations within deep convection, i.e. "overshooting mature convective tops" are also detectable in GOES and MSG data using the SDLAC method. A version of the SDLAC clustering mask was produced specifically for the purpose of detecting overshooting tops in GOES imagery. Figure 3.1-3 shows an example of GOES imagery with active convection over Illinois. Figure 3.1-3 (a) shows a three band colour composite of the active system while Figure 3.1-3 (b) shows the same area in the visible channel. Areas of overshooting tops are very cold and have a rougher textured appearance due to the convection protruding above the cirrus anvil. Figure 3.1-3 (c) shows a three band colour composite with channel 1(VIS) in green, channel 2 (IR3.8) inverted in blue, and the texture

information of channel 1 in red. Using this colour scheme, the areas of high texture are clearly visible as red and yellow areas. The highly textured areas correspond to the overshooting tops and smaller convective clouds. Figure 3.1-3 (d) shows the overshooting tops detected by the SDLAC algorithm in red. Clearly, the overshooting tops correspond well with the areas of high channel 1 texture, but the smaller convective clouds are eliminated, probably based upon temperature. Accurate detection of overshooting tops allows for identification of strong convection, and can be used as a tool for identification for the potential for aircraft turbulence. This has a strong application for aviation safety (see Mecikalski et al., 2007).
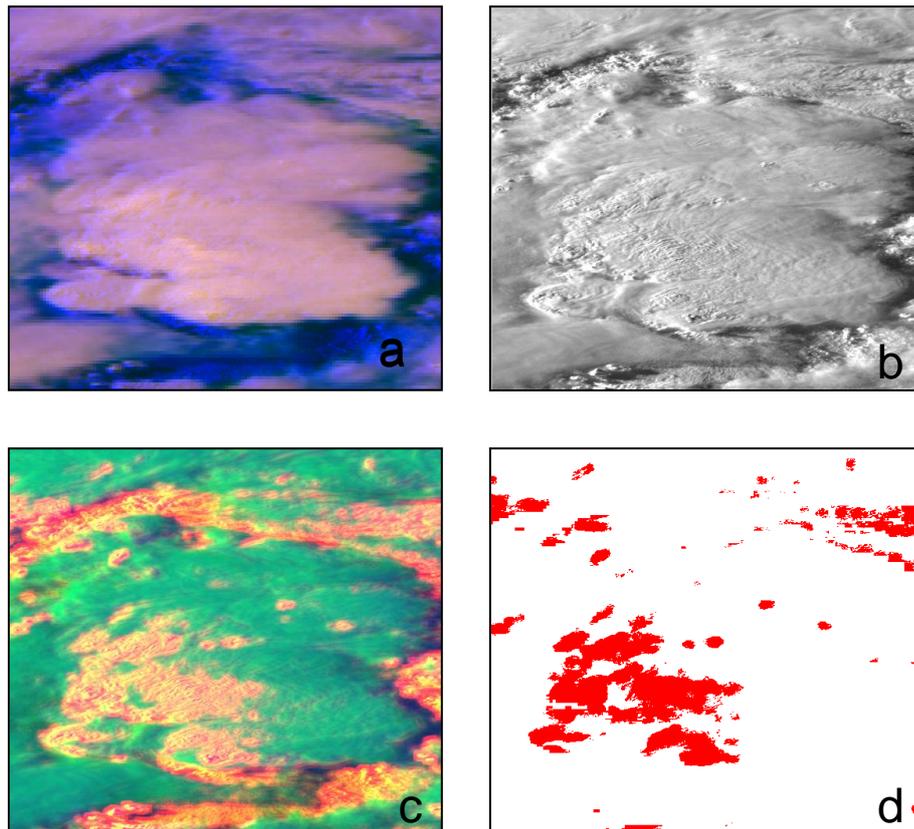
Figure 3.1-3: Example of an "overshooting top" mask for active convection. Data are from GOES-12, with (a) being a three band enhanced colour composite with channel 4 inverted in red, channel 3 in green and channel 1 in blue, (b) an enhanced channel 1 visible image, (c) a three band enhanced colour composite with texture information derived from channel 1 in red, channel 1 in green and channel 2 inverted in blue, and (d) the "overshooting top" mask with red indicating tops. Data are from 2315 UTC May 10, 2003 over Illinois.

3.2   GOES CI Interest Fields

Mecikalski and Bedka (2006; hereafter "MB06") identified the precursor signals of CI with sequences of 1 km resolution visible (VIS) and 4-8 km infrared (IR) imagery from the GOES instrument, following the conceptual framework as shown in Figure 3.2-1. Results indicate that CI may be forecasted 30-60 min in advance through the monitoring of key IR fields for convective clouds. This is made possible by the coincident use of three components of GOES data: 1) a "cumulus cloud mask" (CCM) at 1 km resolution using VIS and IR data (Berendes et al., 2008), 2) satellite-derived mesoscale atmospheric motion

vectors (MAMVs) for tracking individual cumulus clouds (Bedka and Mecikalski, 2005; Bedka et al., 2009), and 3) IR brightness temperature (T_B) and multi-spectral band differencing time trends. In effect, these techniques isolate only the convective cumulus clouds in satellite imagery, track their motion, and evaluate various IR cloud properties as they vary with time. CI is predicted by accumulating information for a satellite pixel that is attributed to the first occurrence of a ≥35 dBZ radar echo. Through the incorporation of satellite tracking of moving cumulus clouds, this work represents a significant advance in the use of routinely available GOES data for monitoring aspects of cumulus clouds important for CI. The CCM delineates cumulus clouds in various stages of development (e.g., small "fair weather" cumulus, cumulus congestus, cumulus with small anvils, cumulonimbus), and provided statistics of the cloud field (e.g., size distributions on regional scales; Berendes et al., 2008).
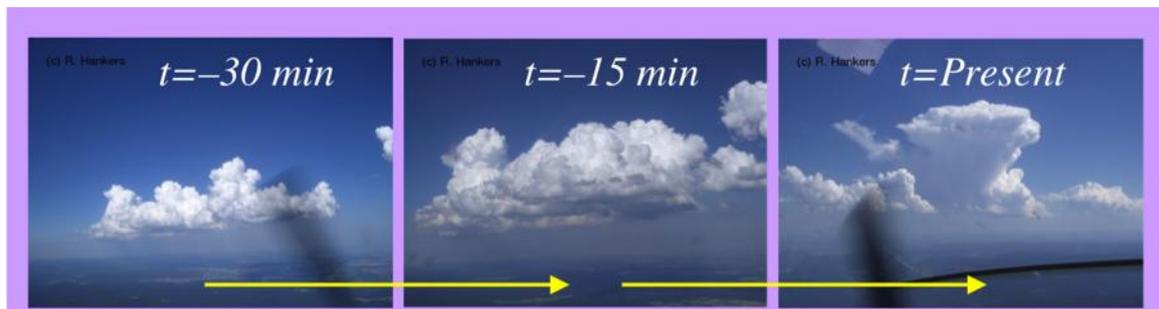
Figure 3.2-1: Conceptual framework for CI nowcasting using satellite data, whereby cumulus clouds are identified and monitored as they grow in time, while their cloud-top properties are evaluated.

Once cumulus cloud tracking is established, 10 predictor fields (Table 3.2-1) based on Lagrangian trends in IR data are used to characterize cloud conditions consistent with CI. Cumulus cloud-pixels for which ≥5 of the 8 CI indicators are satisfied, are labelled as having high CI potential, assuming an extrapolation of past trends into the future. The eight CI IR "interest fields" are the cloud-top T_B (10.7 µm T_B), cloud-top temperature cooling rates at 15 and 30 min time intervals (10.7 µm T_B trend; Roberts and Rutledge, 2003), timing of T_B drop below 0º C, the 6.5–10.7 µm channel difference (Ackerman, 1996), the 13.3–10.7 µm channel difference, time rate of change of the 6.5–10.7 µm channel difference, and the time rate of change of channel difference 13.3–10.7 µm.

CI Interest Field	Purpose and Resolution	Critical Value
6.5 – 10.7 μm difference (IF1)	4 km cloud-top height relative to upper-tropospheric WV weighting function (Schmetz et al. 1997)	$-35°$ C to $-10°$ C
13.3 – 10.7 μm difference (IF2)	8 km cloud-top height assessment (Mecikalski and Bedka 2006; Mecikalski et al. 2008)	$-25°$ C to $-5°$ C
10.7 μm T_B (IF3)	4 km cloud-top glaciation (Roberts and Rutledge 2003)	$-20°$ C $< T_B < 0°$ C
10.7 μm T_B Drop Below 0° C (IF4)	4 km cloud-top glaciation (Roberts and Rutledge 2003)	Within prior 30 mins
10.7 μm T_B Time Trend (IF5, IF6)	4 km cloud-top growth rate/updraft strength (Roberts and Rutledge 2003)	$< -4°$ C/15 mins $\Delta T_B/30$ mins $< \Delta T_B/15$ mins
6.5 – 10.7 μm Time Trend (IF7)	4 km multi-spectral cloud growth (Mecikalski and Bedka 2006)	$> 3°$ C/15 mins
13.3 – 10.7 μm Time Trend (IF8)	8 km multi-spectral cloud growth (Mecikalski and Bedka 2006; Mecikalski et al. 2008)	$> 3°$ C/15 mins
3.9 μm Fractional Reflectance (IF9)	4 km cloud-top glaciation Lindsey et al. (2006)	$\leq 5\%$
3.9 – 10.7 μm trend (IF10)	4 km cloud-top glaciation Siewert (2008)	$t - (t_{-1}) \leq -5$ K and $t - (t_{+1}) \leq -5$ K
30-min trend in 3.9 μm fraction reflectance (IF11)	4 km cloud-top glaciation Siewert (2008)	Continually decreasing below 10%

Table 3.2-1: GOES interest fields used to nowcast CI, and how they relate to physical processes associated with cumulus cloud development.

The MB06 methodology has recently evolved to treat convective clouds as objects, relying heavily on MAMVs to advect clouds over 15-min periods. Clouds are grouped into "cumulus objects" and overlap is required within 5-15 min GOES imagery. Currently, 0-1 hour CI nowcasts are available using GOES-13 imagery over the eastern U.S. every 15 minutes during day and night time hours (Figure 3.2-2). For the newer object tracking approach, in an algorithm called SATellite Convection AnalySis and Tracking system (SATCAST; Mecikalski et al., 2010a), three images are used to monitor for CI, and for GOES, six interest fields are used (all but IF4 and IF6 as in Table 3.2-1), and operates day and night with rapid scan data as available on GOES.
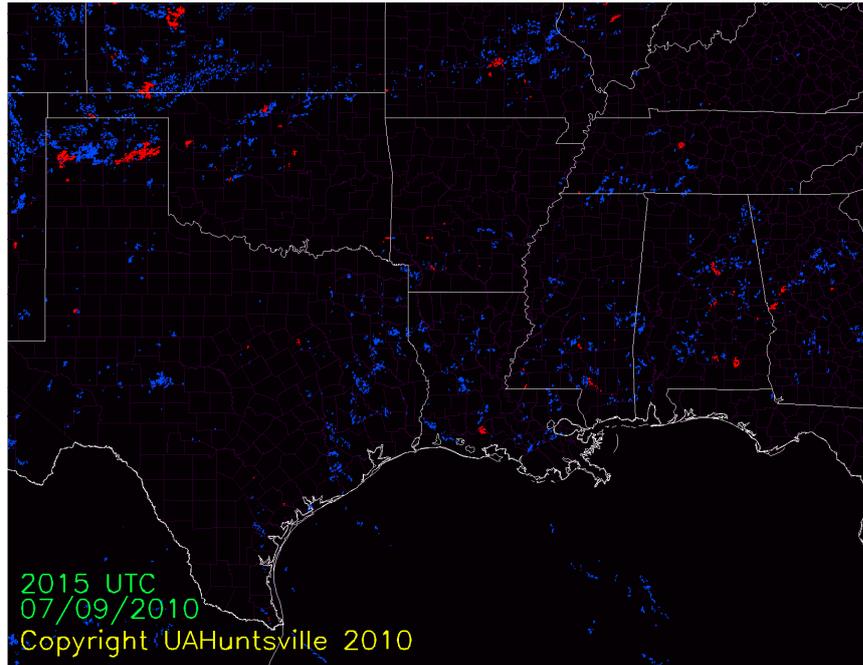
Figure 3.2-2: Object tracking version of the MB06 algorithm. Here, blue and red objects identify clusters of growing convective clouds. Blue objects fail to pass 5 of 6 IR thresholds that identify the presence of strong, persistent updrafts that are glaciating. Red objects pass ≥5 IR threshold tests, and are more likely (>70% chance) to develop into new convective storms (with echo intensities of ≥35 dBZ) within the coming 30-60 minutes. For this effort, CI-objects will be used to isolate locations (on a given day, or afternoon), where CI is becoming more likely over 0-6 hour timeframes. Also, coupled to the land surface variability, we can use these to guide field experiment activities, as well as help address the stated hypotheses.

The University of Wisconsin Convective Initiation (UWCI) nowcast utilizes a box-averaged approach for monitoring cloud top cooling rates (Sieglaff et al., 2010), and leverages the methodology of Roberts and Rutledge (2003) in its reliance of 10.7 μm cloud-top cooling rates to infer future thunderstorm development. The term "box-average" refers to the computation and time differencing of the mean IR-window BT and cloud type properties within a small box centred on the pixel of interest. The box-average approach is best suited for geostationary imagery due to the frequent refresh rate where cloud motion between consecutive scans is small. The difference of the box-averaged IR-window BT field between the current and previous scans is used to reveal areas of cloud top cooling correlated with vertical cloud growth. The UWCI algorithm separates false cloud top cooling associated with horizontal cloud advection from true cloud top cooling associated with vertical cloud growth through a series of tests. After the true cloud top-cooling signal is isolated, the cooling pixels are assigned convective initiation nowcast categories based upon cloud top type classification and trends. Three categories exist, Pre-CI Cloud Growth, CI Likely, and CI Occurring, which represent vertically growing water cloud, vertically growing supercooled/mixed phase cloud, and vertically growing, recently glaciated cloud, respectively.

The UWCI is considered relatively computationally inexpensive, uses a physically based IR-only cloud type algorithm allowing day/night independence, and like SATCAST is portable from one geostationary imager platform to another. The box-average methodology does not require the calculation of computationally expensive AMVs (Bedka et al., 2009), such as those needed in the Mecikalski and Bedka (2006) SATCAST methodology, thereby

reducing false alarms caused by cloud-tracking errors. UWCI uses only cloud top cooling rates from the 10.7 μm channel, and therefore is limited in how is can exploit current and future geostationary imagers which offer many IR channels. The box-averaged method is not perfect and complex logic is required to eliminate false 10.7 μm cooling induced by horizontal cloud advection, thin cirrus motion, and complex multilayer cloud scenes.

The UWCI algorithm has been validated against cloud-to-ground lightning initiation (different that the first-flash LI as defined in Harris et al., 2010, below) derived from the National Lightning Detection Network cloud-to-ground strikes, which serves as a proxy for convective initiation. The validation consists of manually tracking clouds through space and time using GOES-12 IR-window imagery to determine: 1) the LI probability of detection (POD), which is defined as the number of LI events within the validation period that were correctly nowcast by the UWCI algorithm and 2) the UWCI nowcast false alarm ratio (FAR), which is defined as the number of UWCI nowcasts that were not associated with an LI event.
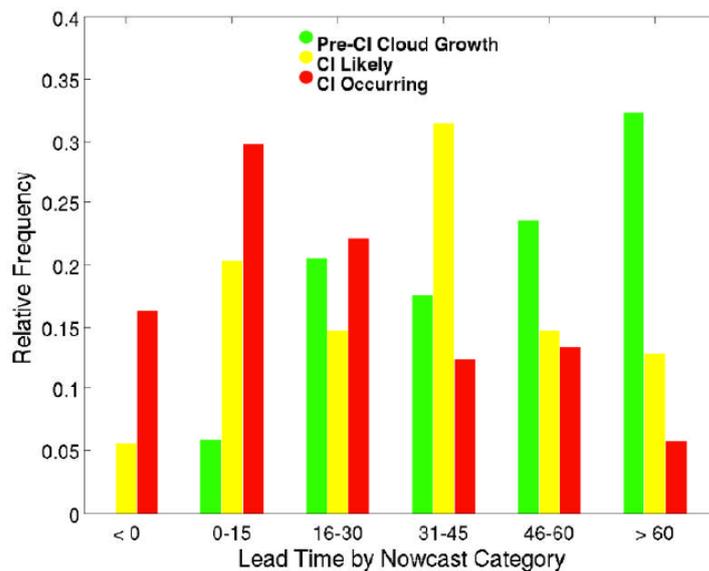
Figure 3.2-3: Relative frequency of lead-time by UWCI nowcast category for all successfully nowcast LI events within SPC slight risk or greater regions. Green bars reflect Pre-CI Cloud Growth, yellow bars reflect CI likely category, and red reflect CI occurring category.

The validation study focused on the Storm Prediction Center severe storm risk areas for 23 convective afternoons and 11 convective nights over the Southern and Central Plains during April, May, June, and one night in July during 2008 and 2009. Within the SPC severe storm risk area, the mean POD is 56.3% and the mean FAR is 25.5% (47.0% POD and 34.8% FAR for entire validation domain). Analysis of the outlying days with POD/FAR above or below one standard deviation of the respective mean reveals that the UWCI algorithm performs 1) better in certain regimes such as with storms developing in previously clear to partly cloudy skies and with storm development along sharp boundaries and 2) poorer in other regimes such as scenes covered with midlevel cloud layers, cirrus shields, existing convective anvils, and fast cloud motion. The analysis showed the "pre-CI cloud growth" nowcast category offers the largest lead-times of the three nowcast categories (see Figure 3.2-3), but also has a highest FAR. The "CI Likely" and "CI Occurring" nowcast categories show progressively shorter lead-times, respectively. The lead-times grow shorter with the CI Likely and CI Occurring categories since these

nowcasts are capturing developing convection further along in the development process lifecycle, but have similarly lower FAR.
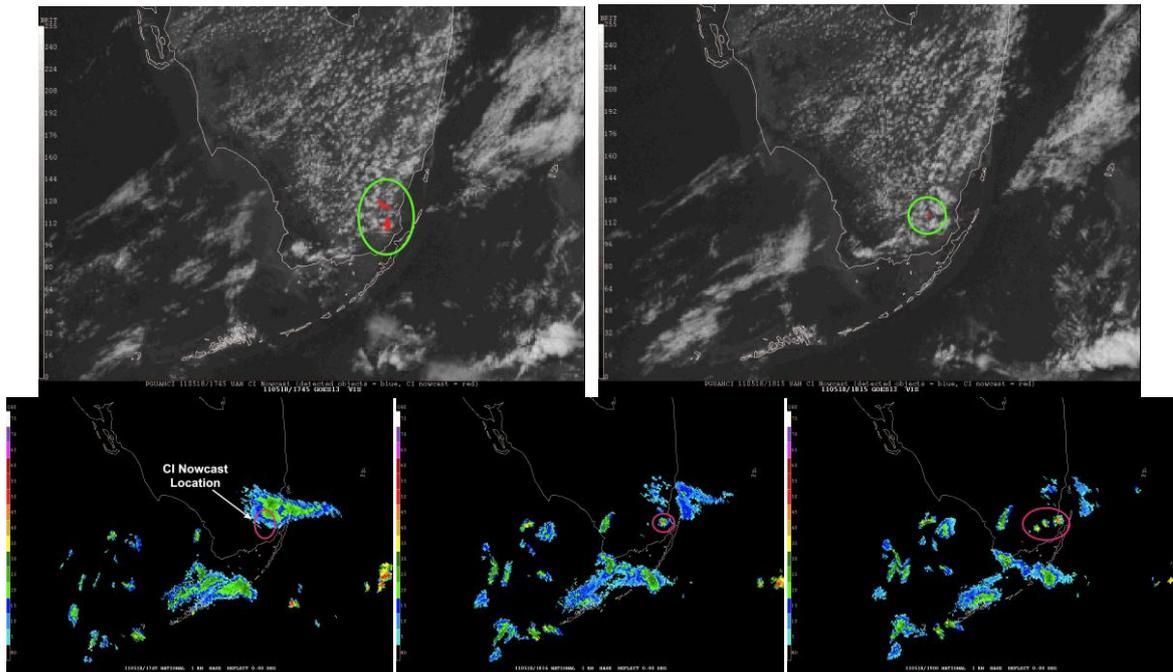
Figure 3.2-4: demonstrates how the SATCAST algorithm performs, in this case over far southern Florida, providing a 45-51 minute advanced lead-time nowcast for the first occurrence of a ≥35 dBZ radar echo. In the top two images, the SATCAST is highlighting a few cumulus clouds (red pixels) that are nowcasted for CI. The bottom sequence of radar images shows the new showers (which unlikely had lightning at this time) that eventually developed. A ≥35 dBZ radar echo formed ~45-51 minutes after the red-highlighted clouds were identified by SATCAST.

In 2009, work began to develop an "object tracking" approach to the SATCAST CI nowcasting algorithm (Figure 3.2-2), as documented and validated in Walker et al. (2011). SATCAST with object tracking has become the NOAA/GOES-R Algorithm working Group's AWG) official CI algorithm, and it currently nearing the end of its initial development phase as an "Option 2" GOES-R product. In this final stage of maturity, only minor enhancements or additions are planned for adjusting the algorithm before the 100% delivery. However, once this delivery is made, even with fulfilled AWG requirements, critical improvements to the official algorithm are needed, which include: (a) further development of a night time component, (b) improved methods for using specific interest fields based on observed weather and airmass variability, and (c) increasing understanding of how environmental factors influence infrared observations made by satellite. The CI algorithm theoretical basis document (ATBD) as part of the NOAA AWG provides a high level description of, and the physical basis for, the assessment of convection initiation derived from the Advanced Baseline Imager (ABI) flown on the GOES-R series of NOAA geostationary meteorological satellites. The CI algorithm provides an assessment of the clouds that may precipitate. The CI algorithm is designed to monitor the growth of non-precipitating clouds, and once a series of spectral and temporal thresholds are met, that cloud is identified as likely to have a radar reflectivity greater than 35 dBZ within 0-2 hours. The AWG CI algorithm produces a binary field at 2 km spatial resolution of areas where CI has a high likelihood of occurring. The product uses an IR T_B spectral thresholding technique, which tracks clouds within their early stages of development, and

monitor their spectral characteristics. If a large majority of the spectral "interest fields" thresholds are exceeded, then the pixels within the cloud object are flagged for having a high likelihood for CI. A nowcast example of SATCAST with object tracking is shown in Figure 3.2-4.

Specifically, one such component of the algorithm that needs enhancement is that which identifies and follows the same satellite-derived cloud "objects" between subsequent images, known as the "object-tracking" routine. The current algorithm employs a simple temporal-overlapping method for this in which identified cloud objects from one image are superimposed onto an array of cloud objects from the next image. Where there is overlap between two objects in the superimposed image, the objects are considered to be the same object from each of the two input image times. Because of the high temporal resolution of the GOES-R ABI (2 km in the infrared), it is reasonable to assume that most objects can be tracked via this method, since object overlap between two closely timed images is relatively easy to achieve.

3.3 MSG Interest Fields, as Related to Physical Processes in Growing Cumulus Clouds

In its application to GOES, the SATCAST algorithm uses 8 different so-called interest fields, all based on infrared data, which different levels of information regarding a possibly fast growing cumulus cloud (see Mecikalski et al. 2008). These indicators define a simple, per-cumulus cloud pixel or object, threshold-based scoring system, where the sum of all scores, i.e. where the respective critical value is met, identifies cumulus clouds that will soon grow into mature storms. Recent work by Mecikalski et al. (2010a,b) describes the use of SEVIRI IR and visible reflectance fields for optimizing CI nowcasting in SATCAST. Beginning with 91 possible IR interest fields per cumulus cloud object, and 27 reflectance and texture-based fields in reflectance and high-resolution visible (HRV) data, a small subset of fields were identified as containing the most information when describing three main physical attributes of pre-CI cumulus clouds. These physical attributes are: (1) in–cloud updraft strength (an inferred physical process), (2) cloud depth, or the height of the updraft, and (3) cloud–top glaciation. The IR interest fields are shown in Table 3.3-1, while the visible reflectance, cloud texture fields are shown in Table 3.3-2. All SEVIRI channels are available on the nominal 3 km sampling distance, while only the HRV channel has the 1 km sampling distance.

Rank	CI Interest Fields	Mean	Standard Deviation
	Cloud Depth		
1	6.2–10.8 µm	−14.6	11.27
2	6.2–7.3 µm	−6.6	5.94
3	10.8 µm T_B	242.5	16.79
4	7.3–13.4 µm	5.4	4.42
5	6.2–9.7 µm	−8.4	3.40
6	8.7–12.0 µm	0.3	1.92
	Glaciation Indicators		
1	15-min Tri-Spectral	0.7	2.02
2	Tri-Spectral	−0.6	1.94
3	15-min 8.7–10.8 µm	0.5	1.47
4	8.7–10.8 µm	−0.1	1.55
5	15-min 12.0–10.8 µm	0.2	1.05
6	15-min 3.9–10.8 µm	0.3	0.24
7	12.0–10.8 µm	−0.5	1.15
	Updraft Strength		
1	30-min 6.2–7.3 µm	7.2	4.92
2	15-min 10.8 µm T_B	−12.1	9.44
3	30-min 10.8 µm T_B	−20.4	13.54
4	15-min 6.2–7.3 µm	4.3	3.58
5	30-min 9.7–13.4 µm	4.9	4.31
6	30-min 6.2–10.8 µm	14.5	8.78
7	15-min 6.2–12.0 µm	8.0	6.32
8	15-min 7.3–9.7 µm	−3.3	4.02

Table 3.3-1: MSG satellite related IR interest field that were preliminarily evaluated for use within the SATCAST algorithm. A total of 21 possible indicators may be used. Here, units are K. The attribute or physical process that each interest field helps identify is shown.

The work by Mecikalski et al. (2010a) expanded the GOES-focused SATCAST algorithm to operate on Meteosat Second Generation (MSG) SEVIRI data, in advance of the Advanced Baseline Imager on GOES-R. A total of 67 IR CI interest fields are initially assessed in MSG SEVIRI data for containing information on three attributes of growing convective clouds: cloud depth, updraft strength and cloud-top glaciation. Through correlation and principal component analyses, 21 fields out of the 67 are identified as containing the least amount of redundant information. Using between 6 and 8 fields per category, two methods are proposed on how growing convective clouds may be quantified per MSG pixel (with 3 km scaling distance), or per cumulus cloud object, toward monitoring cumulus cloud development. In Table 3.3-1, the 6.2–10.8 µm (Schmetz et al., 1997) difference has the highest ranking when estimating cumulus cloud depth, with the 6.2–7.3 µm difference and 10.8 µm T_B the second and third on the list, respectively. Table 3.3-1 shows the top three fields as the 15-min trend in the tri-spectral difference [(8.7–10.8)–(10.8–12.0)], the instantaneous tri-spectral difference, followed by the 15-min 8.7–10.8 µm time trend, all physically consistent, well-documented indicators of cloud-top glaciation (Baum et al., 2000b). The 30-min 6.2–7.3 µm difference, and the two time trends of 10.8 µm T_B (as in Roberts and Rutledge, 2003) as highly ranked IR fields for estimating updraft strength, and hence cumulus cloud growth rates in advance of CI. The cited literature highlights the physical interpretation of a given channel difference or time trend. In contrast, several fields not documented in the literature are shown to possess unique value when monitoring cumulus cloud growth and evolution. These include: (a) 8.7–12.0 µm difference, (b) the 6.2–7.3 µm difference, (c) 6.2–9.7 µm difference, (d) 7.3–13.4 µm difference, (e) 30-min 9.7–13.4 µm trend, (f) 15-min 7.3–9.7 µm trend, (g) 15-min 6.2–7.3 µm trend, and (h) 30-min 6.2–7.3 µm trend (Table 3.3-1).

Mecikalski et al. (2010b) developed understanding on how visible data can be used to monitor growing cumulus ahead of CI. A total of 27 IR CI interest fields were initially assessed for containing reflected and brightness variability (BV) information. The reflectance fields ultimately help determine cloud-top glaciation, related in many cases to

changes in particle size and the formation of ice hydrometeors, while BV fields diagnose the presence of active convective clouds that further correlate to updraft vigour. Through correlation and principal component analyses, 11 fields [5 peak detection (PD), 6 reflectances, Refl] out of 27 initial fields are identified as containing the least amount of redundant information. The main findings include: (1) Time trends of decreasing $Refl_{1.6}$ and $Refl_{3.9}$ correlate well to growing cumulus clouds undergoing CI, with 15-min trends of reflectance being near –0.83 to –0.81% for both channels. Thirty-minute trends for $Refl_{1.6}$ and $Refl_{3.9}$ are –4.8% and –2.6%, respectively. (2) Cloud-top reflectances at or below 3.6% as measured at 3.9 μm appears to be a good indicator that ice hydrometeors are in abundance, and a phase change has occurred. (3) Higher PD indicates the presence of a cumulus field, or the highly non-uniform brightnesses produced by cumuli against an otherwise darker or uniform background. (4) Data in the highly correlated 0.6 and 0.8 μm channels, although indicators of optical depth changes as clouds deepen, appear to be insensitive to cloud development and are not valuable indicators alone of growing convective clouds. Yet, (5) $Refl_{0.6}$ and its time rate of change, have more value for describing cloud-top conditions for warmer, lower cumulus clouds as compared to clouds more likely to contain significant percentages of ice hydrometeors. Several methods are proposed on how growing convective clouds may be quantified per cumulus cloud object, towards monitoring cumulus cloud growth rates, and to perhaps nowcast CI over 1 hour timeframes.

Interesting aspects of
Table *3.3-2* are the last five fields, which represent a measure of contrast within 1 km resolution images (i.e. the texture). The interpretation of these "peak detection" (or a measure of scene "texture") fields is 30-60 minutes prior to CI scattered cumulus clouds are likely to be present in otherwise clear skies, against a background of a darker surface (which causes high brightness contrast). These texture fields exemplify the high value in HRV data for characterizing cumulus clouds, which comes as no surprise given past research (e.g., Purdom 1976, 1982), the quantified importance of 1 km resolution data in convective cloud masks (see Berendes et al., 2008), and given the known ~1 km^2 scale of the cumulus cloud.

Rank	Interest Fields	Mean	Standard Deviation
1	30-min Trend $Refl_{0.6}$	0.0124	0.077
2	15-min Trend $Refl_{0.6}$	0.0071	0.051
3	30-min Trend $Refl_{1.6}$	−0.0214	0.059
4	15-min Trend $Refl_{1.6}$	−0.0670	0.035
5	$Refl_{3.9}$	0.0273	0.042
6	$Refl_{1.6}$	0.1238	0.104
1	9 x 9 PD_{ave} 30 min Previous	14.89	22.0
2	9 x 9 PD_{ave} 15 min Previous	16.00	25.0
3	9 x 9 PD_{ave} Current Time	14.07	21.2
4	9 x 9 PD_{pert} 15-min Previous	9.66	15.6
5	9 x 9 PD_{pert} 30 min Previous	9.20	16.0

Table 3.3-2: Mean and standard deviation values for the VIS/NIR interest fields that describe cumulus cloud-glaciation through reflectance changes. Fields are listed by order of importance or value. Mean and standard deviations are in fractional reflectance, from 0-1. Units of the peak detection (PD) fields are in brightness counts, 0-255. Higher PD or "peakiness" will occur within a field of lumpy, developing cumulus clouds versus cumulus with weaker updrafts that are developing more slowly and have smoother tops.

3.4   Evolution of Retrieved Cloud Properties for Growing Cumulus Clouds

The study by Mecikalski et al. (2011) was toward understanding how satellite retrieved products designed to describe cloud properties evolve during convective cloud growth, with respect to the formation of heavy rainfall within the 1–hour timeframe. It utilizes retrieved fields from the Optimal Cloud Analysis (OCA; Watts et al., 1998) algorithm, relying on Meteosat Second Generation (MSG) data sets as input. Four retrieved fields are analyzed at 5–min time resolution with respect to growing convective clouds: (1) cloud optical thickness (τ), (2) cloud phase, (3) effective radius of cloud–top particles (r_e), and (4) cloud-top pressure (p_c). Minimizing the "cost function" (J_m) is central to the OCA processing and a small J_m implies robust algorithm solutions; J_m is evaluated as part of this study, and will be described in detail below. Each field provides some level of unique information for this analysis. Since the cloud phase is a binary indicator (0 for water, 1 for ice) based on the other fields, our analysis will not focus on its use since analysis of τ, r_e, p_c and J_m fields provide more physical understanding.

The main reasons for retrieving cloud properties from satellite include enhancing understanding of radiative forcing impacts on climate (Minnis et al. 1998, 1999, 2004a; Dong et al. 2005, 2006; Yuan et al. 2008), verifying convective parameterization methodologies and assessing convective storm behaviour (Lindsey et al. 2006; Rosenfeld et al. 2008; Fan et al. 2009), and increasing understanding of the atmosphere as a whole with respect to clouds (Duda et al. 2001; Lopez et al. 2009). Time series analysis of retrieved τ, r_e, cloud phase and p_c have been evaluated on scene–by–scene time scales from AVHRR in the evaluation of clouds with respect to climatological datasets like those for the International Satellite Cloud Climatology Project (ISCCP; Rossow and Schiffer 1991, 1999). Cloud property retrievals from GOES have been used in aviation applications related to icing (Smith et al. 2000; Dong et al. 2002; Smith et al. 2002, 2003; Minnis et al. 2004b), and for enhancing numerical weather prediction models (Weygandt et al. 2006).

A main goal of Mecikalski et al. (2011) was to determine how OCA retrieved fields behave for growing convective clouds, at 5–min temporal resolution, and how they may be used to understand in–cloud processes related to physical aspects of cumulus cloud growth, which include updraft strength and phase changes related to r_e changes, τ as a function of cloud depth, and cloud longevity. Identifying these interactions will help extend our understanding of cloud-top–in-cloud relationships, to promote the use of OCA (or OCA–like) products for convective cloud diagnosis, and to eventually incorporate retrieved microphysical fields within algorithms that nowcast (0–1 hour forecast) new thunderstorm formation or intensity.

Several main questions are addressed when analyzing OCA fields for 94 growing convective cloud events: (1) What are the behaviours of the OCA fields (phase, τ, p_c, r_e, J_m) as clouds evolved over 30–min intervals as cumulus clouds? (2) What are the relationships between 5–30 min rates of change of OCA fields and other IR indicators that infer physical processes in growing cumulus (cloud depth and updraft strength)? (3) Are τ time change rates valuable indicators of cloud evolution? (4) Can J_m be used as an early indicator of cloud-top glaciation? Specifically, does an increasing J_m imply the beginning of the mixed phase at cloud top? Over the following two sections these questions will be addressed as the 94 events are examined. An example of the spatial patterns of the τ, r_e and p_c fields is shown for 1320 UTC 25 May 2009 over a large section of Europe in Figure 3.4-1 (b)-(d), with an accompanying true colour image (Figure 3.4-1 (a)).
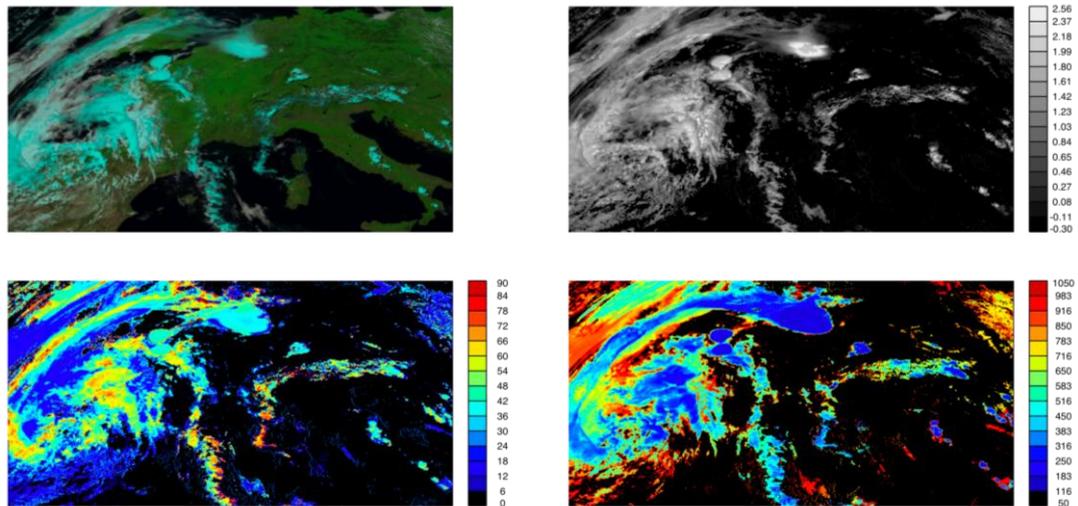
Figure 3.4-1: (a) to (d), clockwise from top–left, an example of a regional plot of a true colour image (red the 1.6 μm channel on SEVIRI, green 0.8 μm, and blue 0.6 μm), Log10 cloud optical thickness (τ), r_e (μm), and cloud top pressure (p_c; hPa). All data are for 1320 UTC 25 May 2009, with all parameters plotted without quality control applied except to omit cases with Log10 τ < −0.3 (τ<0.5).

Four individual, representative events from the 94–cloud population in Mecikalski et al. (2011) are shown in Figure 3.4-2 (a)-(d). For these events, spread over a 30–minute time window, not all clouds were necessarily progressing through the same stage of development, and therefore, the discussion will focus on relationships between fields rather than how fields relate to specific times.

For all events, the following features are found: (1) τ values increase over time, exhibiting a positive time rate of change, often exhibiting a sudden jump in magnitude over 5–10 min periods, (2) p_c values decrease as clouds deepen, beginning near 80 kPa in Figure 3.4-2 (a) and (b), (3) r_e values show two trend types: to generally increase (Figure 3.4-2 (b) and (c)), or a decrease then increase (Figure 3.4-2 (a) and (d)), and (4) J_m values tend to show a distinct maxima which precedes or is coincident with an increase in both r_e and τ values. We interpret these behaviours as the phase change occurring near the increase or spike in J_m, with cloud deepening denoted by the rapid increase in τ, to >250 in Figure 3.4-2 (d). Recall from above, the peak in J_m signifies the OCA algorithm's inability to fit a solution to either a pure water or a pure ice model for hydrometeors, and represents a non–physical way of identifying the clouds deepening and glaciating.
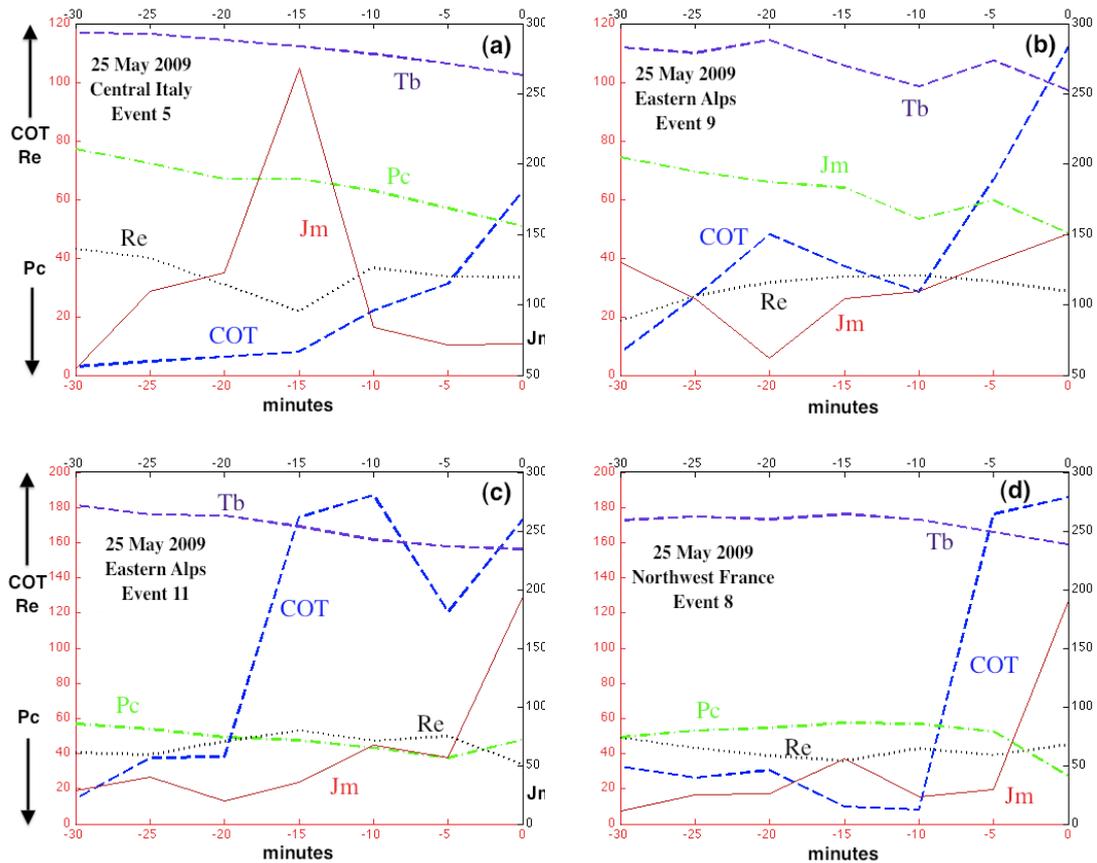
Figure 3.4-2: OCA quantities cloud optical depth (COT or τ), cloud top pressure (Pc), particle effective radius (Re) and function cost (Jm) for individual growing cumulus cloud events within the 94–storm database). Also plotted here is the 10.8 µm brightness temperature (Tb) for the single coldest pixel in the 3 x 3 analysis box.

Also plotted on Figure 3.4-2 are 10.8 µm T_B values for the coldest pixel in the 3 x 3 analysis box for the cumulus clouds examined. These temperatures mimic the p_c trends well, decreasing by 10 to >35 K over the 30 minute period. One issue likely confounding these results are slight changes in the cumulus cloud target over the analysis time, specifically, what is the character of the cumulus clouds within respect to a target box (the three coldest 10.8 µm pixels) from time to time, which is apparent in Figure 3.4-2 (b) (the wavering behaviour in T_B between −10 and 0 min), and in Figure 3.4-2 (c) (the sudden decrease in τ at −5 min). Specifically, the cloud tops may warm and cool slightly as clouds do not filling an entire pixel, or as a cloud becomes span by adjoining IR pixels. We consider these artifacts unavoidable as clouds evolve, and as circular cloud features are being observed by SEVIRI pixels (in contrast to fitting surfaces to the cloud parameters).

3.5   First-Flash Lightning Initiation Indicators and Interest Fields

The study by Harris et al. (2010) developed two components related to nowcasting the first flash (defined in this section as "lightning initiation") from a new convective cloud, used GOES infrared and reflectance data: (1) determination of lightning initiation (LI) signatures within geostationary imagery, so to assess the value in LI 0-1 hour nowcasting, and (2) developing an understanding on how radar (dual-polarimetric), satellite and lightning-mapping array data are inter-related in space and time. The conceptual framework of this research is shown in Figure 3.5-1.

Within cumulus cloud fields that develop in conditionally unstable air masses, only a fraction of the cumuli may eventually develop into deep convection. Identifying which of these convective clouds is most likely to generate lightning often starts with little more than a qualitative visual satellite analysis. Observed satellite infrared (IR) signatures associated with growing cumulus clouds prior to the first lightning strike, so–called lightning initiation (LI), can be identified. The behaviour of ten Geostationary Operational Environmental Satellite (GOES–12) IR interest fields in the 1-hour in advance of LI were analyzed. A total of 172 lightning–producing storms that occurred during the 2009 convective season were manually tracked and studied over four regions: Northern Alabama, Central Oklahoma, the Kennedy Space Center and Washington D.C. Four–dimensional and cloud–to–ground lightning array data provide a total cloud lightning picture (in–cloud, cloud–to–cloud, cloud–to–air, cloud–to–ground) and thus precise LI points for each storm in both time and space.
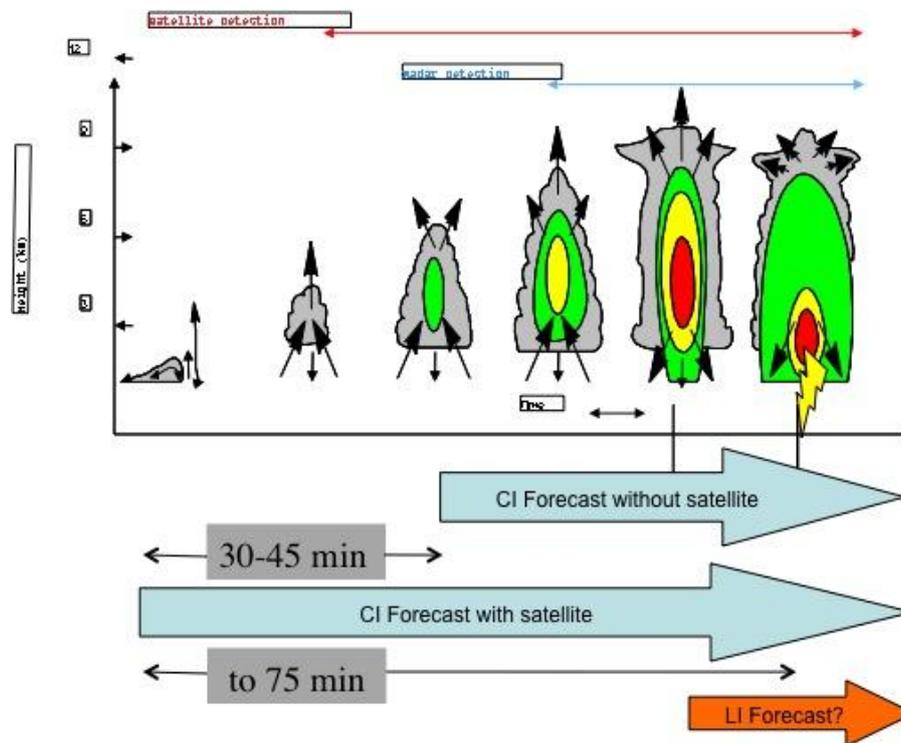

Figure 3.5-1: Conceptual framework for first-flash lightning initiation nowcasting using satellite data.

The main results from Harris et al. (2010) are that upon the examination of 172 LI events over the four LMA networks in GOES IR LI interest fields (IFs), 8 out of 10 LI IFs considered have at least some unique value in identifying LI across all regions. Statistical significance tests were performed as a means of quantifying IF uniqueness. Similar to Siewert (2008), specific IF median values were computed from the results above, as shown in Table 3.5-1. These median-value LI results are shown along with the MB06 CI thresholds (based on examination of many events, including null CI cases, which was not done here); therefore, the MB06 results can only be qualitatively compared to those found in Siewert (2008) and outward of this study. These results are applicable for evaluation within a real–time satellite–based system that monitors for LI.

The 15–min 3.9 – 10.7 temperature difference trend and the Refl$_{39}$ trend are the two fields that showed relatively little unique value when GOES IR data were analyzed in advance of LI (hence why 8 of 10 LI IFs are considered valuable). Additionally, the 15–min 6.5 – 10.7 and 13.3 – 10.7 temperature difference time trends did not provide much added information. Overall, the 15–min trend IFs provide more awareness to imminent LI. Most fields appear fairly predictive at 15 to 45 min before LI, with an average lead–time for all fields and regions near 35 min.

Interest Field	MB06 Critical CI Value	Siewert LI Value	15 to 30–min Threshold (This LI Study)	Description
10.7 μm T$_B$	< 0°C	≤ –13°C	< 0° C	Cloud tops cold enough to support supercooled water and ice mass growth; cloud–top glaciation
10.7 μm T$_B$ Time Trends[1]	< –4°C / 15 min (ΔTb / 30 min < ΔTb / 15 min)	≤ –10°C / 15 min	< –6° C / 15 min	Cloud growth rate (vertical)
Timing of 10.7 μm T$_B$ drop below 0° C	Within prior 30 min	Not used	Not Used	Cloud–top glaciation
6.5–10.7 μm T$_B$ difference	Tb Diff: –35°C to –10°C	≥ –17°C	> –30° C	Cloud top height relative to mid/upper troposphere
13.3–10.7 μm T$_B$ difference	Tb Diff: –25°C to –5°C	≥ –7°C	> –13° C	Cloud top height relative to mid/upper troposphere; better indicator of early cumulus development but sensitive to cirrus
6.5–10.7 μm T$_B$ Time Trend	> 3°C / 15 min	≥ 5°C / 15 min	> 5° C / 15 min	Cloud growth rate (vertical) toward dry air aloft
13.3–10.7 μm T$_B$ Time Trend	> 3°C / 15 min	≥ 5°C / 15 min	> 4° C / 15 min	Cloud growth rate (vertical) toward dry air aloft
3.9–10.7 μm T$_B$ Difference[3]	Not used	Not used	> 17° C	Cloud–top glaciation
3.9–10.7 μm T$_B$ Time Trend[2]	Not used	T–T(t-1) < –5°C and T–T(t+1) < –5°C	> 1.5° C / 15 min	Sharp decrease, then increase indicates cloud–top glaciation
3.9 μm Fraction Reflectance[2]	Not used	≤ 0.05	< 0.11	Cloud top consists of ice (ice is poorer reflector than water at 3.9 μm)
3.9 μm Fraction Reflectance Trend[3]	Not used	Not used	< –0.02 / 15 min	Cloud–top glaciation rate

1 Represents two unique 10.7 μm T$_B$ interest fields in MB06. No 30-min trends were used in Siewert (2008) or in this study.
2 Added to MB06 fields by Siewert (2008).
3 Unique to this study.

Table 3.5-1: GOES infrared and 3.9 μm reflectance interest fields.

Given the roughly 35–min average lead–time for LI the IFs provide, use of the IF medians and means for LI–15 to LI–30 min determines the values in Table 3.5-1. The LI IF values found here are less restrictive than Siewert's (2008) LI values for two reasons: (1) Siewert (2008) examined convective storms only ≤15 min before LI. Since the LI–0 and LI–15 median values in this study match Siewert's IF values very closely, we feel these two studies corroborate the hypothesis that GOES IR IFs can indeed be used to predict LI. And, (2) this present study makes use of a much larger dataset of LI events (172 versus ~12). With a small database, more extreme values are expected, while smoothing of extreme values occurs as more events are included.

49
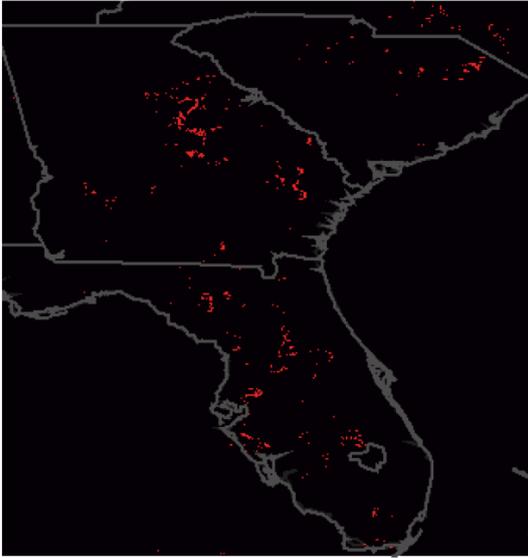
CI Nowcasts

LI Nowcasts (or regions where lightning flash rates will be high)
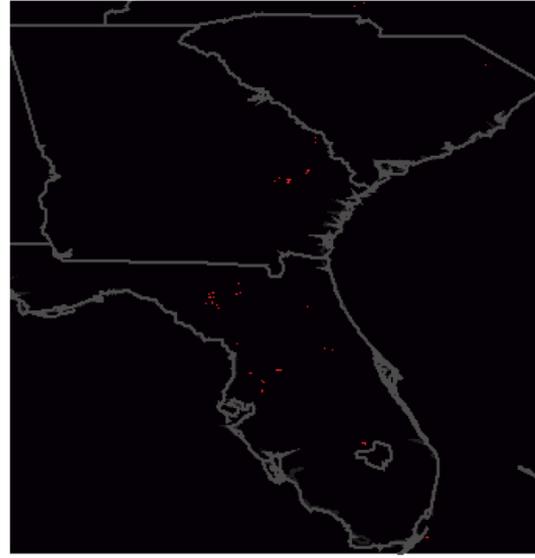

2045 UTC 17 June 2009

Figure 3.5-2: Preliminary comparison between CI and first-flash LI nowcasts made with the SATCAST algorithm, for one test period.

Individual LI cases appear to have very similar tendencies, as for example with the 3.9 – 10.7 and 13.3 – 10.7 temperature difference 15–min trends. However, our analysis noted that the largest tendencies often occur at different times in a storm's development, which is likely related to conditions in the ambient environment of a given storm (e.g., instability, the shape of the instability, water vapour profiles). Therefore, use of IFs that appear to provide similar information over a population of events may in fact add valuable information on a case–by–case basis. A preliminary example of a first-flash LI nowcast is shown in Figure 3.5-2.

3.6   Application to MTSAT

The Japanese Meteorological Agency (JMA) has developed a similar product ("Rapidly Developing Cumulus Areas Product"), operationally derived from the Japanese geostationary satellite MTSAT. The following sections shortly describe this work.

3.6.1   Rapid Scan Operations of MTSAT-1R

JMA began rapid-scan operation using MTSAT-1R in 2011 to capture short-lived but severe weather phenomena so that aviation users can be informed of them in advance. As shown in *Table 3.6-1: Specifications of rapid-scan operationsTable 3.6-1*, observations are made in a small area around Japan from 00 UTC to 09 UTC at five-minute intervals in the summer season during operation.

Observation interval	5 minutes
Time	Daytime only (00:00 to 09:00 UTC)
Period	Summer only (1 June to 30 September)
Objective	To provide information for aviation safety
Observation area	Bounding box around Japan

Table 3.6-1: Specifications of rapid-scan operations

3.6.2 Algorithm of the Rapidly Developing Cumulus Areas Product

Rapidly Developing Cumulus Areas (RDCAs) indicate the potential for heavy rainfall and a key technique in RDCAs identification involves detecting temporal increases in the asperity and altitude of the cloud top surface. VIS data are especially fundamental for checking for temporal increases in asperity at the cloud top surface. Figure 3.6-1 shows rapidly developing cumulus clouds, which are observed in satellite images as their top height and surface roughness increases. As the cloud top rises, the brightness temperatures of infrared images decrease and the brightness of visible images increases. As cloud surface roughness develops the variation of bright and dark satellite image pixels increases.
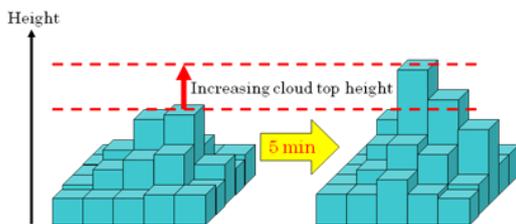

Figure 3.6-1: Schematic diagram of cloud top height and roughness variation for developing cumulus. Each small cube corresponds to one satellite image pixel.

For the detection of developing Cu clouds, the 6 interest fields (parameters) listed in Table 3.6-2 are used. Some of these are taken from the Convective Initiation (CI) product described in section 3.3

No.	Parameter	Main Objective
1	VIS reflectance difference between maximum and average	Evaluation of roughness in and around developing cumulus cloud
2	VIS reflectance standard deviation	
3	10.8 µm brightness temperature difference between minimum and average	
4	10.8 µm brightness temperature standard deviation	
5	Temporal variation of VIS reflectance average	Evaluation of vertical development
6	Temporal variation of 10.8 µm brightness temperature average	

Table 3.6-2: Parameters used in RDCAs

The values of each parameter x_1 to x_6 are used in a multiple logistic regression analysis, yielding coefficients a_0 to a_6, which are determined in reference to lightning strike data obtained from ground-based observations made on 10, 11, 12 and 13 July 2011. These

51

coefficients are applied to many other cases in order to obtain the probability of convective cloud development. Figure 3.6-2 illustrates this concept.
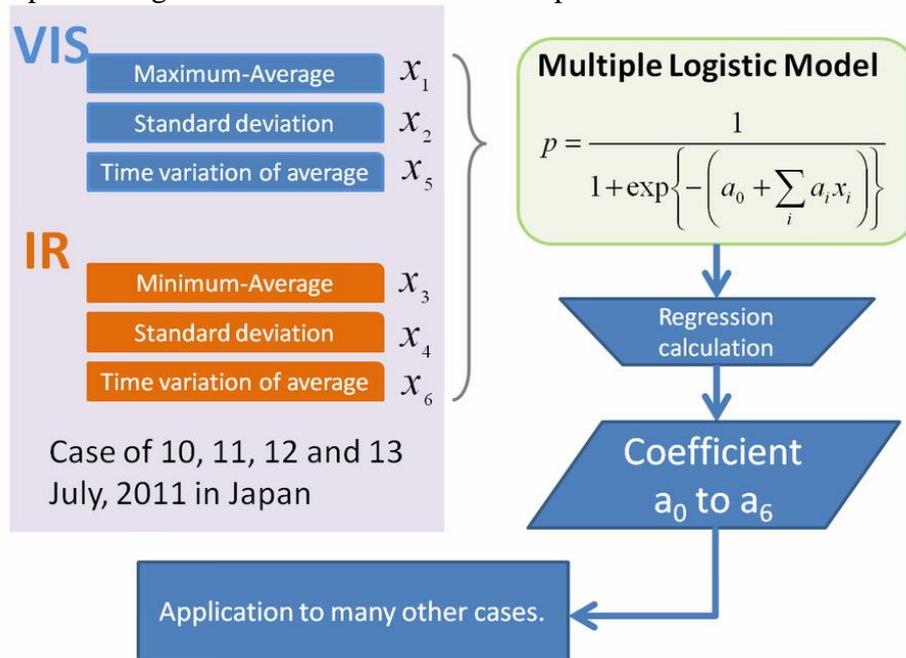
Figure 3.6-2: A multiple logistic regression model is adopted to obtain the probability index for a convective cloud to develop to full Cumulonimbus stage.

3.6.3 Evaluation of RDCA

The results of RDCAs evaluation performed in summer 2012 in relation to lightning observation are shown in Figure 3.6-3 and Figure 3.6-4. The hit rate (derived from dividing the number of hits by the sum of the number of hits and false alarms) was 39% on average in Figure 3.6-3. Similarly, Figure 3.6-4 shows POD (derived from dividing the number of captures by the sum of the number of captures and misses). An average of POD was 42% in that season.
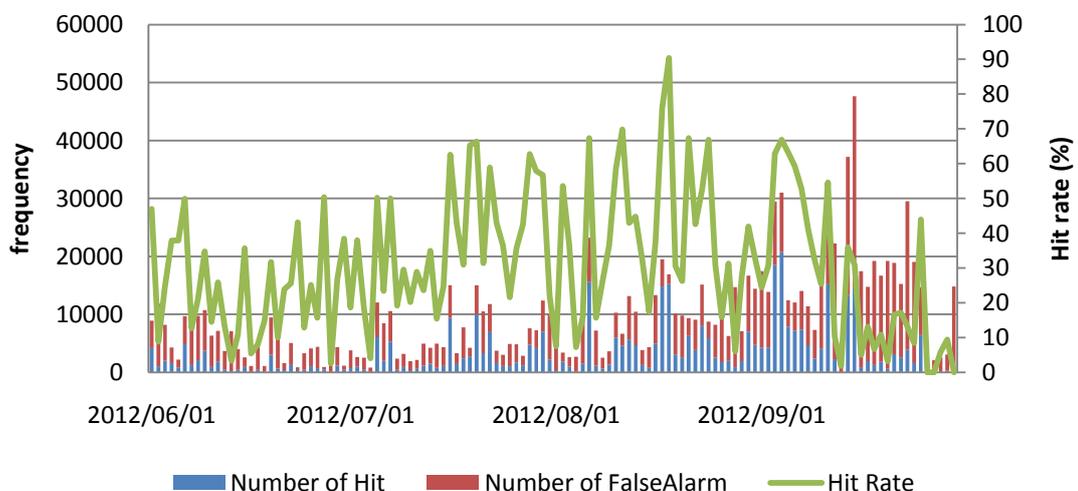
Figure 3.6-3: Time series of hit rate. Bars show frequency, solid line the hit rate. Plotted are daily

52

data between 01 June and 30 September 2012.

Figure 3.6-4: Time series of probability of detection (POD). Bars show frequency, solid line shows POD. Plotted are daily data between 01 June and 30 September 2012.

3.6.4 Final RDCA Product for Aviation Users

The information of RDCAs was provided for aviation members on a web based interface. Figure 3.6-5 shows the final product, for an example in 2012. It is called "Convective Cloud Information." It includes RDCAs, and meanwhile other information is also included in Figure 3.6-5. These are "Cumulonimbus Area" and "Mid/Low Cloud Unknown Area" (not explained here). Results of RDCAs are represented as green.
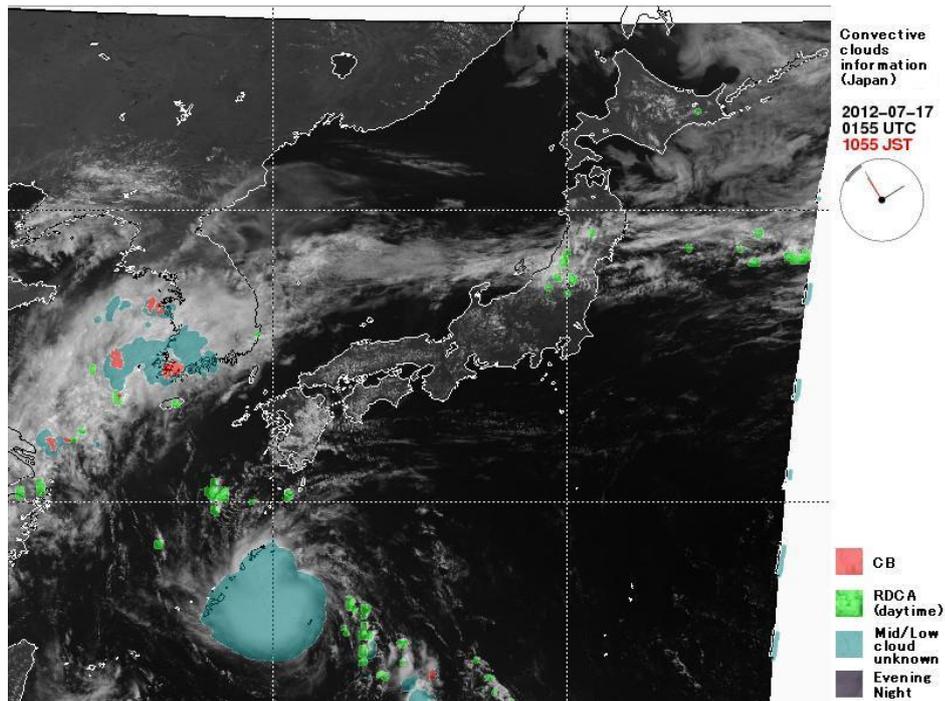
Figure 3.6-5: Convective Cloud Information as presented to users. RDCAs are overlaid in green over the VIS satellite image for this daytime example. Other colours refer to other cloud products, not discussed here. (Legends are in Japanese in the original product).

4 MATURE STORM CHARACTERISTICS: HOW LONG WILL A STORM LAST AND HOW HAZARDOUS IS IT?

Soon after the convective initiation stage, the cumulus cloud top reaches its equilibrium level near the tropopause region. The tropopause is characterized by strong static stability, so the vertical motions in the updraft are forced horizontally, continually transporting ice crystals laterally and forming a cirrus anvil cloud. Cumulus with particularly strong updrafts can penetrate into and above the tropopause, producing a feature known as an "overshooting top". The updraft interaction with the stable tropopause region produces gravity waves. When the gravity waves break, hazardous turbulence for aviation occurs and ice crystals can be forced into the stratosphere, producing a phenomenon known as "jumping cirrus". The horizontal dimension of the cirrus anvil is modulated by the updraft intensity, storm lifetime, wind speed at cloud top, and environmental inertial stability of the outflow region.

Much can be learned about the intensity, severity, cloud top height, potential lifetime, and precipitation rate of/within a mature convective storm from passive visible and IR satellite imagery. Overshooting top locations are evident in visible imagery and can be inferred from multispectral IR in addition to stratospheric moisture plumes produced these features. Persistent overshooting tops can produce a feature in IR imagery called a "cold-" or "enhanced-U/V" signature, which indicates that the storm may be producing large hail, damaging winds, and/or a tornado. Multispectral IR data can be used in combination with a NWP model temperature profile to estimate the cloud top height of the storm core and cirrus anvil. The rate of lateral anvil cloud expansion can be used to infer the lifetime of the storm. Signatures within multispectral IR data can be calibrated with ground-based weather radar data to derive precipitation rates.

The following sections will describe satellite-based research of mature convective storms using passive visible and IR channel data that will expand upon many of the features and processes described above. Emphasis will be directed toward description of recent objective detection algorithms that can benefit the nowcasting community.

4.1 Storm Intensity Indicators: Coupled IR and Lightning Diagnostics

New research involves coupling current GOES and MSG satellite spectral information used to determine cumulus cloud and growth with data that mimics that to be collected by the GLM [based on TRMM's Lightning Imaging Sensor (LIS)] or MTG LI towards identifying the correlation between strong updrafts, lightning intensity, and thunderstorm severity. This project will produce a satellite-based "storm severity index" product designed to substantially enhance our ability to isolate updrafts within thunderstorms, and the related hazards that accompany the occurrence of strong updrafts within active portions of convective storms, specifically heavy rainfall, frequent cloud-to-ground lightning, overshooting tops (and hence locations that generate severe turbulence aloft for aircraft), and subsequent ground-level heavy rainfall, and microbursts (caused by the collapse of updraft cores).

Using MSG SEVIRI IR data over tropical Africa for 2-3 months, information gained from recent research (Mecikalski et al., 2009; Siewert et al., 2009), along with total lightning data from TRMM LIS via the "Global Total Lightning Flash" product, correlations in space and time will be developed between CI/LI "interest fields, " strong cumulus cloud growth

and intense lightning. Cumulus clouds will be identified using the algorithm of Berendes et al. (2008) and the GOES-R cloud-typing algorithm. Given the degree of correlation between IR fields (e.g., 10.8 μm T_B cloud-top cooling rates; 6.2–7.3 μm, 6.2–10.8 μm to identify updraft depth; 8.5–10.8 μm and 3.9 μm reflectance for cloud-top glaciation), lightning frequency and cumulus clouds, we expect to be able to pin-point new and strong/severe storms on spatial scales of 3 km (the MSG footprint near the Equator). NWP data will assist by providing CAPE and CIN (to determine environments capable of supporting storm storms) and precipitable water (to estimate rainfall rates and microburst potential). The severity index product is a forthcoming GOES-R capability, one that takes advantage of the expected high temporal, spatial and spectral resolution the ABI and GLM will provide.

For the analysis, convective events are chosen from the precipitation feature database for the months of January and August 2007 over tropical Africa and eastern tropical Atlantic. Storm intensity is determined using the TRMM precipitation radar. Currently, intensity is being defined by the Ice Water Path (IWP) with reflectivities >40 dBz between 6 and 10 km (a mixed phase region important for lightning initiation). IWP is calculated for every precipitation feature over both land and water, making useful statistics when analyzing TRMM LIS and MSG imagery. TRMM LIS data is converted to flash rates by combining all the flashes for one IWP sample using a nearest neighbour technique and dividing by the average observation time (typically ~90 s). Black dots represent lightning flash location in Figure 4.1-1.

MSG data will be collected for each IWP sample time along with an hour of data before and after, allowing for temporal trends of convective interest fields.
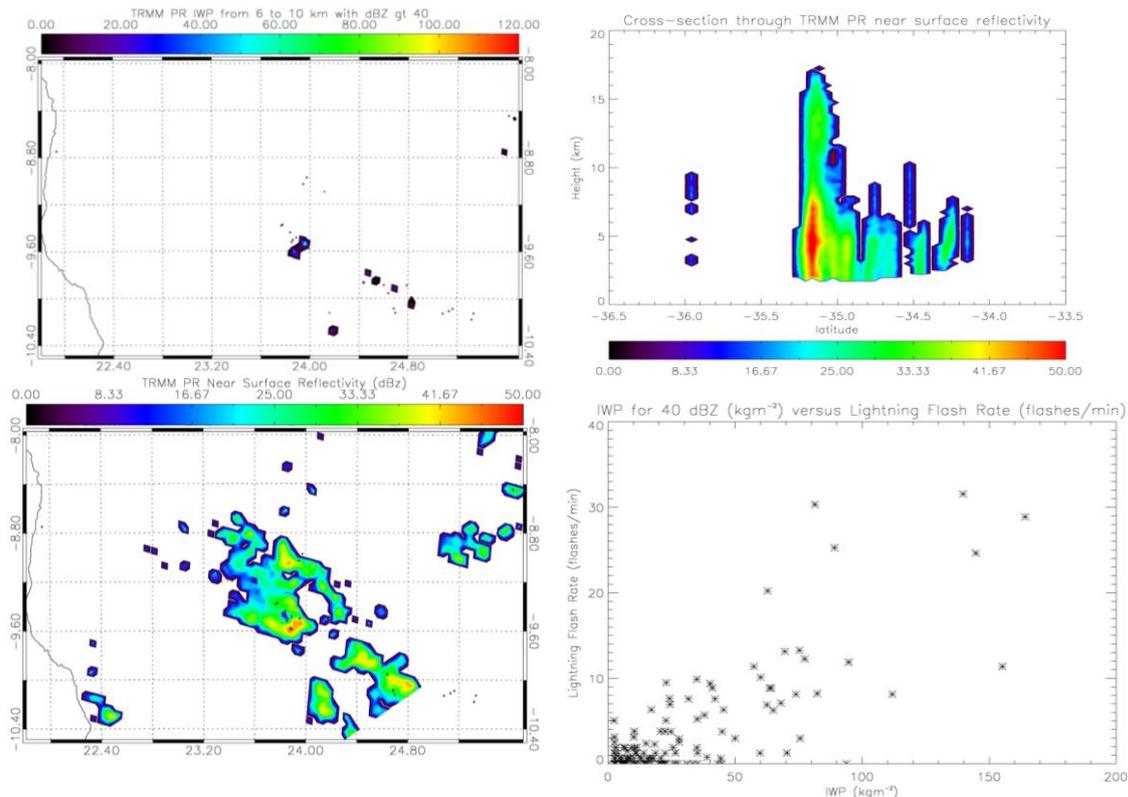

Figure 4.1-1: TRMM fields used to diagnose storm intensity. Results from January 2007 show that there is a correlation between the IWP (ice water path) and lightning flash rate for both ocean and land cases, with a correlation coefficient of ~0.8.

56

4.2 Storm Movement, Intensification/Decay, and Lifetime Estimation

Knowledge of convective storm motion can help one to forecast the future position of a storm as well as to evaluate the possibility of heavy rainfall. The literature suggests that forecasting the movement of large, organized regions of convective activity known as mesoscale convective systems (MCSs, Maddox, 1980; Morel and Senesi, 2002) can be a significant challenge using upper-air analyzes and NWP fields. In a study examining the movement of more than 100 MCSs over the U.S., Merritt and Fritsch (1984) were amongst the first to recognize that while no true "steering level" exists for MCS motion, most systems move approximately parallel to the contours of the 1000-500 hPa thickness. They also noted that the speed of MCS motion was in part modulated by the location of the area of maximum low-level moisture convergence relative to existing convection. However, they also noted that many systems did not move along lines of constant thickness, and that some moved downshear along the contours while others inexplicably moved upshear ("back-built") along them.

Corfidi et al. (1996) extended and generalized Merritt and Fritsch's work, showing that the propagation component of MCS motion in many cases may be estimated by the speed and direction of the 850 hPa low-level jet. This is a rather surprising finding given that storm propagation can be influenced a myriad of other factors such as the distribution of convective available potential energy (CAPE), convective inhibition, gravity waves, outflow boundaries and orographic effects (e.g., Juying and Scofield 1989, Moore et al. 1993). Based on this finding, Corfidi et al. developed a simple procedure for the predicting the short term (6-12 hour) motion of the meso-alpha scale cores of MCSs. In this scheme, MCS core motion is taken to be the vector sum of (1) a vector representing cell advection by the mean cloud-layer wind and (2) a vector representing storm propagation – i.e., new cell development – directed perpendicular to the low-level jet. Because the "vector approach" requires knowledge of only the low-level jet and mean cloud-layer wind, and because the technique may be applied in any type of environmental wind regime (systems are not constrained to follow a given thickness contour), it is ideal for operational use. The vector approach is also of value in identifying those kinematic situations conducive to the development of quasi-stationary and back-building MCSs. The former occur when cell advection is completely offset by cell propagation, while the latter develop when propagation exceeds advection. Both types of systems are frequently associated with excessive rainfall and flash flooding (Chappell 1986).

From a satellite perspective, automated recognition and prediction of cloud motion can be done most effectively by clustering cold cloud pixels into "objects" and tracking these objects within sequential GEO images. To define convective cloud objects, many techniques use a fixed maximum IRW BT value ranging from 225 to 240 K that corresponds with temperature commonly observed in anvil clouds. Some studies also monitor the evolution of intense convective regions featuring extremely cold IRW BTs (< 215 K) within the larger anvil cloud object. Methods may use additional parameters such as the WV-IRW BTD to ensure that an object is indeed a convective cloud and not just a cold cirrus cloud. The first step in deriving object motion involves building an association between objects defined in sequential images. Once objects are matched, motion is computed via determining the displacement of either the centre of the coldest IRW pixels or the geographic centre in the sequential images.

The object-based approach complements traditional satellite-derived wind retrievals, which depict motions over many small target regions in and around the cloud system, but often not for the cloud system as a whole. (Rabin et al., 2004; Bedka and Mecikalski, 2005; Garcia Pereda, 2010). From these sometimes spatially dense wind retrievals, parameters such as divergence and vorticity can be derived in near-real time to augment NWP-based analyses (see section 2.8).

A wealth of literature describes the application of object tracking to IR satellite observations to analyze and nowcast convective storms (Arnaud et al., 1992; Machado et al., 1993; Evans and Shemo, 1996; Hodges and Thorncroft, 1997; Carvalho and Jones, 2001; Honda et al., 2002; Tsakraklides and Evans, 2003; Vila and Machado, 2004; Futyan and Del Genio, 2007; Morel and Senesi, 2002a; Vila et al., 2008; Lakshmanan et al., 2009; Antonelli et al., 2010; Bedka and Minnis, 2010). This reference list would expand to a much greater length if applications with space- and/or ground-based microwave observations were considered. A few techniques are described below.

4.2.1 The NWC-SAF Rapidly Developing Thunderstorm (RDT) Product

The NWC-SAF Rapid Developing Thunderstorm (RDT) product, developed by Meteo-France, is designed to identify, monitor and track intense convective clouds and detect rapidly developing convective cells using geostationary satellite data (Guillou, 2010). It provides information on clouds related to significant convective systems, from meso-α scale (200 to 2000 km) down to smaller scales (a few pixels). The object-oriented approach utilized by the RDT product allows for the derivation of spatially and temporally consistent parameters of interest to the forecaster such as motion vector, cloud-top cooling and areal expansion rate, and cloud top height trends. In the RDT algorithm, "cells" are defined on infrared images (channel IR10.8) by applying a threshold which is specific to each cloud system, and which chosen based on local brightness temperature pattern. An adaptive temperature thresholding of IR data is used and each cloud system is represented by one or several cells defined by its own, cell-specific temperature threshold.

Once the detection of cloud systems is performed, the tracking module of the RDT software is applied on the detected "cells" and allows building trajectories of cloud systems from a sequence of infrared images. The tracking algorithm is based primarily on cell overlap in two successive images. Cells defined in the previous image are moved forward in time according to their previously determined movement, and when a past cell overlaps with one at the current time, the two are considered a match and the object time series is carried forward in time. In the event that no object overlap is found, cross-correlation or nearest neighbour methods are applied. Once a cell is defined and tracked, a discrimination component is used to ensure that the cell is associated with a convective cloud. The discrimination scheme uses following channels for processing predictors: WV6.2, WV7.3, IR8.7, IR10.8, IR12.0. Some of these predictors are optional and different combinations are proposed to the users. Of course, in real-time mode, lightning data can be added to the convective diagnosis. Since the v2011 release, NWP data are used to calculate convection indices and to establish a mask before the RDT processing. After all these steps, the cloud is classified into "early stage", "triggering", "developing", or "mature", based upon a combination of cloud top and the base of cloud tower IR brightness temperatures. The final step removes clouds in the decaying phase and potential false alarms. The use of NWP through various instability indices has been proven to improve accuracy of RDT (Autonès, 2010), see

Figure *4.2-1*.
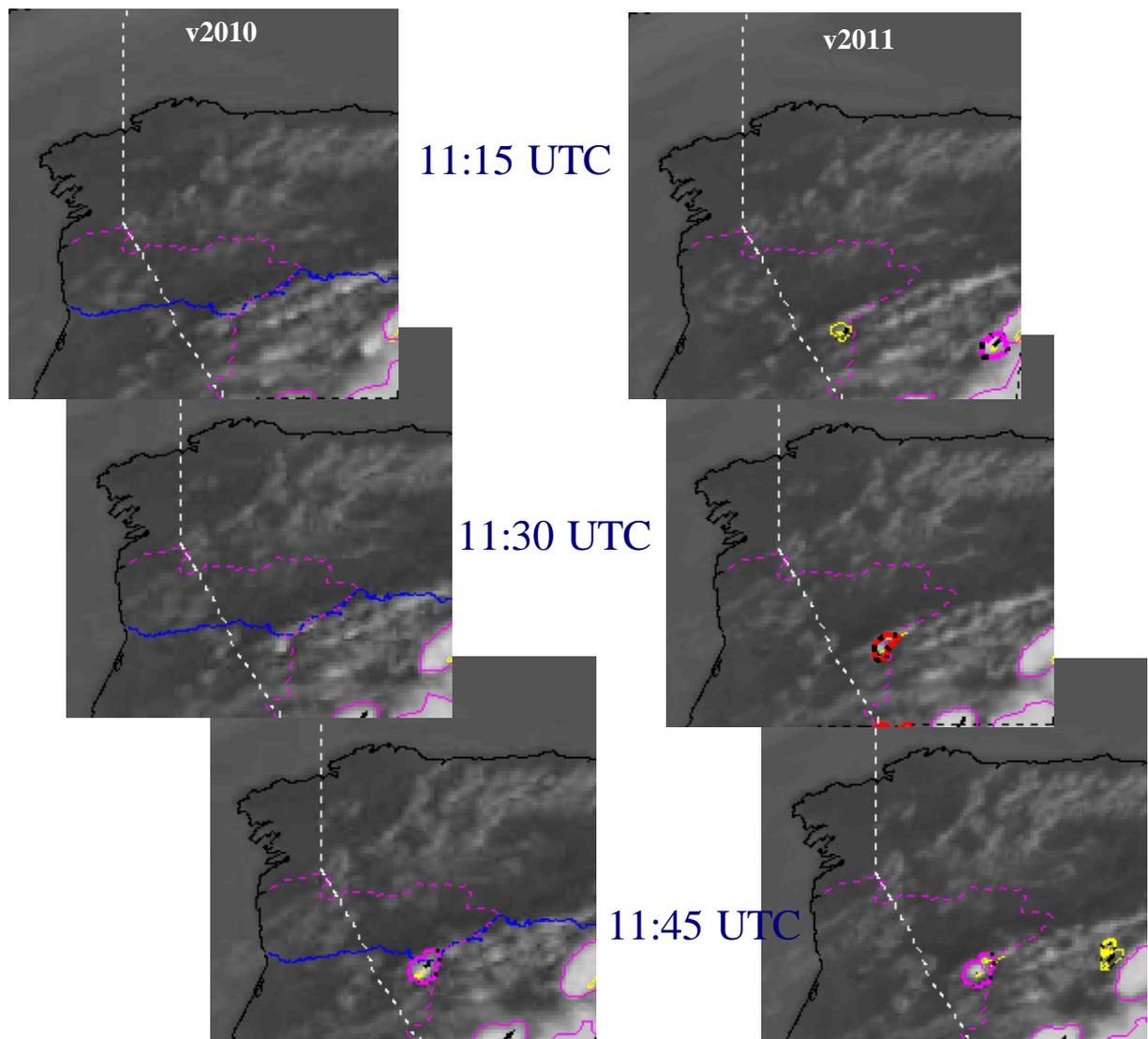
Figure 4.2-1: RDT v2011. NWP Impact on precocity, 20 September 2010. Trajectories, cells and motion vectors from RDT v2010 (left) versus v2011 (right). v2011 uses NWP data as guidance while v2010 does not. v2011 shows an increase of 30 min in precocity for the convective cell near the Portuguese-Spanish border. First detection occurs in the "transition warm" category (yellow line) for v2011, in "mature" category (purple line) for v2010.

4.2.2   The DLR CumulonimBus Tracking and Monitoring (CbTram) Product

The DLR CumulonimBus TRacking And Monitoring (CbTram) algorithm uses SEVIRI HRV,WV6.2, IR10.8 channel brightness temperatures, together with NWP tropopause temperature data to detect convective cells (Zinner et al., 2008). The tracking component of CbTram is based on geographical overlap between current detections and first guess patterns of cells predicted from preceding time steps. The first guess patterns as well as short range forecast extrapolations are obtained with the aid of an image matching algorithm providing complete fields of approximate differential cloud motion. Based on these motion vector fields, interpolation and extrapolation of satellite data are obtained which allow one to generate synthetic intermediate data fields between two known fields as

well as nowcasts of motion and development of detected areas.

4.3 Overshooting Tops

Especially strong convective storm updrafts generated by buoyant energy can penetrate through the stable tropopause region and into the lower stratosphere. These penetrative updrafts have been described in the literature as "hot towers" and/or "overshooting tops" (OT). Thunderstorms with OTs frequently produce hazardous weather at the Earth's surface such as heavy rainfall, damaging winds, large hail, and tornadoes. (Reynolds 1980; Negri and Adler, 1981; Adler et al., 1985; Brunner et al., 2007). Thunderstorms with OTs are also often associated with strong horizontal and vertical wind shear and lightning through a non-inductive graupel-ice collision process within the updraft region (Ziegler and Macgorman ,1994; Wiens et al., 2005), both of which represent serious turbulence and safety hazards for in-flight and ground aviation operations. OTs also generate gravity waves as they interact with and penetrate through the tropopause which can produce turbulence at large distances from the OT region (Heymsfield et al., 1991; Lane et al., 2003; Bedka et al., 2007). Convectively induced turbulence in and around thunderstorms is likely responsible for over 60% of turbulence-related aircraft accidents (e.g., Cornman and Carmichael, 1993; Kaplan et al., 2005; Sharman and Williams, 2009). From United States Federal Aviation Administration (FAA) statistics, Weber et al. (2006) estimate that thunderstorm related flight delays cost the commercial airline industry approximately two billion dollars annually in direct operating expenses.

OTs have been recognized as a significant source of lower stratospheric water vapour. For example, by analyzing aircraft measurements, Dessler (2002) demonstrated that up to 60% of the water vapour crossing the 380 K potential temperature surface at ~17 km was detrained above 15 km. In a later study employing airborne measurements, Corti et al. (2008) showed that ice particles from overshooting tops reached as high as 18.8 km. Gettelman et al. (2002) used satellite data to estimate that overshooting tops cover ~0.5% of the tropics and penetrate up to 1.5 km into the stratosphere. Setvak et al. (2008) employed satellite radiances to show that mid-latitude deep convective clouds also inject some of their water vapour into stratosphere. These and other empirical results are consistent with a variety of modelling studies (e.g., Wang, 2003, Jensen et al., 2007, Chemel et al., 2008) that estimate the moisture balance of the tropical tropopause layer (TTL) and lower stratosphere in the presence of overshooting convection.

The water vapour and ice crystals introduced into the TTL by overshooting convection are thought to be responsible for the thin, often sub-visible, cirrus above 14 km in the tropics (e.g., Wang et al. (1996), Liu (2007)). These clouds, which are characterized as having very small ice crystals (e.g., Wang et al. (1996)), are thought to form from a combination of effects including the direct injection of ice crystals and, more indirectly, convective generated gravity wave pulses clouds above the main convective cloud tops (Garrett et al., 2006). Fujita (1982) described these clouds as "above anvil cirrus plumes" and/or "jumping cirrus". Wang (2007) used a cloud model to show that breaking gravity waves atop a deep convective storm can cause some water vapour to detach from the storm cloud and remain in the stratosphere. This water vapour can condense to form a cloud at levels up to 3 km above the anvil (Levizzani and Setvak, 1996). The above anvil cirrus plumes can extend over 100 km away from the overshooting top (OT) source region (Figure 4.3-1).

Techniques and instrumentation such as numerical modelling, aircraft photography, multi-satellite stereoscopy, active space-based radar, and aircraft-based lidar have been used to better understand the relationship between OT signatures in visible and 11 μm infrared window (IRW) channel satellite imagery and the physical height of the cloud top. From several flights over OTs with an airborne lidar, Heymsfield et al. (1991) showed that some OTs reach altitudes up to 2 km above the surrounding anvil cloud. Through analysis of Tropical Rainfall Measuring Mission (TRMM) Precipitation Radar data (Kummerow and Barnes, 1998), Liu and Zipser (2005) found an overshooting magnitude of 0.67 km for global deep convective clouds. The height difference between lidar and TRMM-based results is likely due to the fact that lidar derives cloud top height via ice crystal reflectance at the physical cloud top whereas TRMM requires reflectance from precipitation particles that reside at lower levels within the cloud. Liu and Zipser (2005) also show that overshooting magnitude depends significantly on whether the level of neutral buoyancy or tropopause height is used as a reference. Currently, MODerate resolution Imaging Spectroradiometer (MODIS) multispectral imagery, CloudSat Cloud Profiling Radar profiles, and Cloud-Aerosol Lidar and Infrared Pathfinder Satellite Observation (CALIPSO) cloud-top height retrievals from the National Aeronautics and Space Administration (NASA) A-Train satellite constellation can be used to better understand the relationship between satellite OT inferences and the physical cloud height (Stephens et al., 2002; Mitrescu et al., 2008; Setvak et al., 2010.

Signatures in multispectral weather satellite imagery indicate the presence of OTs. OTs exhibit a lumpy or "cauliflower" textured appearance in visible channel imagery. OTs are also inferred through the presence of a small cluster of very cold brightness temperatures (BTs) in the IRW region. OTs continue to cool at a rate of 7-9 K km^{-1} as they ascend into the lower stratosphere (Negri, 1982; Adler et al., 1983), making them significantly colder than the surrounding anvil cloud temperature. The surrounding anvil cloud has been shown to have temperatures at or near that of the tropopause level (Adler et al., 1985). This contrasts significantly with a storm with a relatively weak updraft that will feature a relatively uniform cloud top brightness temperature pattern.

Several published studies describe objective OT detection techniques using multispectral satellite imagery. Berendes et al. (2008) show that a combination of visible and near-IR texture and reflectance, IR channel BTs, and multispectral IR channel BT differences (BTD) can be used in an unsupervised cloud classification technique to objectively detect deep convection and OTs (see also section 3.1). While this technique performs well at and around the hours near solar noon, Berendes et al. show a significant diurnal signal in classifier output that can be induced by enhanced texture in visible channel imagery atop deep convective clouds at low solar zenith angles. A close inspection of OT detections during the early morning and evening hours with corresponding visible and IRW channel imagery suggests that many of these pixels would be considered false alarms. Near-IR reflectance and ice particle effective radius techniques (Lindsey and Grasso, 2008; Rosenfeld et al., 2008) suffer from some of the same issues, making these techniques unreliable and/or not applicable for objective day/night OT detection.

The use of infrared-only multispectral band difference techniques for objective OT detection has also been investigated. The 6 to 7 μm water vapour absorption minus the ~11 μm IRW channel BT difference (WV-IRW BTD) technique for OT detection has been described extensively in the literature (Fritz and Laszlo, 1993; Ackerman, 1996; Schmetz et al, 1997; Setvak et al., 2007a-b; Martin et al., 2008). The premise behind the use of the

WV-IRW BTD for OT detection is that: (1) the atmospheric temperature profile warms with height in the lower stratosphere, (2) water vapour is forced into the lower stratosphere at levels above the physical cloud top by the overshooting storm updraft, (3) this water vapour emits at the warmer stratospheric temperature whereas emission in the IR window channel originates from the colder physical cloud top, (4) positive differences between the warmer WV and colder IRW BTs can therefore identify where overshooting is occurring. The maximum WV-IRW BTD can be offset from the OT location due to advection of stratospheric water vapour away from the active thunderstorm updraft (Setvak et al., 2007) or from other remote sources not related to overshooting convection. Via comparison with NASA CloudSat Cloud Profiling Radar observations, positive BTD values generally correspond to deep convective clouds whose tops are located above 14 km, extending into the TTL from 14 km to 19 km, with a cloud depth at least thicker than 4 km, but mostly greater than 10 km (Chung et al., 2008).

The WV-IRW BTD references listed above indicate that the required WV-IRW BTD threshold for OT detection can vary depending upon satellite instrument spatial resolution and spectral channel coverage, intensity of the convective updraft, stratospheric lapse rate, and water vapour residence time in the stratosphere. For 4 km GOES-12 imagery, a BTD value greater than +1 K is shown to relate to the presence of overshooting (Martin et al., 2007). When applied to 1 km MODIS imagery, this BTD value would detect a substantial portion of the anvil in addition to OT pixels, resulting in a large number of false OT detections. (see Figure 4.3-1) A BTD value of +2 K is shown to be a better indicator of overshooting in this higher spatial resolution imagery.
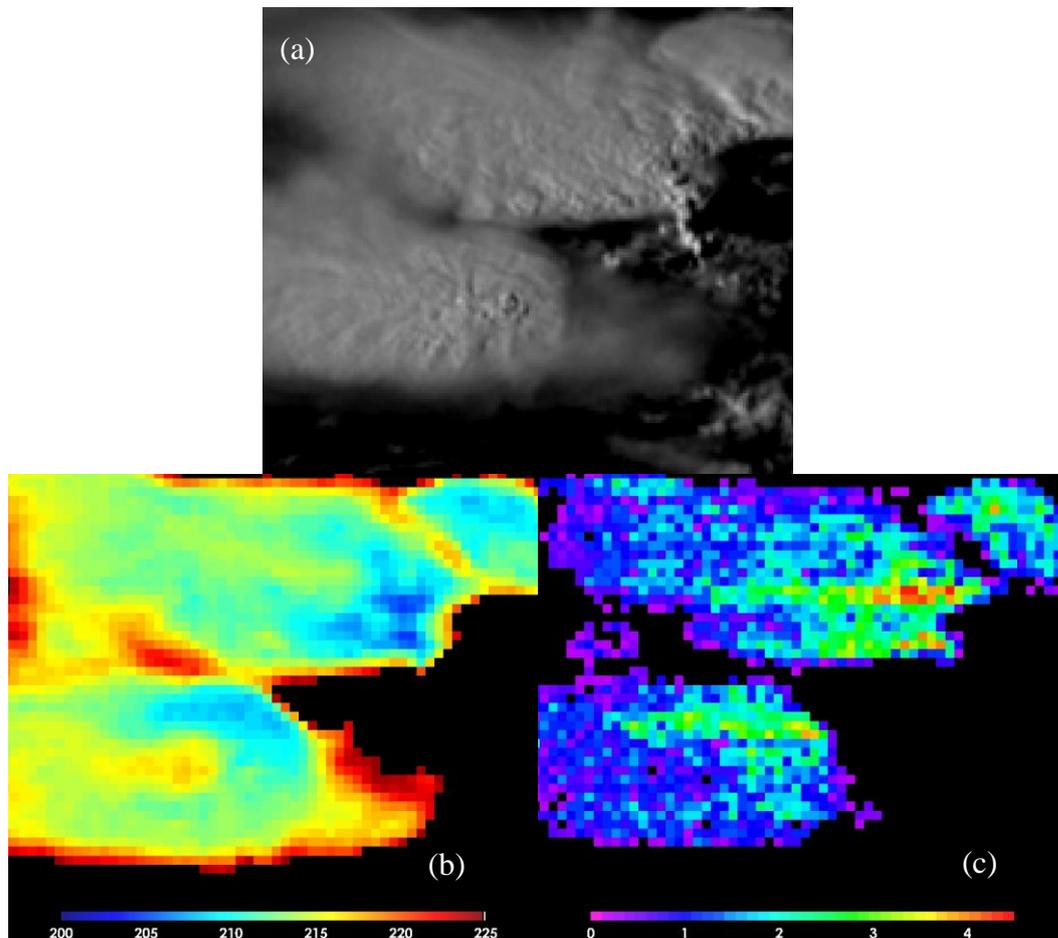
Figure 4.3-1: (a) 1 km MSG SEVIRI HRV,(b) 3 km MSG SEVIRI 10.8 µm brightness temperature, and (c) WV-IRW BTD imagery at 1530 UTC on 25 May 2009. Only IRW BT ≤ 225 K and positive WV-IRW BTD values are shown.

Another detection technique has been developed which utilizes IRW BT minima, spatial gradients in the IRW BT field (i.e. "texture"), and NWP tropopause temperature to detect OTs during both day and night in geostationary and polar-orbiting satellite data (Bedka et al. 2010). This so-called "IRW-texture" method has been used to produce multi-year OT climatologies over the U.S. and Europe, as well as comparisons with aviation turbulence, cloud-to-ground lightning, severe weather reports, and ground-based radar reflectivity (Bedka et al., 2010; Bedka, 2010; Dworak et al., 2011). Figure 4.3-2 shows a comparison between IRW-texture and WV-IRW BTD output for a cluster of deep convective storms along the border between Austria and Slovenia. The IRW-texture method identifies several OT signatures evident in visible channel imagery. The WV-IRW BTD method also flags these regions, but many anvil cirrus pixels are also identified. A six warm season SEVIRI OT database showed a strong relationship with relative OT maxima and regions of high terrain. OTs were found to occur more frequently during the day over land than during the night and over water, similar to the results of Bedka et al. (2010) for the U.S. The number of daytime detections peaks sharply at 1500 UTC near the time of maximum land surface temperature and greatest atmospheric instability. A bi-modal distribution of OTs is evident, with a broad maximum from 1100 to 2200 UTC and a secondary maximum from 0400 to 0700 UTC. Maximum OT occurrence is in May and June over continental Europe, and in September over the Mediterranean Sea. There were also interesting intra-seasonal shifts in OT detections coincident with changes in the favoured climatological locations for storm development throughout the warm season. See Bedka (2011) for a full description of these results. Figure 4.3-3 shows gridded OT results over Europe, April-September for years 2004-2009.

The appearance and apparent time evolution of an overshooting top is affected by the spatial and temporal resolution of satellite imagers. Analysis of animated GOES super rapid scan visible channel imagery indicates that an OT can form and dissipate several times within the 15-minute scan frequency utilized by many currently operational imaging instruments (see the following for animated 1-minute resolution GOES-15 imagery: http://cimss.ssec.wisc.edu/goes/blog/wp-content/uploads/2010/09/100921_g15_srso_vis_overshoots_anim.gif). This is caused by pulsing within the primary storm updraft. Updraft intensification will produce a new tropopause penetration that will later collapse when the updraft weakens. Thus, there is no guarantee that an OT present in one scan will be the same feature as another observed in the following 15-minute scan. Brunner et al. (2007) shows that the minimum IRW BT within an OT increases by 11 K if 1 km resolution data are degraded to an 8 km resolution, making objective OT detection more challenging as resolution coarsens. Adler et al. (1986) and Setvak et al. (2010) also suggest that an overshooting top can warm over time as the OT mixes with the stratospheric environment.
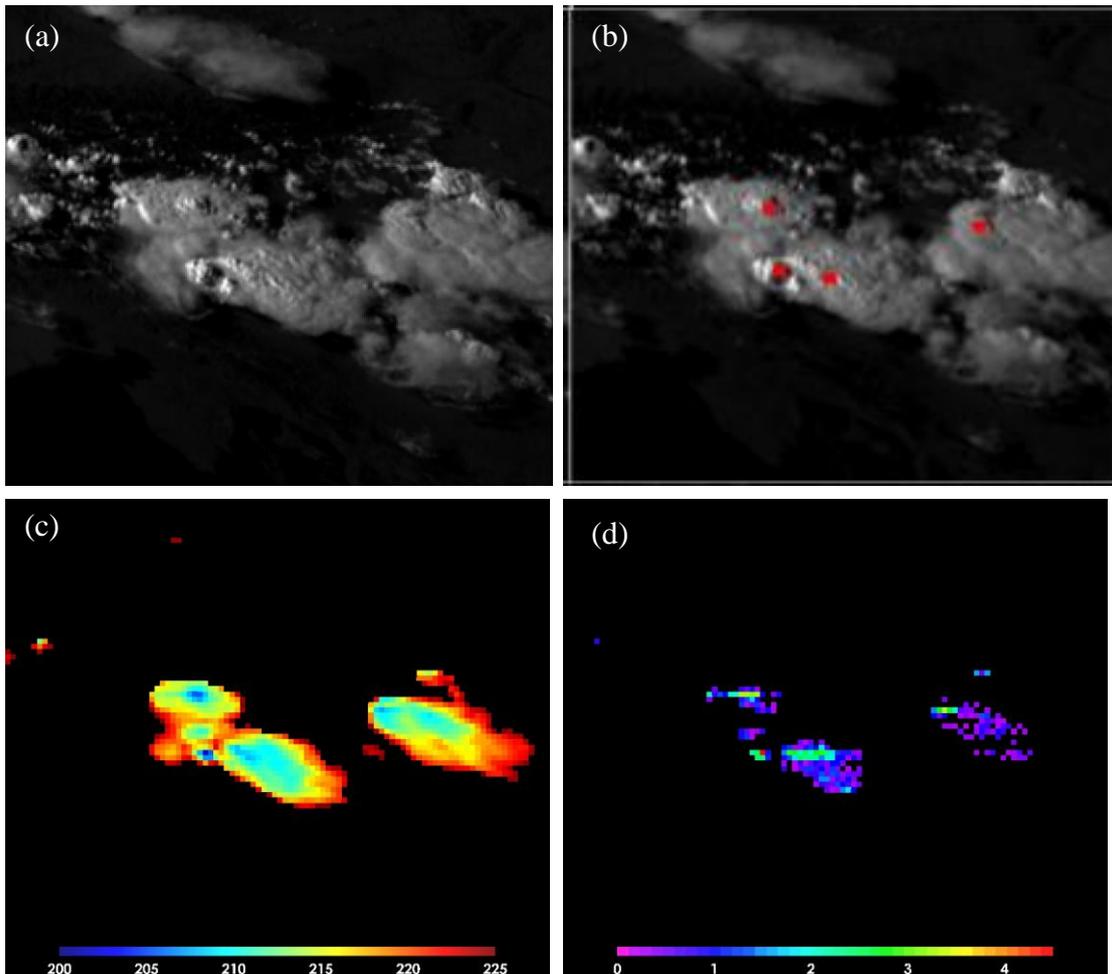
Figure 4.3-2: (a) 1 km MSG SEVIRI HRV, (b) 3 km MSG SEVIRI 10.8 µm brightness temperature, (c) HRV with IRW-texture objective overshooting top detections, and (d) WV-IRW BTD imagery for deep convective storms along the border between Austria and Slovenia at 1600 UTC on 25 May 2009. Only IRW BT ≤ 225 K and positive WV-IRW BTD values are shown.
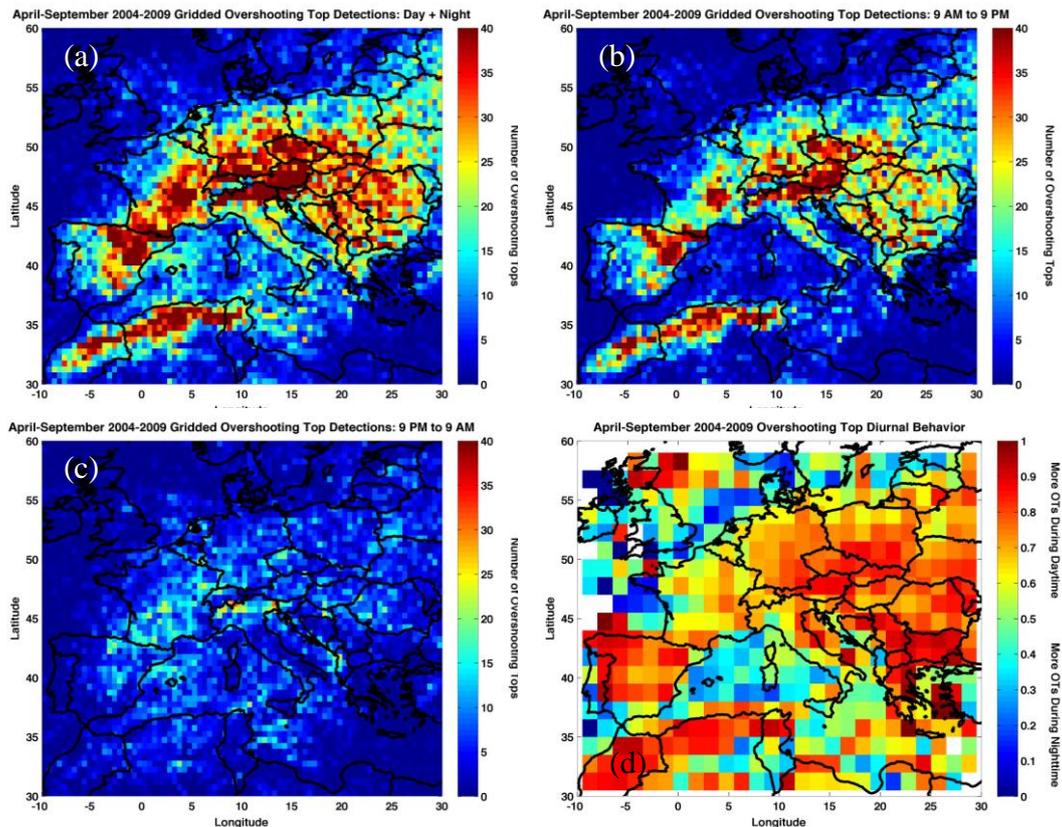
Figure 4.3-3: IRW-texture overshooting top detections on a 0.50° grid. (a) All overshooting top detections, (b) daytime only (0900 AM to 0859 PM LT), (c) night-time only (0900 PM to 0859 AM LT), and (d) the fraction of overshooting top detections occurring during the daytime. This fraction is computed over 1.5° x 1.5° grid boxes such that a significant OT sample size is used to determine this statistic. Warm (Cool) colours in panel d) indicate that more tops were detected during the day (night). Only locations with 5 or more OTs in a 1.5° grid box are shown.

Though qualitative and/or case study based analysis indicate that a storm with an OT is hazardous, it is important to quantify these hazards to demonstrate that objective OT detection provides additional value relative to existing datasets and forecasting techniques. Confirmed severe wind, large hail, and tornado events from the ESWD were compared to OT detections to determine how often OTs are detected near the time and location of confirmed severe weather reports. An OT was found in the vicinity of severe weather events for 643 or ~44% of the 1475 confirmed reports from the 2004-2009 warm seasons (April to September). The relationship is strong for large hail (53%) and severe wind (52%) events but relatively weak for tornadoes (14%). OT detections were also compared with severe weather reports over the U.S. for the same time period (Dworak et al., 2011). This study included a much larger sample size of 113,541 severe weather reports. The results were comparable for large hail (51%) and severe wind events (58%), but vastly different for tornadoes (56%). Strong atmospheric instability (i.e. CAPE) is necessary to produce the intense updrafts required for OTs, but also large hail formation. Earlier studies had shown that large low-level wind shear values are found more often than high CAPE in tornadic thunderstorm environments across Europe. (Sander et al., 2008; Brooks, 2009; and Kaltenböck et al., 2009). Bedka (2011) suggests that weaker updrafts in tornadic storms

relative to storms that produce severe hail/winds result in a less prominent or possibly non-existent OT signature in IRW BT imagery.

The relationships between satellite OT signatures, ground-based weather reflectivity, and derived radar products over the U.S. have been examined in detail by Dworak et al. (2011). Figure 4.3-4 shows a time sequence of GOES-12 rapid scan imagery and time-matched WSR-88D data while an EF-5 tornado was on the ground in Parkersburg, IA. Despite the relatively coarse GOES-12 spatial resolution (~5 km over Iowa), OTs are detected where distinct minima in the IRW BT field are present. The maximum composite radar reflectivity and highest precipitation echo tops within the domain were co-located with the OT detections. Figure 4.3-5 shows that the echo top rapidly increased prior to the first OT detection within this storm and the tops remained above 52 kft as OTs were consistently detected over the 40 min period while the tornado was on the ground. Through analysis of 207 individual storm cells, Figure 4.3-6 shows that radar reflectivity aloft was maximized shortly before or at the time of OT presence. The reflectivity maximizes near the surface and echo top lowers soon after detection as the storm updraft pulses, a typical behaviour that is readily apparent in 1-min Super Rapid Scan data (see http://cimss.ssec.wisc.edu/goes/blog/wpcontent/uploads/2010/09/100921__g15_srso_vis_overshoots_anim.gif for an example).
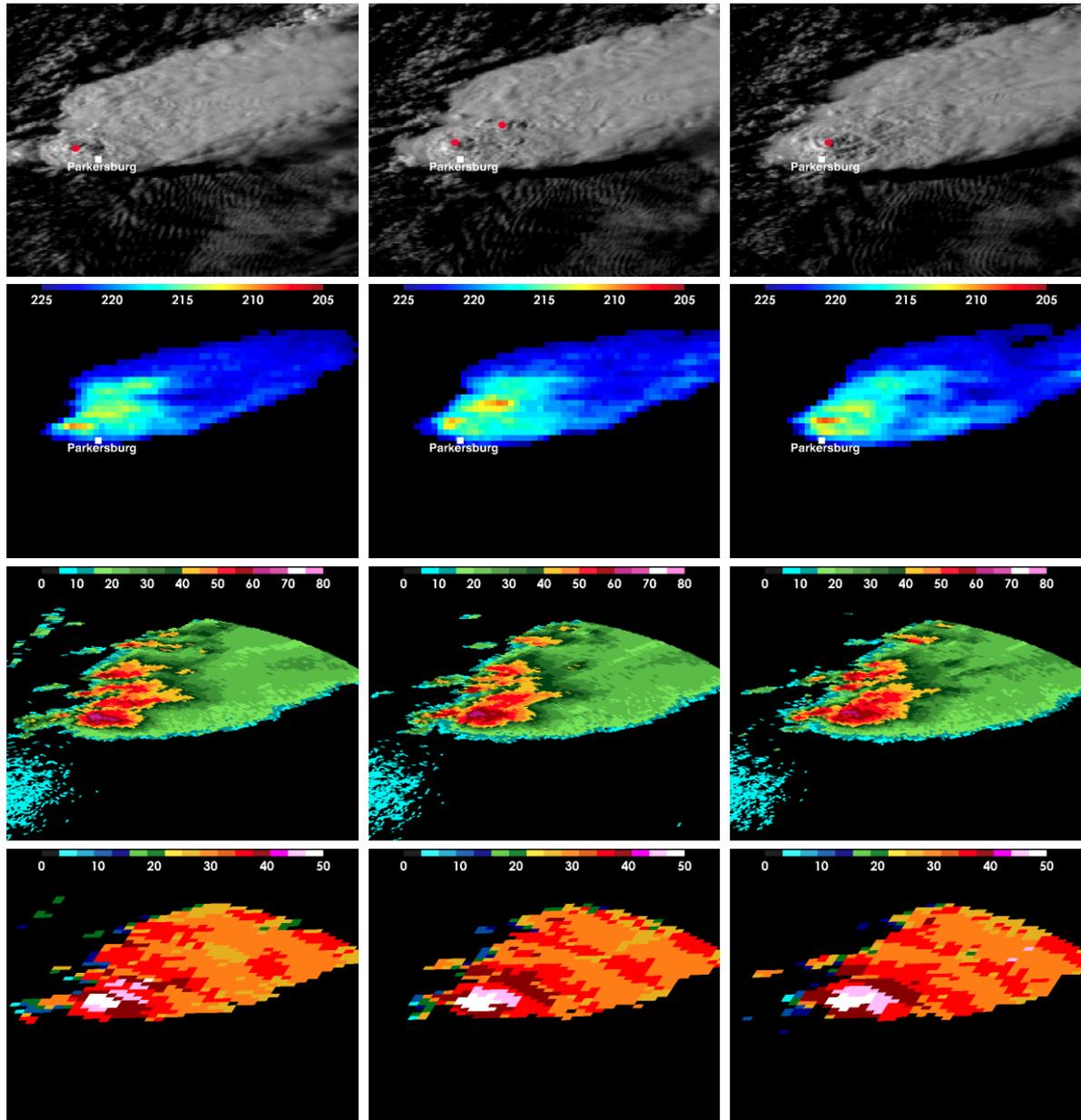
Figure 4.3-4: (top row) GOES-12 visible channel imagery with objective OT detections (red dots),(second row) GOES-12 IRW imagery, (third row) KDMX (Des Moines, IA) WSR-88D composite reflectivity, and (fourth row) KDMX WSR-88D echo top product at 2145 (left column), 2155 (middle column), and 2202 UTC (right column) on 25 May 2008 for a tornadic OT-producing storm near Parkersburg, IA (city location labelled on the GOES imagery). From Dworak et al., 2011.
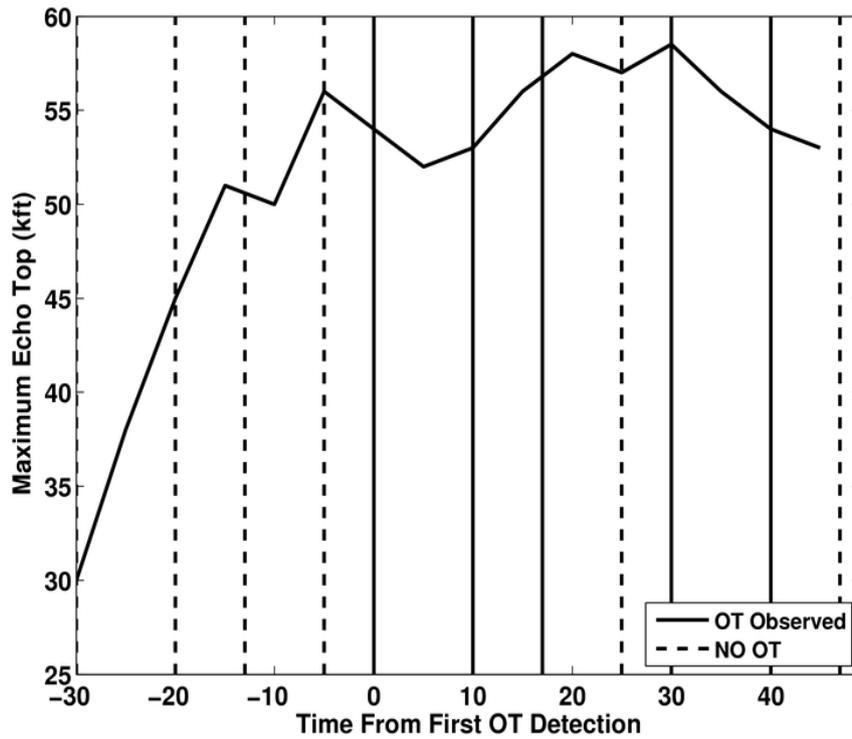
Figure 4.3-5: The co-evolution of GOES-12 OT detections and WSR-88D echo top for the Parkersburg, IA tornadic storm event shown in Fig. 24. From Dworak et al. (2011).
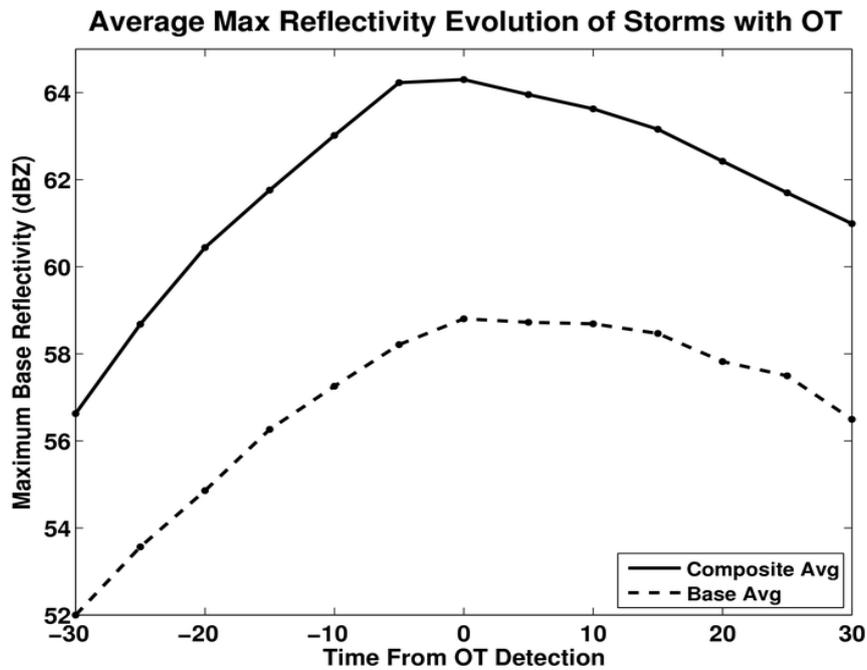
Figure 4.3-6: The time evolution of mean base and composite reflectivity within +/- 30 mins of the 207 confirmed OT detections.

OTs identified within GOES-12 imagery have been shown by Bedka et al. (2010) and Machado et al. (2009) to represent a significant cloud-to-ground lightning hazard. When IRW-texture OT pixels are directly compared with nearby U.S. National Lightning Detection Network (NLDN) observations, CG lightning is found to occur within a 10 km radius of an OT ~30% more often than a non-overshooting cold cloud pixel (see Figure 4.3-7). For very cold OTs with IRW BTs less than 200 K, CG lightning occurred nearby for 70% of all OT occurrences. Machado et al. (2009) found that WV-IRW BTD values greater than −15 K are associated with penetrative clouds with potential for cloud-to-ground discharge activity in a study over Brazil. As the BTD increases, the probability of lightning increases. These differences are also associated with the probability to have a specific number of cloud-to-ground discharges per pixel. For instance, if the BTD=0, the probability of having at least one cloud-to-ground discharge is 10.9%, 7.0% for two, 4.4% for four, 2.7% for eight and 1.5% for sixteen cloud-to-ground discharges. Figure 3.3.8 suggests that the probability of cloud-to-ground discharge can be expressed as an exponential function of the WV-IR BTD.
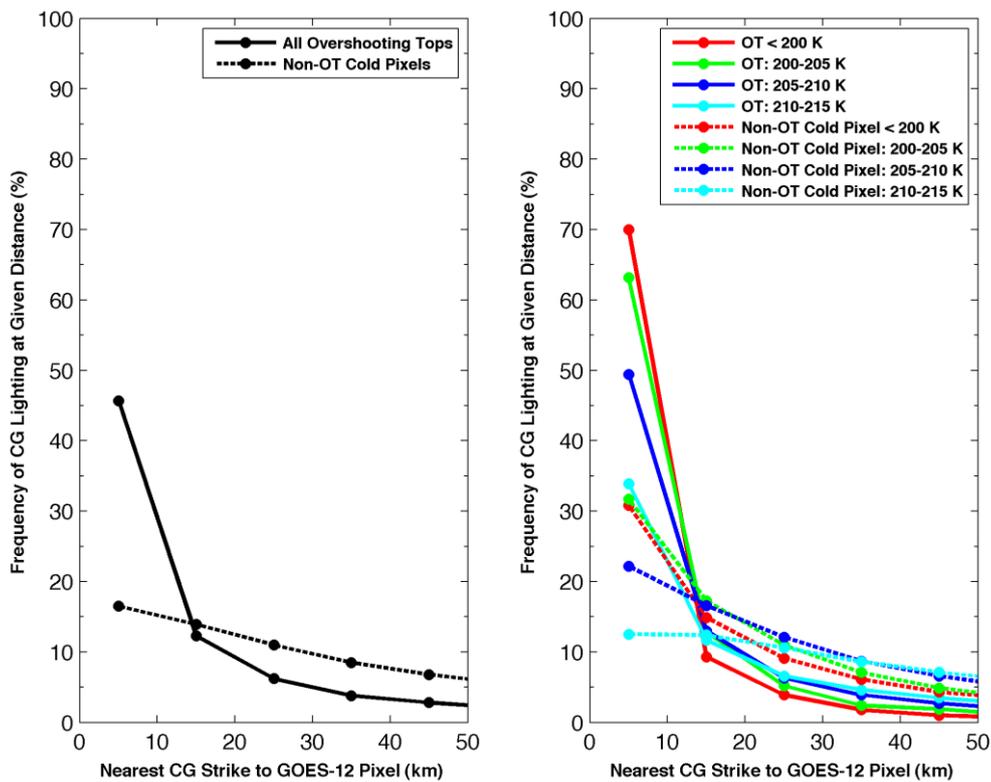

Figure 4.3-7: The distance between both GOES-12 IRW-texture OT detections and non-overshooting cold pixels to the closest cloud-to-ground lightning strike from May to September 2008. (right) A similar comparison to the left panel, but overshooting and non-overshooting pixels are grouped into IRW BT bins. From Bedka et al., 2010.
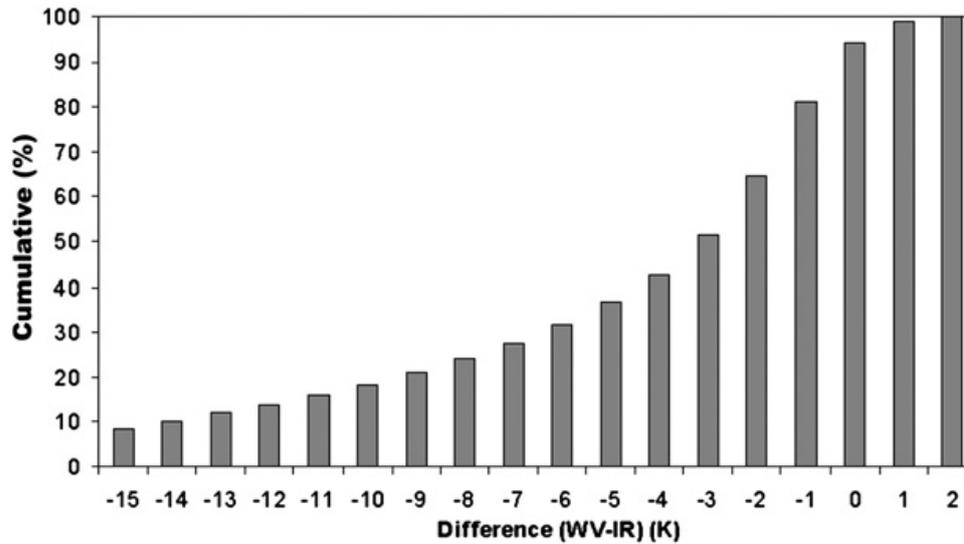
Figure 4.3-8: Cumulative frequency (%) of cloud-to-ground discharge occurrence as a function of the WV-IR brightness temperature (K). From Machado et al., 2009.

OTs are also a significant in-flight turbulence hazard. Bedka et al. (2010) show that aircraft which flew within 5 km of an OT experienced turbulence in 42% of all encounters, a 50% increase in turbulence frequency relative to flights near non-overshooting cloud pixels (BT < 215 K with a uniform cloud-top BT pattern, see Figure 4.3-9). Moderate or greater turbulence occurs 58% more often than non-OT cold pixels at a 5 km radius from an OT and 9.5% of flights within 0-5 km of an overshoot experienced moderate or greater turbulence. Severe turbulence is quite infrequent, ~1.25% of all flights observed within a 0-5 km radius from an OT experienced severe turbulence, but this turbulence was observed 12.5 times more frequently near an OT than a non-overshooting cold pixel.
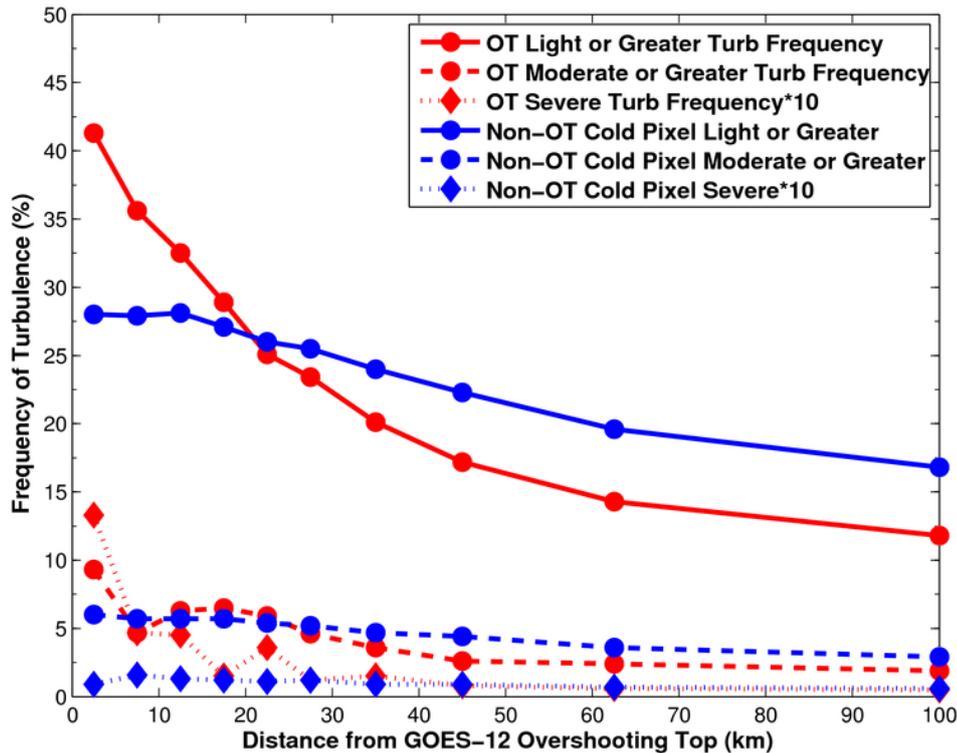
Figure 4.3-9: The frequency of turbulence inferred through United Airlines objective in-situ Eddy Dissipation Rate observations at varying distance from GOES-12 OT and non-overshooting cold pixels (non-OT) from April-September 2005-2008 over the U.S. The frequency of severe turbulence is multiplied by 10 so that variability in the curves can be seen using the y-axis scale appropriate for lesser intensity turbulence. From Bedka et al., 2010.

4.4 Cold-U/V and Cold-Ring Signatures

Overshooting tops are also a key component of two inter-related severe storm signatures in IRW imagery called the "cold- or enhanced-U/V" and "cold ring". An enhanced-V signature is composed of the following in IRW satellite imagery:

1) An OT which is well correlated with the coldest pixels in a given thunderstorm cloud top and acts to divert the upper level flow around it.
2) A U- or V-shaped pattern of relatively cold BTs with the apex of the U or V signature located slightly upwind of the OT. The "arms" of this signature extend downwind of the OT, often along the periphery of cirrus anvil cloud.
3) A region of anomalously warm BTs located downwind of the OT region. The combination of the cold OT and downstream warm region is called the anvil thermal couplet (ATC).

Setvak et al. (2010) provide an excellent summary of the previous research on and the characteristics of cold-U/V and ring shaped storms. The following discussion is an excerpt from this paper.

In the early 1980's, Negri (1982), Fujita (1982), McCann (1983), Heymsfield et al. (1983a) and several others documented storms exhibiting a feature they called an enhanced-V. The original name of this feature reflects the fact that it was revealed in enhanced IR imagery. A more physically descriptive term of this signature is cold-U (or cold-V, depending on the

actual appearance of the feature, or generally cold-U/V) shape. Follow-up works, including Heymsfield et al. (1983b), Schlesinger (1984, 1988), Adler et al. (1985), Adler and Mack (1986), Heymsfield and Blackmer (1988), and Heymsfield et al. (1991) discussed the origins of this feature and namely of the warm regions enclosed by this feature, the close-in warm area (CWA) and the distant warm area (DWA). Negri (1982) and Heymsfield et al. (1983) hypothesize that the downstream warm area is produced through adiabatic descent (or subsidence) downwind of the OT updraft location. Others such as Setvak et al. (2007) suggest that moisture ejected into the stratosphere produces an "above anvil cirrus plume" downstream of the OT, which radiates at a warmer temperature than the primary anvil cloud underneath, contributing to the CWA and DWA. McCann (1983) and Brunner et al. (2007) describe the relationship of storms exhibiting the cold-U/V signature with severe weather, namely strong winds, large hail, and tornadoes. Brunner et al. shows that a cold-U/V producing storm with a large OT-CWA BT difference is a strong indicator that the parent thunderstorm is severe.

Storms exhibiting cold rings or cold-U/V shapes belong to a category of storms whose tops exhibit some form of cold/warm couplets. Bedka et al. (2010) use the term "anvil thermal couplet" (ATC) to describe the temperature contrast between the OT and CWA. Under favourable conditions almost every major overshooting top generates a downwind counterpart, a warm spot of varying horizontal extent, BT difference from the surrounding anvil, and duration. Warm spots embedded within cold anvil tops were first reported some 30 years ago, on the basis of GOES/SMS imagery (Mills and Astling, 1977). Typically, based on SEVIRI, these are only transient features, disappearing shortly after the collapse of their "parent" overshooting top.

In general, storms exhibiting some form of embedded warm area or short-lived smaller-scale warm spots, forming downwind of the individual overshooting tops, are quite common in MSG imagery over Europe (see Figure 4.3-3). It seems that their occurrence is supported by some specific airmass types and wind shear; on some days they tend to form at cloud top of almost every storm over larger regions, while on other days all the storms have a "regular" appearance, without any trace of a warm spot. Most of the overshooting top-warm spot couplets have lifetimes of typically up to 2 or 3 MSG 15-minute scan cycles; however, some of them can be found in a single 5-minute rapid scan only. There are several cases of long-lived (of the order between 1 to 2 h) and large-sized cold-ring-shaped storms documented over the last few years. The majority of these produced some form of severe weather (Image Gallery at http://www.eumetsat.int/).

Cold-ring shaped storms are similar to those with a cold- U/V shape, differing only by the closed shape of the cold feature (see Figure 4.4-1, bottom). The cold ring entirely encloses the central warm spot (CWS). The typical CWS size is from several SEVIRI pixels up to about 50 km. The temperature difference between the cold ring minimum and CWS maximum is typically from several degrees up to about 10–12 K. However, since this temperature difference strongly depends on the temperature minimum of the "parent" overshooting tops, which form and disappear at periods ranging from several minutes up to 20–30 min, this characteristic depends on the actual state of the overshooting top when scanned by a satellite. It should be noted that the BT minimum of an overshooting top also depends on the satellite resolution (pixel size): the BT difference between the BT minimum and CWS maximum can reach higher values for instruments with better pixel resolution (e.g. those found aboard polar orbiting satellites), as compared to geostationary satellite observations (e.g. Setvák and Levizzani, 1992; Bedka et al., 2010). For geostationary

observations, this BT difference will reach higher values for instruments or missions with higher scanning frequency. For most of Europe, cold-ring-shaped storms seem to be significantly more frequent than cold-U/V-shaped ones.

The typical CWS size is from several SEVIRI pixels up to about 50 km. The temperature difference between the cold ring minimum and CWS maximum is typically from several degrees up to about 10–12 K. However, since this temperature difference strongly depends on the temperature minimum of the "parent" overshooting tops, which form and disappear at periods ranging from several minutes up to 20–30 min, this characteristic depends on the actual state of the overshooting top when scanned by a satellite. It should be noted that the BT minimum of an overshooting top also depends on the satellite resolution (pixel size): the BT difference between the BT minimum and CWS maximum can reach higher values for instruments with better pixel resolution (e.g. those found aboard polar orbiting satellites), as compared to geostationary satellite observations (e.g. Setvák and Levizzani, 1992; Bedka et al., 2010). For geostationary observations, this BT difference will reach higher values for instruments with higher scanning frequency.
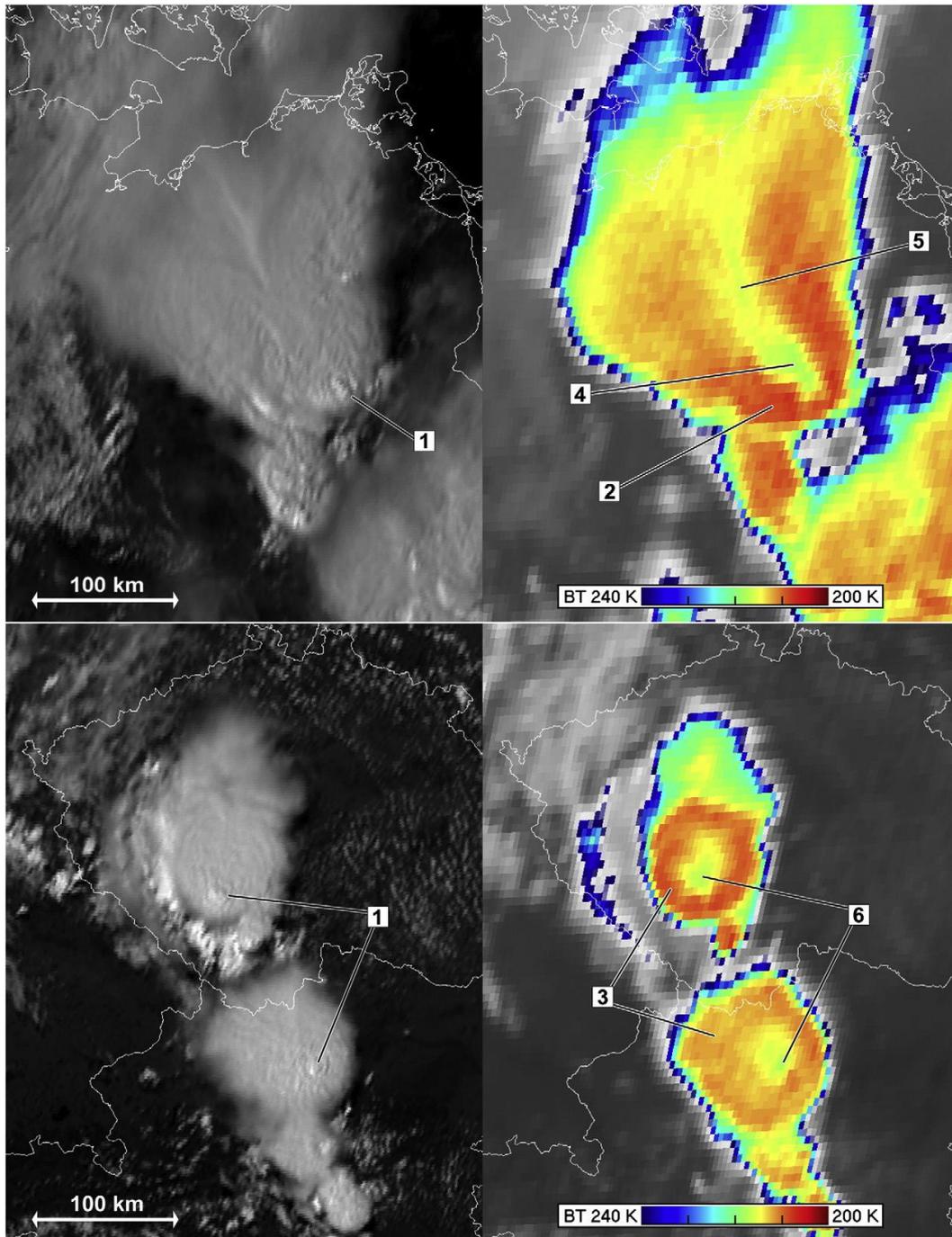
Figure 4.4-1: Examples of cold-U shaped storms–top (Meteosat-9, 26 May 2007, 15:00 UTC, Germany) and cold-ring shaped storms–bottom (Meteosat-8, 25 June 2006,13:45 UTC, Czech Republic and Austria). Left: high-resolution visible (HRV) images, right: colour enhanced IR10.8 images. Legend: 1–overshooting tops, 2–cold-U shape, 3–cold ring shapes, 4–close-in warm area (CWA), 5–distant warm area (DWA), 6–central warm spots (CWS). Time in this figure refer to the beginning of the scan of the image slot.

4.5   Objective Cold U-V Signature Detection

Brunner et al. (2007) show that the cold-U/V signature appears somewhat differently in almost every case, making direct pattern recognition of this feature very challenging (see Figure 4.5-1). In addition, as spatial resolution decreases, the V pattern becomes poorly defined in IRW imagery. A new objective detection method focuses on detection of the OT and CWS rather than direct pattern recognition of the V signature, as this is considered to be an approach that is less prone to false detections. The OT and CWS are found very near to each other and can be considered an "anvil thermal couplet" (ATC). This ATC method has been developed in support of the GOES-R ABI program, but is also applicable to current GEO and LEO imagery (Bedka et al., 2010).

The first step of ATC detection uses the IRW-texture method to find all OTs within an image. Next, an NWP 250 hPa wind analysis is used to define a search region where the CWA is expected to be found. Analysis of a large sample of enhanced-V events indicates that most CWA are within 35 km from the OT region. Candidate CWAs are identified within a region +/- 45 deg of the 250 hPa wind direction and within 35 km of the OT. The OT minimum IRW BT must be at least 10 K colder than the candidate CWA mean BT over a 3x3 pixel region centered on the CWA. The maximum CWA IRW BT also must be $\leq$ 225 K. Spatial checks are performed for these candidate CWAs to ensure that they represent a focused area of warm BTs surrounded by colder anvil cloud and are not along the edge of the anvil where small regions of anomalously warm BTs are often present that can trigger false ATC detections via this methodololgy.

Bedka et al. (2010) subjectively examined ATC detection performance relative to 415 (of the 450 total) cold-U/V events identified in AVHRR and MODIS imagery by Brunner et al. (2007). These 415 events were scatted across 136 individual AVHRR or MODIS granules over the continental U.S. The algorithm is shown to have a POD of ~53% and a FAR of 20%. Detailed analysis shows that the primary source of non-detections is lack of detection of the OT region, not inadequacies in the CWA detection logic. Regions of warm BTs between adjacent thunderstorm anvils are the primary source of false detections. ATC detections were compared with NOAA Storm Prediction Center severe storm reports that occurred within +/- 30 mins and 60 km of the 415 cold-U/V events. 76% of storms with detected ATCs produced severe weather. 62% of the undetected cold-U/V ATC storms produced severe weather, indicating that storms with detectable and pronounced CWAs are more often severe.
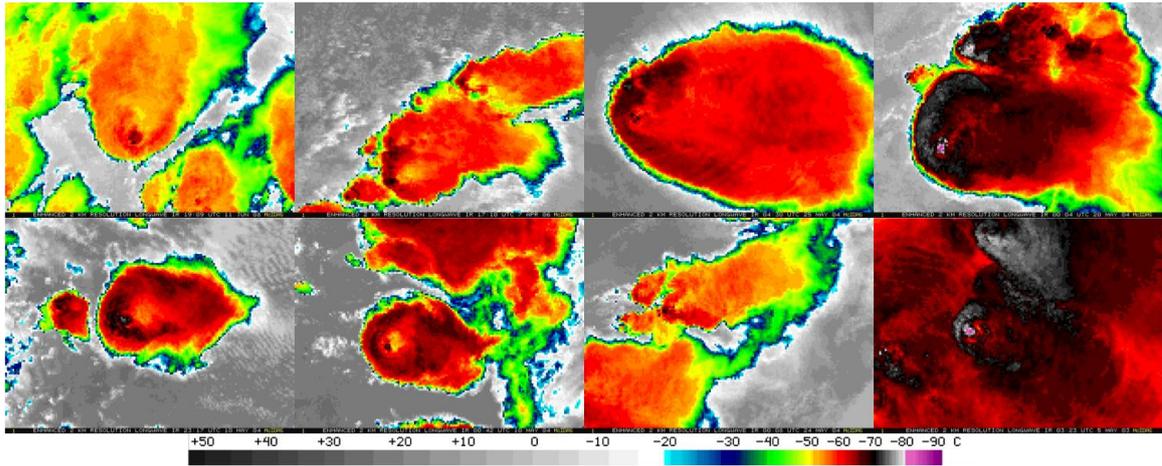
Figure 4.5-1: MODIS and AVHRR ~11 µm IR window imagery for 8 enhanced-V events. All images cover the same horizontal distance and use same colour enhancement, illustrating the significant variations in the V-signature across events.

4.6 Convective Cloud Top Height

Objective assessment of convective cloud top height is important for aviation interests. Current U.S. Federal Aviation Administration (FAA) guidelines in the Aeronautical Information Manual (2010, available online at: http://www.faa.gov/air_traffic/publications/atupubs/aim/) suggest that aircraft avoid severe thunderstorms by at least 20 miles, including under anvil regions and above thunderstorm tops. Since much of the convective anvil cloud is optically thick with a near-unity emissivity, the IRW BT of a convective cloud pixel can be compared with a NWP model temperature profile to derive a cloud height. This method has proven to be quite accurate for an opaque anvil cirrus cloud when a reasonably accurate model profile of sufficiently high vertical resolution is used in this process. One must understand that even an optically thick cloud emits radiation at a height within the cloud, not at the physical cloud top that would be depicted by a lidar instrument.

Several studies have examined the accuracy of cloud top height retrievals for optically thick clouds. Smith et al. (2008) compared 5 years of surface-based cloud radar and lidar data taken at the Atmospheric Radiation Measurement (ARM) program's site near Lamont, Oklahoma with the three versions of the NASA Langley Research Center's GOES Imager cloud top height product. They found that for high clouds ($\geq$ 7 km in height) with an optical depth $\geq$ 6, the clouds were assigned 0.4 to 1.1 km too low and had a root-mean-squared error ranging from 0.8 to 1.6 km. Daloze and Haefflin (2005) found that the NWCSAF cloud top heights were 0.4 km too low based on a similar ground based product based on a combination of cloud radar and lidar observations over the Site Instrumental de Recherche par Télédétection Atmosphérique (SIRTA) in Palaiseau, France. For RDT Cloud Top Temperature and Height are issued from Cloud PGE of SAF/NWC. An empirical rule converts the information available for the numerous pixels of one cell into a single attribute.

Cloud top height assignment for OT pixels remains a challenge though because IRW BTs in the OT region are often significantly colder than any temperature in the model profile. Many height assignment algorithms default by assigning these very cold OT pixels to the tropopause height. Stastka and Setvak (2008) show that the NWCSAF cloud top height

product significantly underestimated the height of an OT relative to a ground-based radar height estimate. To remedy this, a method is being implemented within CERES cloud properties algorithm package (Minnis et al., 2010) that uses the Bedka et al (2010) IRW-texture OT detection method in combination with an assumed temperature lapse rate to elevate the height of detected OT pixels. Innovative approaches such as this one must be developed to address the challenges of OT height assignment.

4.7 Cloud Top Microphysics and Inferred Processes in Mature Storms

Rosenfeld et al. (2008) presents a new conceptual model that facilitates the detection of the vigour of convective storms by remote sensing from satellites, based on the retrieved vertical profiles of cloud-particle effective radius and thermodynamic phase. A major driving force of all these severe weather phenomena is the high updraft speeds, which can sustain the growth of large hailstones, provide the upward motion that is necessary for evacuating vertically the violently converging air of a tornado, or complemented strong downward motion, which results in downbursts and intense gust fronts. Wind shear provides additional energy for sustaining the dynamics of tornadic supercell storms and squall lines that can recirculate large hailstones and produce damaging winds.

The conceptual model of a satellite-observed severe storm microphysical signature is based on the satellite-retrieved microphysical signature of the updraft velocity on the developing convective elements that have the potential to become severe convective storms, or already constitute the feeders of such storms. The severe storm microphysical signature, as manifested by the vertical profile of cloud-particle effective radius, is caused by the greater updrafts delaying to greater heights the conversion of cloud drops to hydrometeors and the glaciation of the cloud. The greater wind shear tilts the convective towers of the pre-storm and feeder clouds and often deflects the strongly diverging cloud tops from obscuring the feeders. This allows the satellite a better view of the microphysical response of the clouds to the strong updrafts. This satellite severe storm signature appears to primarily reflect the updraft speed of the growing clouds, which is normally associated with the CAPE. However, wind shear is as important as CAPE for the occurrence of severe convective storms, in addition to helicity that is an important ingredient in intense tornadoes. It is suggested that the effectiveness of the satellite retrieved severe storm signature and inferred updraft speed may not only depend on the magnitude of the CAPE, but also on the wind shear, and perhaps also on the helicity. This can occur when some of the horizontal momentum is converted to vertical momentum in a highly sheared environment when strong inflows are diverted upward, as often happens in such storms. While this study focuses on exploring a new concept of satellite application, eventually a combined satellite with sounding algorithm is expected to provide the best skill.

The vertical evolution of cloud top particle size can be retrieved readily from satellites, using the methodology of Rosenfeld and Lensky (1998) to relate the retrieved effective radius (r_e) to the temperature (T) of the tops of convective clouds (see Figure 4.7-1). An r_e >14 mm indicates precipitating clouds (Rosenfeld and Gutman, 1994). The maximum detectable indicated r_e is 35 mm, because of saturation of the signal. The T-r_e relations are obtained from ensembles of clouds having tops covering a large range of T. This methodology assumes that the T-r_e relations obtained from a snap shot of clouds at various stages of their development equals the T-r_e evolution of the top of an individual cloud as it grows vertically. This assumption was validated by actually tracking such individual cloud elements with a rapid scanning geostationary satellite and comparing with the ensemble

cloud properties (Lensky and Rosenfeld, 2006).
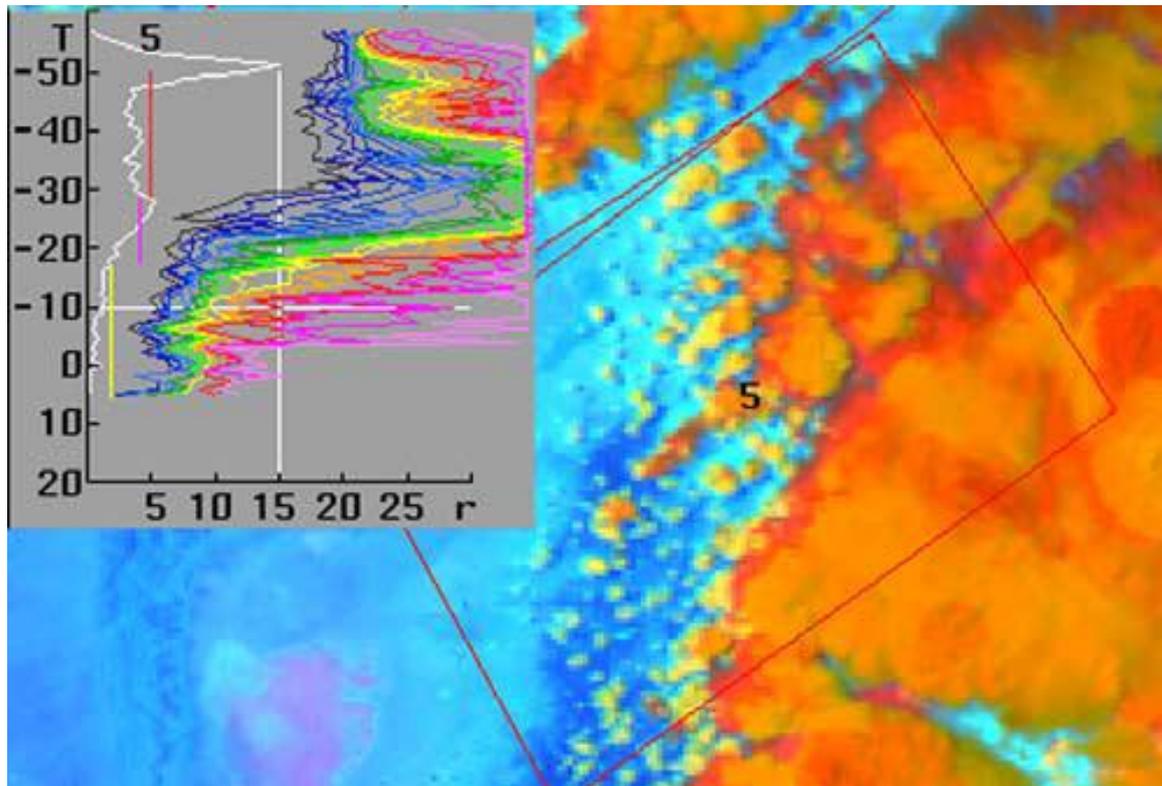
Figure 4.7-1: A T-re analysis of the cloud top microstructure of a Cb (cumulonimbus) that has an anvil partially formed by homogeneous freezing. The image is based on a NOAA AVHRR overpass on 8 June 1998, 2212 UTC, over New Mexico. The domain is 220 _ 150 AVHRR 1-km pixels. The image is an RGB composite where the visible channel modulates the red, 3.7 mm reflectance modulates the green, and 10.8 mm brightness temperature modulates the blue [after Rosenfeld and Lensky, 1998]. Brighter 3.7 mm reflectance (greener) means smaller cloud top particles. The inset shows the T-re lines for the clouds in the marked rectangle. The different coloured lines represent different T-re percentiles every 5% from 5% (leftmost line) to 100% (rightmost line), where the bright green is the median. The white line on the left side of the inset is the relative frequency of the cloudy pixels. The vertical lines show the vertical extent of the microphysical zones: yellow for the diffusional growth, green for the coalescence zone (does not occur in this case), and pink for the mixed phase and red for the glaciated zone. The glaciated cloud elements that do not exceed the -38°C isotherm appear red and have very large re that is typical of ice particles that form by heterogeneous freezing in a mixed phase cloud, whereas the colder parts of the anvil are coloured orange and are composed of small particles, which must have formed by homogeneous freezing of the cloud drops in the relatively intense updraft that was necessary to form the anvil portions above the- 38°C isotherm.

On the basis of the shapes of the T-r_e relations (see Figure 4.7-2) Rosenfeld and Lensky (1998) defined the following five microphysical zones in convective clouds:

1. The diffusional droplet growth zone is characterized by very slow growth of cloud droplets with depth above cloud base, indicated by shallow slope of dr_e/dT.

2. The droplet coalescence growth zone is characterized by large increase of the droplet growth rate dr_e/dT at T warmer than freezing temperatures, indicating rapid cloud-droplet growth with depth above cloud base. Such rapid growth can occur there only by drop coalescence.

3. The rainout zone is a zone where re remains stable between 20 and 25 μm, probably determined by the maximum drop size that can be sustained by rising air near cloud top, where the larger drops are precipitated to lower elevations and may eventually fall as rain from the cloud base. This zone is so named, because droplet growth by coalescence is balanced by precipitation of the largest drops from cloud top. Therefore the clouds seem to be raining out much of their water while growing. The radius of the drops that actually rain out from cloud tops is much larger than the indicated r_e of 20–25 μm, being at the upper end of the drop size distribution there.

4. The mixed phase zone is a zone of large indicated droplet growth rate, occurring at T < 0°C, due to coalescence as well as to mixed phase precipitation formation processes. Therefore the mixed phase and the coalescence zones are ambiguous at $0 < T < -38°C$. The conditions for determining the mixed phase zone within this range are specified by Rosenfeld and Lensky (1998).

5. The glaciated zone is a nearly stable zone of re having a value greater than that of the rainout zone or the mixed phase zone at T < 0°C.
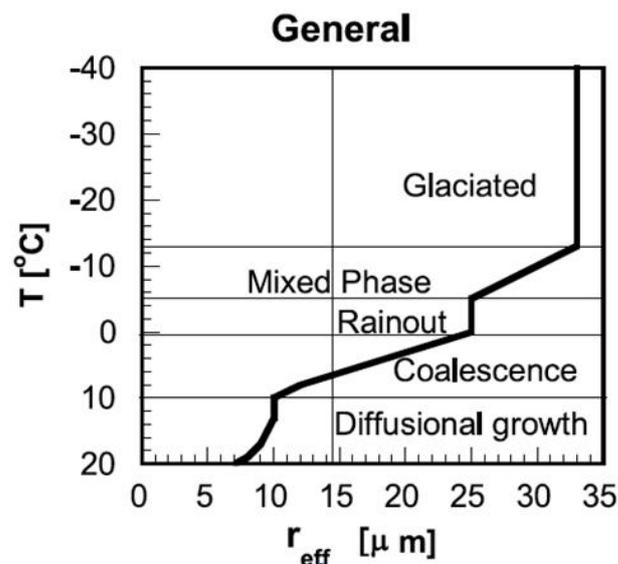

Figure 4.7-2: Classification scheme of convective clouds into microphysical zones, according to the shape of the T-re relations [after Rosenfeld and Woodley, 2003]. The microphysical zones can change considerably between continental and maritime clouds, calssified by their microphysical properties, as illustrated by Rosenfeld and Woodley (2003, Figure 6).

All these microphysical zones are defined only for convective cloud elements. Multilayer clouds start with small r_e at the base of each cloud layer. This can be used to distinguish stratified from convective clouds by their microstructure. Typically, a convective cloud has a larger re than a layer cloud at the same height, because the convective cloud is deeper and contains more water in the form of larger drops.

A microphysically continental cloud is defined as such when cloud condensation nuclei (CCN) concentrations are sufficiently large to induce a drop concentration that is sufficient to suppress drop coalescence and warm rain in the lowest several (2 to 3) km of the cloud. Even with small CCN concentrations, a sufficiently low cloud base temperature can always be found such that the diffusional zone of cloud drops in the T-r_e line will extend through the homogeneous glaciation temperature isotherm, even for moderate updraft velocities. This is the case for many of the high plains storms over the western USA, as already noted by Lindsey et al. (2006).

Alternatively, a cloud with an extremely large number of small droplets, such as in a pyro-Cb (see example given by Rosenfeld et al. (2006a, Figure 11), can occur entirely in the diffusional growth zone up to the homogeneous glaciation level even if it does not have very strong updrafts. In any case, a deep (>3 km) zone of diffusional growth is indicative of microphysically continental clouds, where smaller re means greater heights and lower temperatures that are necessary for the transition from diffusional to the mixed phase zone, which is a manifestation of the onset of precipitation.

Figure 4.7-2 illustrates the fact that a highly microphysically continental cloud with a warm base (e.g., >10°C) has a deep zone of diffusional cloud droplet growth even for weak updrafts (line A). The onset of precipitation is manifested as the transition to the mixed phase zone, which occurs at progressively greater heights and colder temperatures for clouds with stronger updrafts (line B). The glaciation temperature also shifts to greater heights and colder temperatures with increasing updrafts. From the satellite point of view the cloud is determined to be glaciated when the indicated re reaches saturation. This occurs when the large ice crystals and hydrometeors dominate the radiative signature of the cloud. Some super-cooled water can still exist in such a cloud, but most of the condensates are already in the form of large ice particles that nucleated heterogeneously and grew by riming and fast deposition of water vapour that is in near equilibrium with liquid water. Such was the case documented by Fridlind et al. (2004) in convective clouds that ingested mid-tropospheric CCN in Florida, where satellite-retrieved T-r_e relations indicated a glaciation temperature of -29°C (not shown).

Further invigoration of the clouds would shift upward the onset of mixed phase and glaciated zones. However, glaciation occurs fully and unconditionally at the homogeneous glaciation temperature of -38°C. Any liquid cloud drops that reach to this level freeze homogeneously to same-size ice particles. If most cloud water was not rimed on ice hydrometeors, it would have a radiative impact on the retrieved effective radius and greatly decrease the re of the glaciated cloud, as shown in line C of Figure 4.7-3 (a) and (b). Yet additional invigoration of the updraft would further shift upward and blur the onset of the precipitation, and reduce the re of the glaciated cloud above the -38°C isotherm, until the ultimate case of the most extreme updraft, where the T-r_e profile becomes nearly linear all the way up to the homogeneous freezing level. This situation is illustrated by line E in Figure 4.7-3 (a) and (b)

This method has been shown to work best for clouds with exposed feeders. Therefore, convective clouds best show their severe weather potential while they are still in their early developing stages. This is typically 1 to 2 hours before the occurrence of the tornado or large hail. The T-r_e relations are analyzed by an automatic detection algorithm for the detection of a "severe storm signature". The suspected clouds are then identified and flagged as "Early Alerts" (EA). The method objective is to predict when and where severe weather is most likely to occur one to two hours prior to the actual event. As such, an EA normally comes after issuance of a severe weather watch but before the warning when the event is underway.
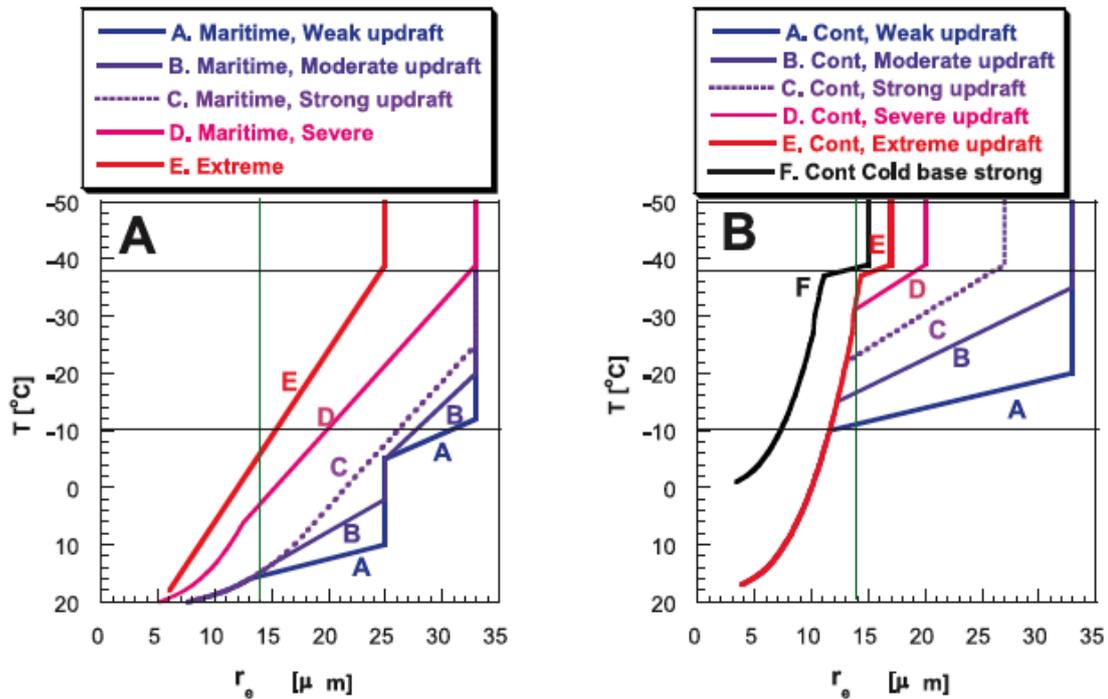

Figure 4.7-3: A conceptual model of the way T-re relations of convective clouds are affected by enhanced updrafts to extreme values. The vertical green line represents the precipitation threshold of re = 14 µm [Rosenfeld and Gutman, 1994]. The horizontal line at T = -38°C represents the homogeneous freezing isotherm. (a) Microphysically maritime clouds with low and warm bases and small concentrations of CCN and (b) clouds with high CCN concentrations or high and cold bases. In reality most cases occur between these two end types.

Lindsey et al. (2006) examine the reflectivity of thunderstorm tops as measured by the GOES 3.9 µm albedo product. A climatological analysis reveals that environmental conditions in mountainous regions of the U.S. favor storms with enhanced 3.9 µm albedo, while storm-top reflectivity over much of the eastern U.S. is lower. Model results suggest that these storm-top 3.9 µm albedo differences are due to variations in ice crystal size and number concentration; smaller ice crystal distribution mean diameters result in larger 3.9 µm albedos. Reanalysis data is used to show that highly reflective thunderstorms tend to occur in environments with relatively dry boundary layers, steep lapse rates, large vertical shear, and small distances from cloud base to the homogeneous freezing level. A physical mechanism, called the cloud droplet residence time, is presented which explains why storms in mountainous areas have larger mean 3.9 µm albedos. If proven to be valid, thunderstorm updraft strength information can be obtained from GOES 3.9 µm albedo measurements.

Levizzani and Setvak (1996 and Setvák et al. (2003) discuss observations of thunderstorms with highly reflective plumes which appear to be ejected from a thunderstorm's overshooting top. If a thunderstorm with fairly uniform 3.9 μm albedo values suddenly begins ejecting smaller ice crystals from its updraft, results of the Lindsey et al. (2006) study suggest that its updraft may have recently strengthened, allowing more tiny cloud droplets to freeze homogeneously. This observation also has potential nowcasting applications.

4.8   Aviation Turbulence Indicators and Cloud-Induced Turbulence

Aside from overshooting tops, a number of signatures in satellite imagery have been found in association with significant aviation turbulence events. These include newly developing convective storms, transverse cirrus cloud bands, and the rapid lateral expansion of a convective anvil cloud. (Bedka et al., 2007). Transverse bands, also known as "radial cirrus", are long-lived features in the upper-level outflow of during the mature and decaying stages of mesoscale convective systems. (Lenz et al., 2009). Lenz et al describe that transverse bands appear to originate along the edge of the outflow of the convective system in most cases, though some cases exhibit evidence for the production of banded structures earlier in the storm life cycle closer to the OT region. They also showed that nearly every case of transverse bands found over the U.S. during the 2006 warm season was associated with at least light turbulence and just less than half of these cases were associated with moderate or greater intensity turbulence. This finding suggests that the presence of bands in satellite imagery may be used to nowcast a high likelihood for aviation turbulence. Transverse bands are not unique to mesoscale convective systems; they have also been observed in jet streams, tropical cyclones, and extra-tropical cyclones (Knox et al. 2009). Trier et al. (2010) provide an explanation of the formation mechanisms and dynamics of transverse bands through analysis of satellite imagery and cloud resolving model output.

4.9   Satellite Rainfall Estimation

Precipitation is the most important variable in the hydrological budget of the Earth. So the better understanding of the spatial and temporal distribution of precipitation is fundamental for any hydrologic and climatic applications. Unfortunately, the inhomogeneity of temporal and spatial distribution of rainfall combined with the lack or the sparse presence of ground measurement makes it ones of the most difficult parameter to quantify as an input to hydrological model.

Meteorological satellites provide a unique opportunity for monitoring the precipitation for regions where ground measurement is limited and consistent with the accuracy required by hydrologists.

Techniques for estimating precipitation from infrared and/or visible satellite data have existed almost as long as the data have been available. (Scofield and Kuligowski, 2003) Rainfall rates are generally derived from cloud-top infrared (IR) brightness temperature, which is related to cloud-top height for optically thick clouds below the tropopause. This relationship assumes that the cloud height is related to cloud thickness—an assumption that holds reasonably well for active convective clouds but is problematic for nimbostratus clouds (for which rain rates are often underestimated because of the relatively warm cloud tops) and non-precipitating cirrus clouds (which may be incorrectly identified as

precipitating clouds because of their low brightness temperatures) (Scofield and Kuligowski, 2003). Visible cloud reflectances can be used as supplementary information to somewhat mitigate this problem. All visible and infrared precipitation estimation schemes are necessarily indirect because the radiation does not penetrate through the cloud. The cloud's brightness temperature and visible reflectance may be related to the rain falling from it, but the raindrops themselves are not directly sensed (Kidder and Vonder Haar, 1995).

Microwave instruments have been shown to yield more reliable information concerning instantaneous precipitation rates on account of their ability to "see" through cloud tops and detect directly the presence of actual precipitation particles within and below the clouds. However, as microwave instruments are currently only available onboard satellites in low earth orbit, they do not provide a continuous monitoring of rainfall over a given location.

One approach is to combine geostationary and low orbit satellite observations. This kind of multi-platform algorithm provides global precipitation estimation merging high-quality, sparsely sampled data from low earth orbit satellites (e.g. Metop, NOAA series, DMSP, i.e. LEO/MS in general) with continuously sampled data from geostationary satellites (e.g. GEO/IR).

The following two sections present three rainfall estimates, one is the Convective Rainfall Rate (CRR) of the NWC-SAF software package, the other two are the H-SAF rainfall estimates PR-OBS3 and PR-OBS4.

4.9.1   Convective Rainfall Rate (CRR) Product of the NWC-SAF

The NWCSAF Convective Rainfall Rate (CRR) product is a nowcasting tool providing information on convective and convectively-induced hourly rainfall accumulations (see **Error! Reference source not found.**) and instantaneous rain rates (Rodriguez and Marcos, 2010). This product provides forecasters with some complement to other NWC-SAF products related to rain and convection monitoring such as the modules PGE04 (Precipitating Clouds) and PGE02 (Cloud Type). An empirical relationship between cloud height/thickness, probability of rainfall occurrence, and the intensity of precipitation is the fundamental basis of the CRR algorithm. Information about cloud top height and about cloud thickness can be obtained, respectively, from the IRW BT and from the VIS reflectance (Scofield, 1997; Vincente and Scofield, 1996). The WV-IRW BTD is also a useful parameter for extracting deep convective cloud with heavy rainfall.

The final CRR products are derived via calibration of IRW BT, VIS reflectance, and WV-IRW BTD with ground based radar fields. Two radar databases were used for this effort, the first being data from 2004 through 2006 over Spain and the second being from 2006 over the Nordic countries.

Environmental and orographic conditions can affect convective precipitation rates, often more than the convectively-induced stratiform rain cases, therefore some corrections can be applied to adjust the rain rates. Moisture correction decreases/increases rain rates in a dry/moist environment. Cloud growth rate correction studies the temporal variability of cloud tops to decrease rain rates when cloud systems are decaying. Parallax correction tries to correct parallax effect applying a spatial shift to every pixel with precipitation accordingly. An orographic correction takes into account atmospheric flows over the

mountains and characteristics of the flow disturbances created by the mountains themselves to adjust rain rates as appropriate. Finally, as lightning activity is related with convection, a lightning algorithm can be applied. This algorithm uses some characteristics of Cloud-to-Ground lightning flashes as time distance between lightning events, location and spatial density of lightning in a time interval, to include or increase convective precipitation not detected through the satellite data.

As IRW and VIS radiation does not penetrate through the cloud, precipitation techniques based on those information use cloud top characteristics to infer precipitation. For this reason CRR precipitation pattern closely follows cloud top features, usually elading to a larger extent of the satellite derived rain areas when compared to radar. Inaddition, due to the close dependence of CRR on the cloud top temperature, the CRR algorithm usually performs better for colder cloud tops.

An extended validation of the CRR product has been carried out using data corresponding to convective events occurred along the whole year 2008 over Spain. A subjective validation comparing CRR with lightning detection information over Spain has also been carried out. Other validations using data of convective events occurred in the 2009 summer period over Hungary has also been performed against both radar and rain gauges (Labo et al., 2009). More information on the product and on the validation can be found on the NWC_SAF web site http://www.nwcsaf.org.

The CRR product is also used by the Rapidly Developing Thunderstorms (RDT) SAF product (see section 4.2.1) as an object attribute and to aid in the convective diagnostics in case of high rain rates.
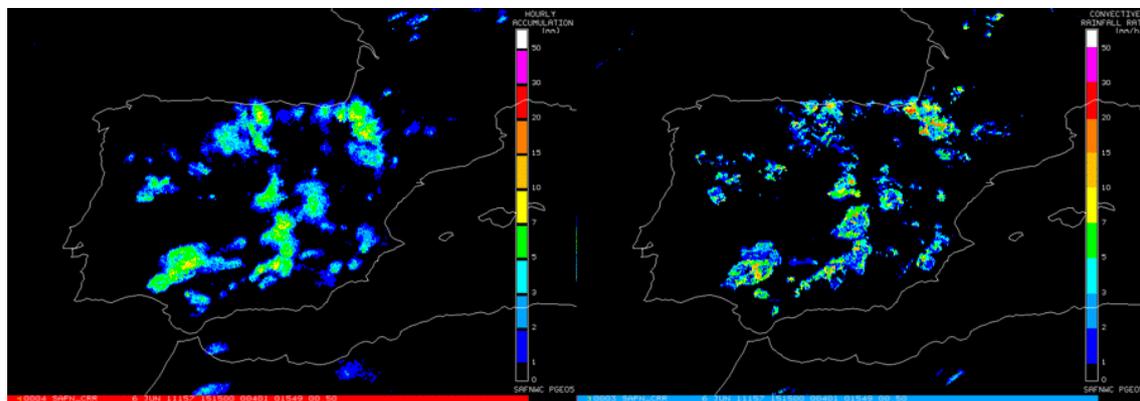

Figure 4.9-1: NWCSAF CRR hourly rainfall accumulation (left) and instantaneous rates (right) at 1515 UTC on 6 June 2011.

4.9.2 Precipitation Products Provided by the H-SAF

The H-SAF has developed an algorithm to derive the precipitation rate at ground by GEO/IR supported by LEO/MW (PR-OBS-3). PR-OBS-3 (see Figure 4.9-2.) is thus a multisensory algorithm based on the rapid-update technique (RU), which was originally developed at the Naval Research Laboratory (Turk et al., 2000; Turk and Miller, 2005). RU is a technique where passive microwave (MW) is blended with infrared (IR) observations for the retrieval of instantaneous precipitation intensities. Rain rates obtained from microwave measurements of the Special Sensor Microwave/Imager (SSM/I) and by the Advanced Microwave Sounding Units (AMSU-A, AMSU-B) and Microwave Humidity Sounder (MHS) (PR-OBS-2 and PR-OBS-3) are combined with the IR10.8 MSG-SEVIRI brightness temperatures.
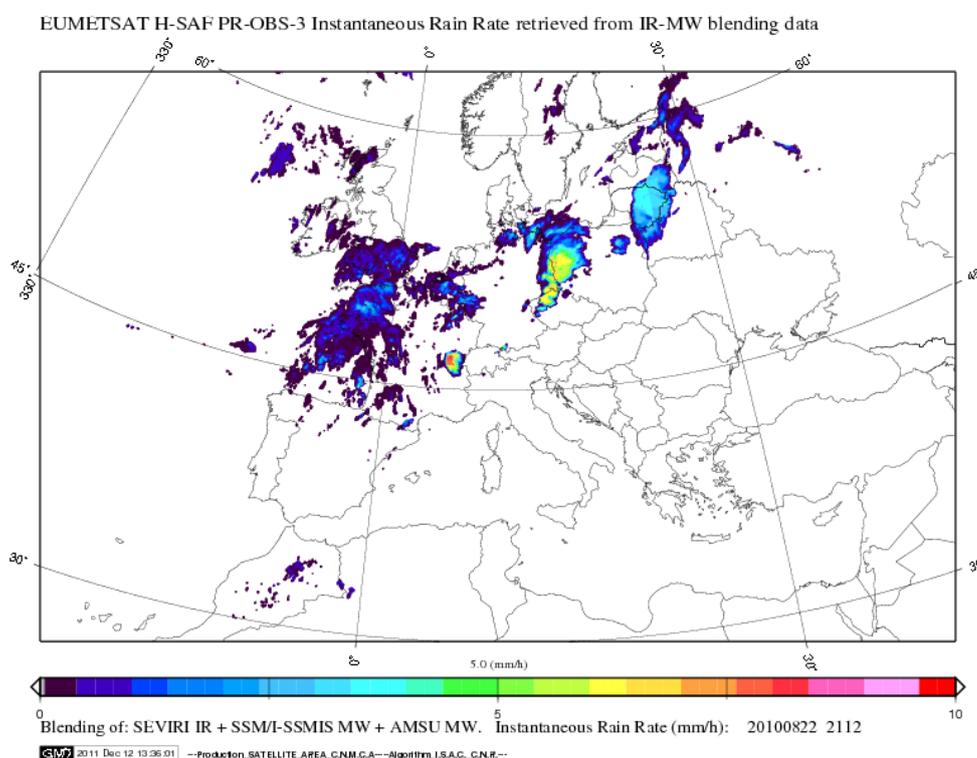

Figure 4.9-2: HSAF PR-OBS3 Instantaneous Rain Rate retrieved from IR-MW blending data at 2112 UTC on 22 August 2009.

The RU algorithm is based on a collection of time and space overlapping SEVIRI IR images and Low Earth Orbit (LEO) MW radiometers. As a new MW swath is available, the MW-derived pixels are paired with the time and space coincident geostationary (GEO) IR10.8 brightness temperatures. Coincident data are subsequently located in a geographical latitude-longitude grid (2.5° x 2.5°), and for each grid box the histogram of the IR brightness temperatures and of the corresponding MW rain rates is built. Geolocated IR temperature vs. MW rain rates relationships are produced by combining the histograms by means of a probabilistic histogram matching technique (Calheiros and Zawadzki, 1987), thus assigning precipitation intensity value at each SEVIRI pixel. As soon as a grid box is refreshed with new data, the corresponding relationship is updated accordingly.

Relationships older than 24 h with respect to the acquisition time of the geostationary observations are considered no longer reliable, and consequently a conventional rain intensity value equal -1 is assigned, until a refresh of the relationship is done.

A preliminary pre-screening of the cloudy scenario is performed using the "Cloud Type" product from the NWC-SAF, which cleans up the scene from cirrus, and broken and semitransparent clouds. The cloud classification is essential to improve the performances of the blended technique, in particular for preventing erroneous precipitation assignments typical of the IR precipitation retrieval techniques

A second H-SAF algorithm of interest is the PR-OBS-4 – the precipitation rate at ground by LEO/MW supported by GEO/IR. PR-OBS-4 (see Figure 4.9-3.) is based on the Climate Prediction Center (CPC) morphing method (CMORPH), which is alternative to the RU (product PR-OBS-3) for combining GEO/IR radiances and LEO/MW rainfall estimates and was proposed by Joyce et al. (2004) using an entirely different combination concept. As for the RU algorithm, precipitation estimates are derived from LEO MW observations.
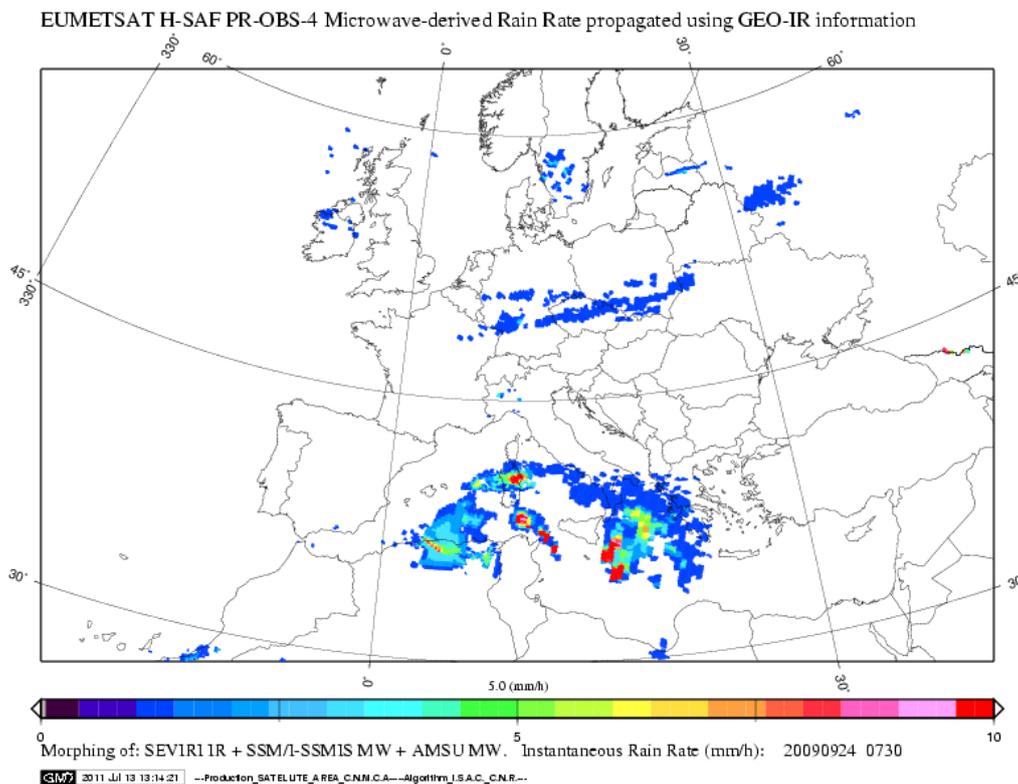

Figure 4.9-3: HSAF PR-OBS4 Microwave-derived Rain Rate propagated using GEO-IR information at 0730 UTC on 24 September 2009.

5   END-TO-END CONVECTION NOWCASTING TECHNIQUES

5.1   The COALITION approach: an EUMETSAT Fellowship research project at MeteoSwiss

COALITION is a new heuristic model that provides early assessments of potential thunderstorms in terms of severity and location, through the rapid modelling of the available predictors (Nisi et al., 2011). Numerical weather prediction models provide good forecasts on regional to global scales, but they have difficulties in predicting the exact time and location of small-scale phenomena like thunderstorms. Current heuristic methods such as satellite and radar imagery, model output post-processing, satellite nowcasting products, neural network methods or other statistical methods focus on specific aspects. For example, existing radar-based solutions are well suitable for detecting and extrapolating already existing thunderstorms when hydrometeors occur. The detection of convective features in early stage still remains a difficult task, especially in complex terrain. The orographic forcing is very important in the Alpine region, where mountain ridges and valleys affect thunderstorm processes through its whole life-cycle (triggering, reactivation and decaying). Information characterizing the storm environment, in particular retrieved by satellite data, can become very useful for detecting the early stages of a convective process and for predicting their development. COALITION merges the most suitable and promising predictors characterizing thunderstorms cells. The algorithm extracts and merges information at different scales provided by (see also Figure 5.1-1):

- Meteosat Second Generation Rapid Scan data (Cloud Top Temperature (CTT) and Convection Initiation (CI)),
- SAF Nowcasting products (Rapid Developing Thunderstorm (RDT), Cloud Top Temperature and Height (CTTH)),
- Radar data provided by the Swiss weather radar network (Vertical Integrated Liquid (VIL) content),
- Numerical Weather Prediction data (COSMO-2),
- Orographic information expressed in terms of a lightning climatology and directional slope gradients.
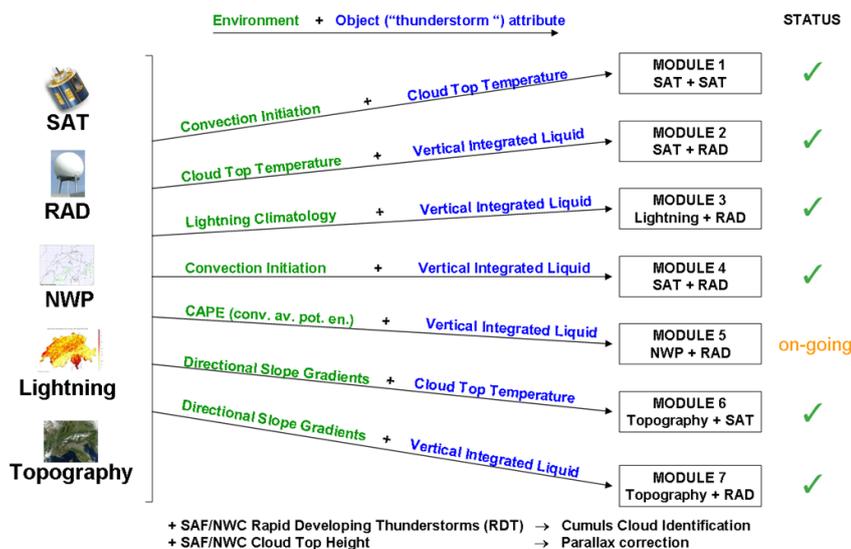

Figure 5.1-1: COALITION input data and implemented modules.

Depending on their context and scale some of the aforementioned data are used to identify objects, which are confined by external algorithms (NWC-SAF Rapid Developing Thunderstorms) or dedicated rules (e.g. temperature thresholds for cloud top, reflectivity thresholds for convective radar cells). In order to describe the environment surrounding the objects, some parameters among the available gridded fields have been selected.

The COALITION algorithm merges convective signatures (predictants) as object attributes of an object (e.g. Cloud Top Temperature, Vertical Integrated Liquid) and environments, considered as an external field describing the conditions surrounding the object (predictors).

Severe convection predictors and evolving thunderstorm properties are considered as interacting elements. The general concept behind COALITION is that external fields have the ability to affect the evolution of a thunderstorm attribute. Conceptually, the method is very similar to solving the problem of a generalized dynamics of a particle within a potential field, with minimization of the action.

Couplings are defined whenever possible through physical conservation laws. Otherwise, semi empirical rules (based on forecaster's experience and/or on conceptual models) are applied as functions (momentum or energy). The forecast corresponds to the evolution of the object attributes, resulting from the solution of Hamilton equation (read below for further explanation of parameters):

$$H(q, p, t) = \frac{p^2}{2m} + f(t)q^2$$

For each coupling module, a simplified one-dimensional model of type (1) is assumed, where q represents an observed thunderstorm attribute (e.g. CTT, VIL), p the correspondent momentum, m a mass of the object inertia and f(t) a function of the correlation between the object attribute evolution and the external field.

Six modules using several kinds of data provided by different sources have already been implemented; an additional one is still under development. Two modules provide ensemble forecasts of the evolution of Cloud Top Temperature; the remaining five modules provide ensemble forecasts of the Vertical Integrated Liquid content of thunderstorm cells. All forecasts are calculated every five minutes for the following hour.
Table *5.1-1* summarizes all modules:

Module number	Data combination	Heuristic approach
Module 1 (SAT + SAT)	Evolution of the CTT based on the environment defined in terms of the Convection Initiation product (Mecikalski et al 2010)	Stronger Convection Initiation signal of a convective cell → more energy is available for its cloud top cooling (towering of the cloud)
Module 2 (SAT + RAD)	Evolution of the VIL based on the environment defined in terms of CTT.	Faster cooling of the cloud top of a convective cell → more energy is available for increasing its VIL
Module 3 (Lightning + RAD)	Evolution of the VIL based on the environment defined in terms of a lightning climatology.	Higher density of cloud to ground lightning over a specific area → more energy is available for increasing the VIL of a convective cell developing in this area
Module 4 (SAT + RAD)	Evolution of the VIL based on the environment defined in terms of the Convection Initiation product (Mecikalski et al, 2010).	Stronger Convection Initiation signal of a convective cell → more energy is available for increasing its VIL
Module 5 (NWP + RAD)	Evolution of the VIL based on the environment defined in terms of the Convective Available Potential Energy (CAPE)	Higher instability values → more energy is available for increasing the VIL of a convective cell developing in this area
Module 6 (Topography + SAT)	Evolution of the CTT based on the environment defined in terms of orographic information (slope gradients).	A convective cell is moving towards a mountain (upslope) → more energy is available for its cloud top cooling (towering of the cloud)
Module 7 (Topography + RAD)	Evolution of the VIL based on the environment defined in terms of orographic information (slope gradients).	A convective cell is moving towards a mountain (upslope) → more energy is available for increasing its VIL

Table 5.1-1: Summary of the product merged in the different modules implemented in COALITION at current status (December 2011).

The model takes orographic forcing into account in two ways. Module 3 integrates a lightning climatology over the Alpine area; this is composed of 10 years of data of cloud-to-ground lightning. The heuristic concept behind this choice is that the higher the mean value of cloud-to-ground strokes per year over a given area, the greater is the probability that a convective cell developing over this area increases its intensity.

Modules 6 and 7 consider the orographic forcing through the "directional slope gradients (DSG)". It is expected that if a convective cell is moving towards a mountain, the upslope gradient will have a positive effect and therefore the cell intensity will increase. On the other hand, if the cell is moving away from the mountain (downslope gradients) or over a flat terrain, this will have a neutral effect.

The diagrams presented in Figure 5.1-2 show the comparison between the VIL forecast (coloured lines) provided by modules 2, 3, 4 and 7. Four different convective cells are analyzed, two of them are severe thunderstorms and the remaining ones represent weak thunderstorm events. The forecast reference has been selected according to the following criteria:

- for heavy thunderstorms the reference represents the maximal measured VIL value of the considered cell at the time when the MeteoSwiss forecasters issued a severe thunderstorm warning
- for the weak ones the reference represents the maximal measured VIL value considering the whole life cycle of the cell.
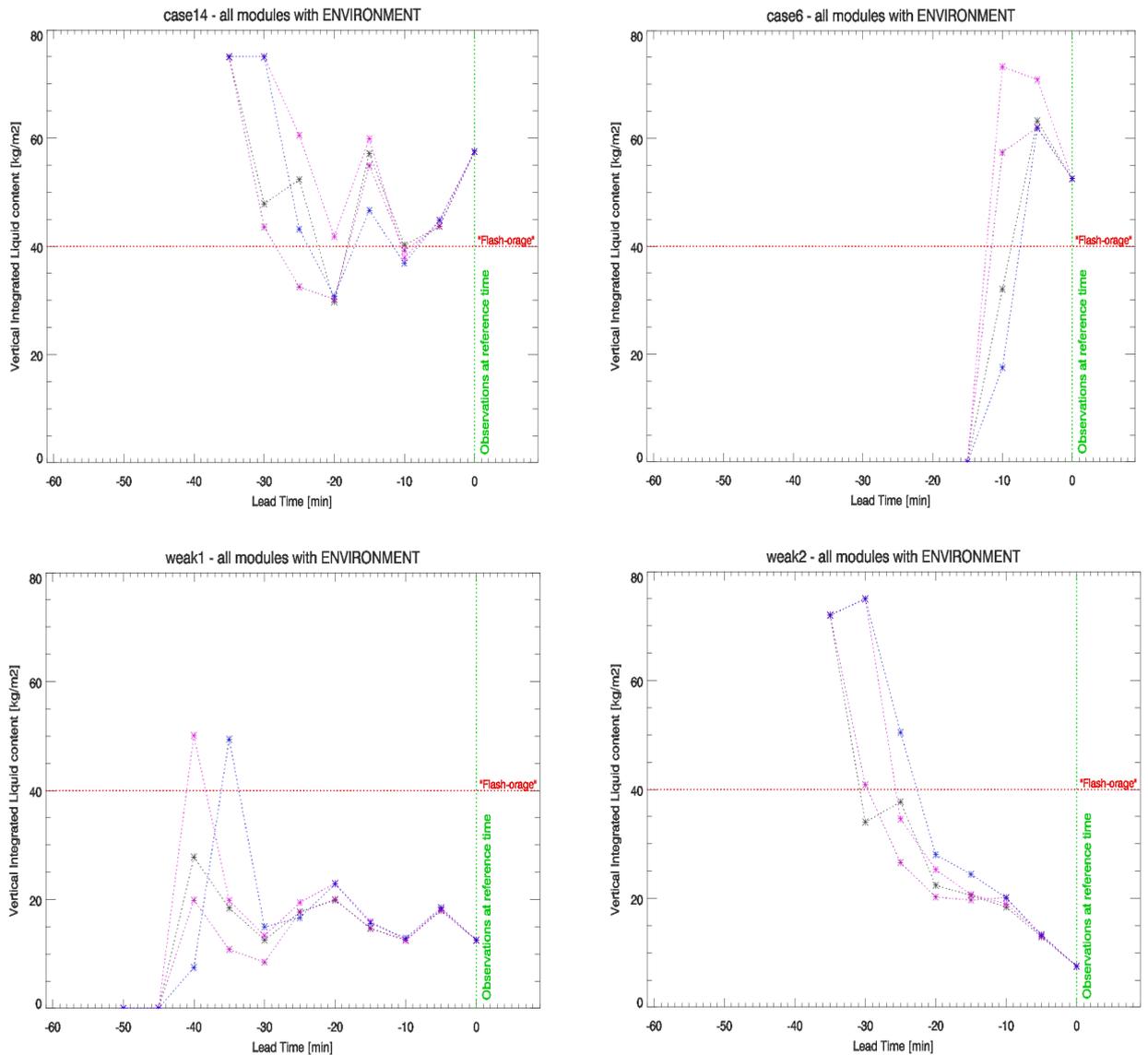
Figure 5.1-2: Comparison of the forecasted Vertical integrated Liquid (VIL) for four different thunderstorm cells (two severe and two weak). Different colours are used to show forecasts produced by different modules.

As expected the differences between the forecasts increase with the lead time. For severe thunderstorms the forecasts have in general a good forecasting skill up to 20-25 minutes in advance. Explosive cells are an exception, in this type of cases useful skills reach at most a 10 minutes lead time (e.g. for the severe thunderstorm of Figure 5.1-2 on the right). The main difficulty is given by the handling of large increases of the VIL (e.g. from 0 to 60 kg/m2 in 10 minutes only). Although the environments show favourable conditions for severe weather, it is very difficult to forecast extremely rapid changes in the thunderstorm attributes.

As shown in Figure 5.1-2 the VIL forecast for weak or moderate thunderstorm cells has a good skill for longer lead times, in general up to 25-30 minutes. In this kind of cases, most of the external environments show less favourable conditions for severe weather development. The differences between the module forecasts are smaller and do not show significant increases in the intensity of the thunderstorm attributes.

The diagrams presented in Figure 5.1-3 show the comparison between the CTT forecast (shown with two colours) provided by modules 1 and 6. Four different convective cells are analyzed, two of them are severe thunderstorms and the remaining ones represent weak thunderstorm events. Similar to the VIL comparison, the forecast reference has been selected according to the following criteria:

- for severe thunderstorms the reference represents the minimal measured CTT value of the considered cell at the time when the MeteoSwiss forecasters issued a severe weather warning
- for the weak ones the reference represents the measured CTT value at the moment when the maximal VIL value has been measured. The whole life cycle of the cell is considered.
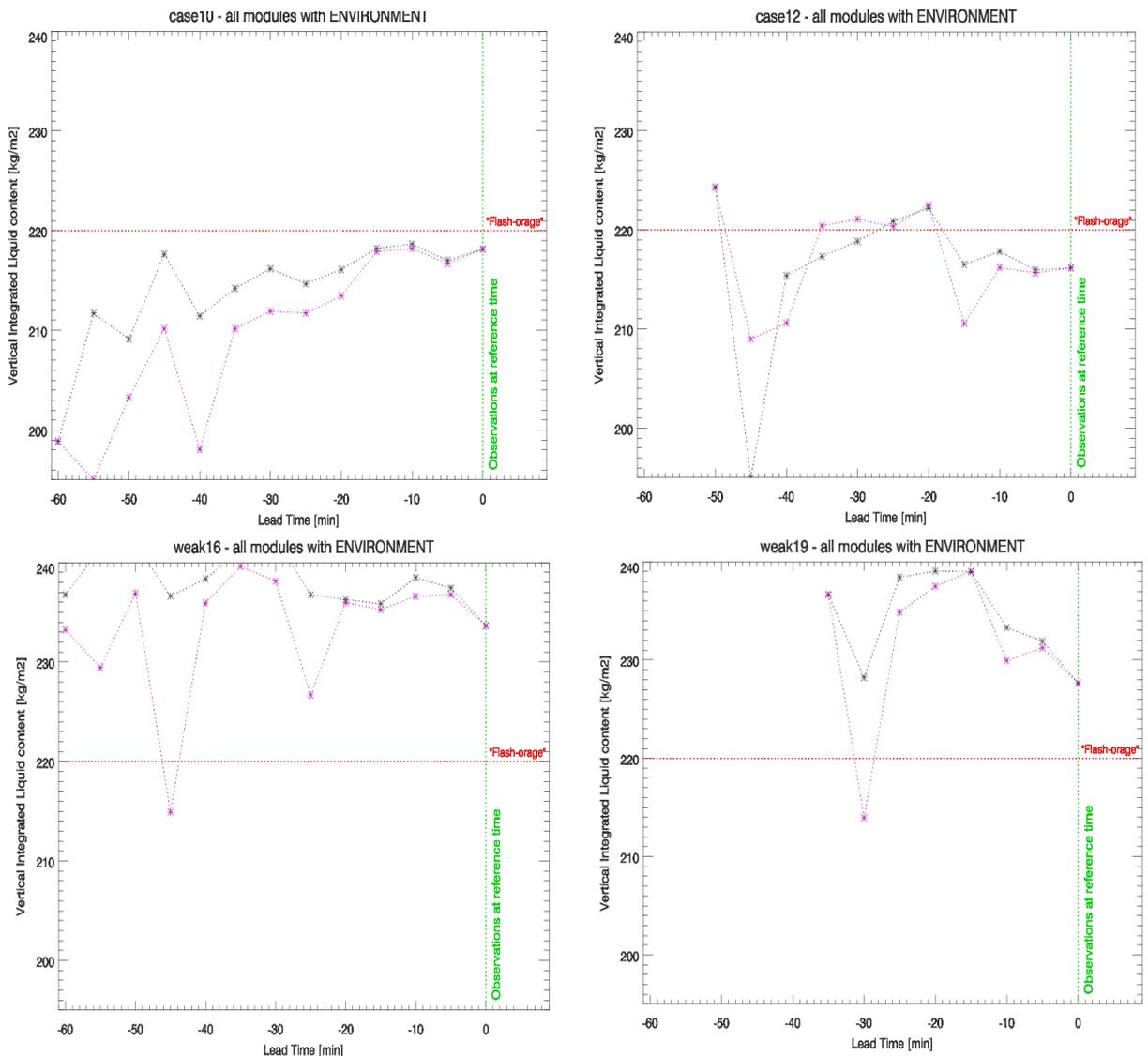

Figure 5.1-3: Comparison of the forecasted Cloud Top Temperature (CTT) for four different thunderstorm cells (two severe and two weak). Different colours are used to show the forecast of different modules.

Generally, for both weak and severe convective cases, the CTT forecast provided by the two modules shows a good skill for long lead times, in some cases up to 60 minutes. This very high probability of detection is set against an increased false alarm rate. In fact, it is more difficult to discriminate severe and weak thunderstorm cells based on CTT than based on VIL. Even weak thunderstorm cells can often reach very cold CTT of about 215 K. The two modules providing CTT forecasts will be used in the early phases of a convective cell, when precipitation is not yet detected or it is very weak. These are only preliminary assessments: the present work includes the use of the forecast uncertainty and the combination of different modules (optimal weighted combination, fuzzy logic) for assessing more rigorously the forecast quality and to give to the forecaster the best probabilistic information about the development of convection intensity. Diagrams in Figure 5.1-4 show a first global validation of the algorithm, where the forecast of the modules are considered together with a simple linear combination. In the first 25 minutes lead time the probability of detection (POD) decreases from 74% to 60% and the false alarm rate increases from 0% to 28%. These first results could already be considered acceptable and useful for automatic nowcasting of heavy thunderstorms. The skill scores for lead times greater than 25 minutes, as shown in Figure 5.1-4, should be evaluated with caution. In fact, the development phase of a convective cell rarely lasts longer than 25 to 30 minutes. For such a lead time, POD and FAR values are calculated over a small sample of data and therefore the statistics are not representative.
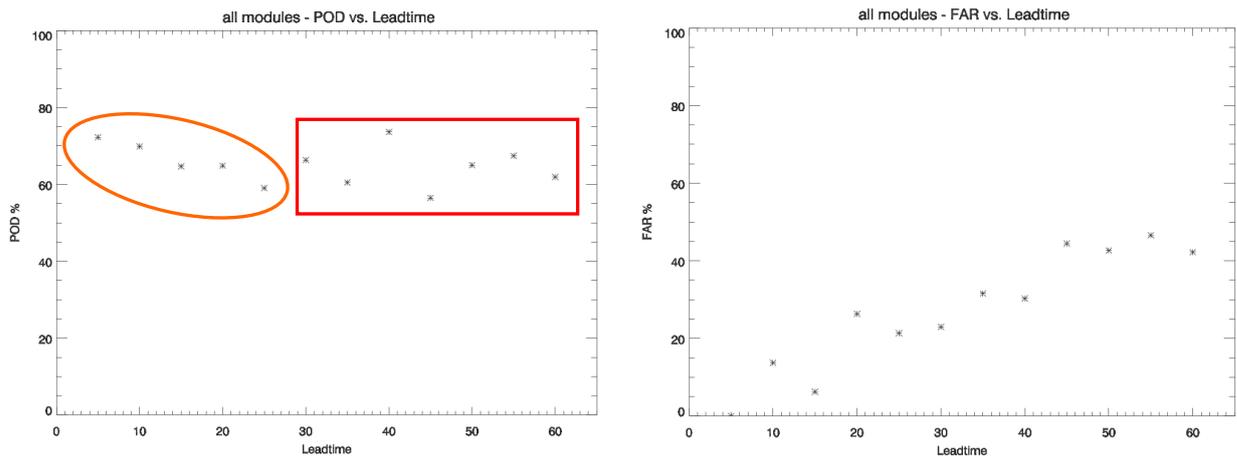

Figure 5.1-4: First validation of COALITION results. For this preliminary validation the convective cells are simply classified in two groups: severe thunderstorms (if VILmax >= 40 kg/m2), weak/moderate thunderstorms (if VILmax < 40 kg/m2).

The on-going work includes the refinement of the model modules as well as their combination in order to provide maps for the likelihood of severe weather in the Alpine area.

COALITION strengths

- COALITION merges advanced satellite, radar, NWP data and other products and summarizes the information about likelihood for severe convection into a single probabilistic map.
- The orographic forcing is taken into account by the algorithm through a lightning climatology and the directional slope gradients.
- A first validation shows that COALITION can forecast severe convective thunderstorms with good skill score for lead times up to 25 minutes, where the POD decreases from 74% to 60% and the FAR increases up to 28%.
- The model has a great performance in cases of isolated thunderstorms, orographic induced convection and pre-frontal thunderstorms.
- The system is developed in C and the computing time is compatible with the Nowcasting requirements
- The system is modular, the user can select which modules (and therefore which products) shall be used. This offers the possibility to test a limited version of COALITION over regions in different parts of the world
- The system is flexible: new products can be easily added, existing products can be easily substituted
- MeteoSwiss plans to test COALITION in real time during the 2012 convective season. Forecaster's feedbacks will be collected and will constitute the base for further algorithm improvements

COALITION weaknesses

- COALITION strongly depends on the performance of the SAF Nowcasting Rapid Developing Thunderstorms (RDT). In order to detect convective cumulus clouds when no precipitation is occurring, some RDT thresholds have been lowered.
- COALITION has difficulties in handling embedded convection in cold fronts as well as very large increases of the vertical integrated liquid in case of explosive thunderstorms. In some cases the maximal vertical integrated liquid content observed by radar increases from 5-10 kg/m2 to more than 40 kg/m2 in 5-10 minutes
- Feedbacks about the real-time performances not yet available

6 REFERENCES

Ackerman, S.A., 1996: Global satellite observations of negative brightness temperature differences between 11 and 6.7 μm. *J. Atmos. Sci.*, **53**, 2803–2812.

Adler, R.F., and D.D. Fenn, 1979: Thunderstorm intensity as determined from satellite data. *J. Appl. Meteor.*, **18**, 502–517.

Adler, R. F., M. J. Markus, D. D. Fen, G. Szejwach, and W. E. Shenk, 1983: Thunderstorm top structure observed by aircraft overflights with an infrared radiometer. *J. Appl. Meteor. and Climatol.*, **22**, 579-593.

Adler, R.F., M.J. Markus, and D.D. Fenn, 1985: Detection of severe Midwest thunderstorms using geosynchronous satellite data. *Mon. Wea. Rev.*, **113**, 769–781.

Adler, R.F., and R.A. Mack, 1986: Thunderstorm cloud top dynamics as inferred from satellite observations and a cloud top parcel model. *J. Atmos. Sci.*, **43**, 1945–1960.

Antonelli, P, S. Puca, F. Zauli, R. Bennartz, L. de Leonibus, W. Feltz, and H. Woolf, 2010: Validation of Satellite Rain Rate Estimation with Ground-Based Observing Systems. Integrated Ground-Based Observing Systems. D. Cimini et al. (eds.), Springer-Verlag Berlin Heidelberg 2010. pp 241-278.

Arnaud, Yves, Michel Desbois, Joel Maizi, 1992: Automatic Tracking and Characterization of African Convective Systems on Meteosat Pictures. *J. Appl. Meteor.*, **31**, 443–453.

Bedka K, Feltz W, Mecikalski J, Sharman R, Lenz A, Gerth J. 2007. Satellite signatures associated with significant convectively-induced turbulence events. *Proc. Joint 2007 EUMETSAT Meteorological Satellite Conf. and the 15th Satellite Meteorology & Oceanography Conf. of the American Meteorological Society*, Amsterdam, The Netherlands. EUMETSAT. http://www.eumetsat.int/Home/Main/Publications/Conference_and_Workshop_Proceeding s/groups/cps/documents/document/pdf_conf_p50_s4_01_bedka_p.pdf [Accessed: 20 January 2009]

Bedka, K. M., J. R. Mecikalski, 2005: Application of Satellite-Derived Atmospheric Motion Vectors for Estimating Mesoscale Flows. *J. Appl. Meteor.*, **44**, 1761–1772.

Bedka, K. M., J. C. Brunner, R. Dworak, W. F. Feltz, J. A. Otkin, and T. Greenwald, 2010: Objective satellite-based overshooting top detection using infrared window channel brightness temperature gradients. *J. Appl. Meteor. and Climatol.*, **49**, 181-202.

Bedka, K. M., J. Brunner, and W. Feltz, 2010: NOAA NESDIS Center for Satellite Applications and Research Algorithm Theoretical Basis Document: Overshooting Top and Enhanced-V Detection for the GOES-R Advanced Baseline Imager Program.

Bedka, K. M., and P. Minnis, 2010: GOES 12 observations of convective storm variability and evolution during the Tropical Composition, Clouds and Climate Coupling Experiment field program. *J. Geophys. Res.*, **115**, DOI: 10.1029/2009JD013227

Bedka, K. M., 2011: Overshooting cloud top detections using MSG SEVIRI infrared brightness temperatures and their relationship to severe weather over Europe. *Atmos. Res.*, **99**, 175-189.

Berendes T. A., J. R. Mecikalski, W. M. MacKenzie Jr., K. M. Bedka, and U. S. Nair, 2008: Convective cloud identification and classification in daytime satellite imagery using standard deviation limited adaptive clustering, *J. Geophys. Res*., **113**, D20207, doi:10.1029/2008JD010287.

Brooks, H. E., 2009: Proximity soundings for severe convection for Europe and the United States from reanalysis data. *Atmos. Res.,* **93**, 546-553.

Brunner, J.C., S.A. Ackerman, A.S. Bachmeier, and R.M. Rabin, 2007: A quantitative analysis of the enhanced-V feature in relation to severe weather. *Wea. Forecasting*, **22**, 853–872.

Carvalho, L., and C. Jones, 2001: A satellite method to identify structural properties of mesoscale convective systems based on the maximum spatial correlation tracking technique (MASCOTTE). J. Appl. Meteor., 40, 1683–1701.

Chappell, C. F.,1986: Quasi-stationary convective events. Mesoscale Meteorology and Forecasting, P.S. Ray, Ed., Amer. Meteor. Soc., 289-310.

Chemel C., M. R. Russo, J. A. Pyle, R. S. Sokhi, and C. Schiller (2008), Quantifying the imprint of a severe hector thunderstorm during ACTIVE/SCOUT-O3 onto the water content in the upper troposphere/lower stratosphere. *Mon. Wea. Rev.*, **137**, 2493-2514.

Chung, E. S., B. J. Sohn, and J. Schmetz, 2008: CloudSat shedding new light on high-reaching tropical deep convection observed with Meteosat. *Geophys. Res. Let.*, **35**, doi:10.1029/2007GL032516

Corfidi, S. F., J. H. Meritt, J. M. Fritsch, 1996: Predicting the Movement of Mesoscale Convective Complexes. *Wea. Forecasting*, **11**, 41–46.

Cornman, L. B., and B. Carmichael, 1993: Varied research efforts are under way to find means of avoiding air turbulence. *ICAO Journal*, **48**, 10-15.

Corti, T., B.P. Luo, M. de Reus, D. Brunner, F. Cairo, M.J. Mahoney, G. Martucci, R. Matthey, V. Mitev, F.H. dos Santos, C. Schiller, G. Shur, N.M. Sitnikov, N. Spelten, H.J. Vössing, S. Borrmann and T. Peter (2008), Unprecedented evidence for deep convection hydrating the tropical stratosphere, *Geophys. Res. Lett.* **35,** doi**:**10.1029/2008GL033641.

Daloze, J.-F., and M. Haeffelin, 2005: Validation of SAFNWC/MSG cloud top height using ground-based lidar and radar measurements. Visiting Scientist Rep., Me´te´o-France, 37 pp.
[Available online at http://www.nwcsaf.org.]

De Coning, E., M. Koenig and J.Olivier, 2010: The combined instability index: a new very-short range convection forecasting technique for southern Africa. Available online at

http://onlinelibrary.wiley.com/journal/10.1002/%28ISSN%291469-8080/earlyview

Dell'Acqua F., and P. Gamba, 2003: Meteorological structures and pattern recognition: Modal analysis of shapes extracted from satellite images. Optical Engineering, 42, 822-829.

Dessler, A. E., 2002: The effect of deep, tropical convection on the tropical tropopause layer, *J. Geophys. Res.*, **107**, doi:10.1029/2001JD000511.

Dworak, R., J. C. Brunner, K. M. Bedka, and W. F. Feltz, 2011: Comparison between GOES-12 overshooting top detections, WSR-88D radar reflectivity, severe storm reports, and cloud-to-ground lightning. Submitted to *Wea. Forecasting*.

Evans, Jenni L., Robert E. Shemo, 1996: A Procedure for Automated Satellite-Based Identification and Climatology Development of Various Classes of Organized Convection. J. Appl. Meteor., 35, 638–652.

FAA, 2004: Review of aviation accidents involving weather turbulence in the United States, 1992-2001. National Aviation Safety Data Analysis Center, FAA Office of System Safety. Available online at: http://www.asias.faa.gov/aviation_studies/turbulence_study/turbulence_study_new.pdf

Fritz, S., and I. Laszlo, 1993: Detection of water vapour in the stratosphere over very high clouds in the tropics. *J. Geophys. Res.*, **98** (D12), 22959-22967.

Fujita, T. T. (1982), Principle of stereoscopic height computations and their applications to stratospheric cirrus over severe thunderstorms. *J. Meteor. Soc. Japan*, **60,** 355-368.

Futyan, Joanna M., Anthony D. Del Genio, 2007: Deep Convective System Evolution over Africa and the Tropical Atlantic. *J. Climate*, **20**, 5041–5060.

Gambill, L. D., and J. R. Mecikalski, 2011: A satellite-based summer convective cloud analysis over the Southeastern United States. *J. Appl. Meteorol. Climat*. Early Online Release.

Garcia Pereda, J., 2010: Algorithm Theoretical Basis Document for "High Resolution Winds". Available online at: http://www.nwcsaf.org/indexScientificDocumentation.html

Garrett, T. J., J. Dean-Day, C. Liu, B. K. Barnett, G. G. Mace, D. G. Baumgardner, C. R. Webster, T. P. Bui, W. G. Read, and P. Minnis (2006), Convective formation of pileus near the tropopause, *Atmos. Chem., & Phys.*, **6**, 1185-1200.

Gettelman, A., M. L. Salby, and F. Sassi (2002), Distribution and influence of convection in the tropical tropopause region, *J. Geophys. Res*., **107**, doi:10.1029/2001JD001048.

Guillou, Y., 2010: Algorithm Theoretical Basis Document for "Rapid Development Thunderstorms". Available online at: http://www.nwcsaf.org/indexScientific Documentation.html

Harris, R. J., J. R. Mecikalski, W. M. MacKenzie, Jr., P. A. Durkee, and K. E. Nielsen, 2010: The definition of GOES infrared lightning initiation interest fields. *J. Appl. Meteor.*

Climat. **49**, 2527-2543.

Heymsfield, G.M., Blackmer Jr., R.H., Schotz, S., 1983a. Upper level structure of Oklahoma tornadic storms on 2 May 1979, Pt. 1 radar and satellite observations. J. Atmos. Sci. 40, 1740–1755.

Heymsfield, G.M., Szejwach, G., Schotz, S., Blackmer Jr., R.H., 1983b. Upper level structure of Oklahoma tornadic storms on 2 May 1979, Pt. 2 Proposed explanation of "V" pattern and internal warm region in infrared observations. J. Atmos. Sci. 40, 1756–1767.

Heymsfield, G.M., Blackmer Jr., R.H., 1988. Satellite-observed characteristics of Midwest severe thunderstorm anvils. *Mon. Wea. Rev.* **116**, 2200–2224.

Heymsfield, G.M., R. Fulton, and J.D. Spinhirne, 1991: Aircraft overflight measurements of Midwest severe storms: Implications and geosynchronous satellite interpretations. *Mon. Wea. Rev.*, **119**, 436–456.

Hodges, K. I., C. D. Thorncroft, 1997: Distribution and Statistics of African Mesoscale Convective Weather Systems Based on the ISCCP Meteosat Imagery. Mon. Wea. Rev., 125, 2821–2837.

Honda, R., S. A. Wang, T. Kikuchim O. Konishi, 2002: Mining of moving objects from time-series images and its application to satellite weather imagery. J. Intel. Infor. Syst., 19, 79-93.

Jensen, E. J., A. S. Ackerman, and J. A. Smith (2007), Can overshooting convection dehydrate the tropical tropopause layer? *J. Geophys. Res.*, **112**, doi:10.1029/2006JD007943.

Kaltenböck, R., G. Diendorfer, and N. Dotzek, 2009: Evaluation of thunderstorm indices from ECMWF analyses, lightning data and severe storm reports. *Atmos. Res.*, **93**, 381-396. Kidder, S.Q., and T.H. Vonder Haar, 1995: Satellite Meteorology: An Introduction. Academic Press.

Knox, J. A., A. S. Bachmeier, W. M. Carter, J. E. Tarantino, L. C. Paulik, E. N. Wilson, G. S. Bechdol, M. J. Mays, 2010: Transverse cirrus bands in weather systems: A grand tour of an enduring enigma. *Weather*, **65**, 35-41.

Kummerow, C., and W. Barnes, 1998: The tropical rainfall measuring mission (TRMM) sensor package. *J. Atmos. Oceanic Technol.*, **15**, 809-817.

Lábó, E., Putsay, M., Kocsis, Z. and Szenyán, I. 2009: Cross-verification of the Rapid Developing Thunderstorm and the precipitation products of the Nowcasting and Very Short-Range Forecasting SAF. Help Desk VS Reports.

Lakshmanan, V., K. Hondl, R. Rabin, 2009: An Efficient, General-Purpose Technique for Identifying Storm Cells in Geospatial Images. *J. Atmos. Oceanic Technol*., **26**, 523–537.

Lane, T.P., R.D. Sharman, T.L. Clark, and H.M. Hsu, 2003: An Investigation of turbulence generation mechanisms above deep convection. *J. Atmos. Sci.*, **60**, 1297–1321.

Lensky, I. M., and D. Rosenfeld, 2006: The time-space exchangeability of satellite retrieved relations between cloud top temperature and particle effective radius, *Atmos. Chem. Phys.*, **6**, 2887– 2894.

Lenz, A., K. M. Bedka, W. F. Feltz, and S. A. Ackerman, 2009: Convectively-induced transverse band signatures in satellite imagery. *Wea. Forecasting*, **24**, 1362-1373.

Levizzani, V., and M. Setvák (1996): Multispectral, high-resolution satellite observations of plumes on top of convective storms. *J. Atmos. Sci.*, **53**, 361–369.

Lindsey, D. T., D. W. Hillger, L. Grasso, J. A. Knaff, J. F. Dostalek, 2006: GOES Climatology and Analysis of Thunderstorms with Enhanced 3.9-μm Reflectivity. *Mon. Wea. Rev.*, **134**, 2342–2353.

Lindsey, D.T., and L. Grasso, 2008: An effective radius retrieval for thick ice clouds using GOES. *J. Appl. Meteor. Climatol.*, **47**, 1222–1231.

Liu, C., 2007: Geographical and seasonal distribution of tropical tropopause thin clouds and their relation to deep convection and water vapour viewed from satellite measurements, *J. Geophys. Res.*, **112**, doi:10.1029/2006JD007479.

Liu, C., and E. J. Zipser, 2005: Global distribution of convection penetrating the tropical tropopause, *J. Geophys. Res.*, **110**, D23104, doi:10.1029/2005JD006063.

Machado, L. A. T., J. P. Duvel, M. Desbois, 1993: Diurnal Variations and Modulation by Easterly Waves of the Size Distribution of Convective Cloud Clusters over West Africa and the Atlantic Ocean. Mon. Wea. Rev., 121, 37–49.

Machado, L. A. T., W. B. Rossow, R. L. Guedes, A. W. Walker, 1998: Life Cycle Variations of Mesoscale Convective Systems over the Americas. Mon. Wea. Rev., 126, 1630–1654.

Machado, L. A. T., H. Laurent, 2004: The Convective System Area Expansion over Amazonia and Its Relationships with Convective System Life Duration and High-Level Wind Divergence. *Mon. Wea. Rev.,* **132**, 714–725.

Machado, L. A. T., W. F. A. Lima, O. Pinto, and C. A. Morales, 2009: Relationship between cloud-to-ground discharge and penetrative clouds: A multi-channel satellite application. *Atmos. Res.,* **93**, 304-309.

Maddox, R. A., 1980: Mesoscale convective complexes. *Bull. Amer. Meteor. Soc.*, **61**, 1374–1387.

Martin, D. W., R. A. Kohrs, F. R. Mosher, C. M. Medaglia, and C. Adamo, 2008: Over-ocean validation of the Global Convective Diagnostic. *J. Appl. Meteor. Climatol.*, **47**, 525-543.
McCann, D.W., 1983. The enhanced-V: a satellite observable severe storm signature. *Mon. Wea. Rev*. **111**, 887–894.

Mecikalski, J. R., and K. M. Bedka, 2006: Forecasting convective initiation by monitoring the evolution of moving convection in daytime GOES imagery. *Mon. Wea. Rev*. **134**, 49-78.

Mecikalski, J. R., W. M. Mackenzie, M. Koenig, and S. Muller, 2010a: Use of Meteosat Second Generation infrared data in 0-1 hour convective initiation nowcasting. Part 1. Infrared fields. *J. Appl. Meteor. Climate*., **49**, 521-534.

Mecikalski, J. R., W. M. Mackenzie, M. Koenig, and S. Muller, 2010b: Use of Meteosat Second Generation infrared data in 0-1 hour convective initiation nowcasting. Part 2. Use of visible reflectance. *J. Appl. Meteor. Climat*. **49**, 2544-2558.

Merritt, J. H., and J. M. Fritsch, 1984: On the movement of the heavy precipitation areas of mid-latitude mesoscale convective complexes. Preprints, 10th Conf. on Weather Analysis and Forecasting, Clearwater, Amer. Meteor. Soc., 529-536.

Mills, P., Astling, E., 1977. Detection of tropopause penetrations by intense convection with GOES enhanced infrared imagery. Preprints 10th Conf. Severe Local Storms. Amer. Meteor. Soc. 61–64.

Minnis, P., S. Sun-Mack, Q. Z. Trepte, F.-L. Chang, P. W. Heck, Y. Chen, Y. Yi, R. F. Arduini, K. Ayers, K. Bedka, S. Bedka, R. Brown, S. Gibson, E. Heckert, G. Hong, Z. Jin, R. Palikonda, R. Smith, W. L. Smith, Jr., D. A. Spangenberg, P. Yang, C. R. Yost, and Y. Xie, 2010: CERES Edition 3 cloud retrievals. *AMS 13th Conf. Atmos. Rad.*, Portland, OR, June 27 – July 2.

Mitrescu, C., S. Miller, J. Hawkins, T. L'Ecuyer, J. Turk, P. Partain, and G. Stephens, 2008: Near-real-time applications of CloudSat data. *J. Appl. Meteor. Climatol.*, **47**, 1982–1994.

Morel, C., and S. Senesi, 2002a: A climatology of mesoscale convective systems over Europe using satellite infrared imagery. I: Methodology. Quart. J. Roy. Meteor. Soc., 128, 1953–1971.

Morel C. and Senesi S. 2002b: A climatology of mesoscale convective systems over Europe using satellite infrared imagery. II: Characteristics of European mesoscale convective systems. Quarterly Journal of the Royal Meteorological Society. ISSN 0035-9009. Retrieved on 2008-03-02.

Negri, A. J., and R. F. Adler, 1981: Relation of satellite-based thunderstorm intensity to radar-estimated rainfall. *J. Appl. Meteor.*, **20**, 288–300.

Negri, A. J., 1982: Cloud-top structure of tornado storms on 10 April 1979 from rapid scan and stereo satellite observations, *Bull. Amer. Meteor. Soc.,* **63**, 1851–1859.

Rabin, R., S. F. Corfidi, J. C. Brunner, and C. E. Hain, 2004: Detecting winds aloft from water vapour satellite imagery in the vicinity of storms. Weather, 59, 251–257.

Reynolds, D.W., 1980: Observations of damaging hailstorms from geosynchronous satellite digital data. *Mon. Wea. Rev.*, **108**, 337–348.

Rodriguez, A., and C. Marcos, 2010: Algorithm Theoretical Basis Document for "Convective Rain Rate". Available online at: http://www.nwcsaf.org/indexScientificDocumentation.html

Rosenfeld, D., and G. Gutman (1994), Retrieving microphysical properties near the tops of potential rain clouds by multispectral analysis of AVHRR data, Atmos. Res., 34, 259– 283.

Rosenfeld, D., and I. M. Lensky (1998), Satellite-based insights into precipitation formation processes in continental and maritime convective clouds, Bull. Am. Meteorol. Soc., 79, 2457–2476.

Rosenfeld, D., and W. L. Woodley (2003), Closing the 50-year circle: From cloud seeding to space and back to climate change through precipitation physics, in Cloud Systems, Hurricanes, and the Tropical Rainfall Measuring Mission (TRMM), edited by W.-K. Tao and R. Adler, chap. 6, Meteorol. Monogr., 51, 59– 80.

Rosenfeld, D., M. Fromm, J. Trentmann, G. Luderer, M. O. Andreae, and R. Servranckx (2006a), The Chisholm firestorm: Observed microstructure, precipitation and lightning activity of a pyro-Cb, Atmos. Chem. Phys. Disc., 6, 9877–9906.

Rosenfeld, D., W. L. Woodley, A. Lerner, G. Kelman, and D. T. Lindsey, 2008: Satellite detection of severe convective storms by their retrieved vertical profiles of cloud particle effective radius and thermodynamic phase. J. Geophys. Res., 113, D04208, doi:10.1029/2007JD008600

Sander, J., N. Dotzek, and R. Sausen, 2008: First results of climate change impacts on severe convective storms over Europe. *Preprints, 24th Conference on Severe Local Storms*, Savannah, 27-31 October 2008, Amer. Meteor. Soc., Boston, 4 pp. [Available at http://ams.confex.com/ams/24SLS/techprogram/paper_142105.htm]

Schlesinger, R.E., 1984. Mature thunderstorm cloud-top structure and dynamics: a three-dimensional numerical simulation study. *J. Atmos. Sci.* **41**, 1551–1570.

Schlesinger, R.E.,1988. Effects of stratospheric lapse rate on thunderstorm cloud top structure in a three-dimensional numerical simulation. Part I: some basic results of comparative experiments. *J. Atmos. Sci.* **45**, 1555–1570.

Schmetz, J., S. A. Tjemkes, M. Gube, and L. van de Berg, 1997: Monitoring deep convection and convective overshooting with METEOSAT. *Adv. Space. Res.*, **19**, 433-441.

Scofield, R.A., 1987: The NESDIS operational convective precipitation estimation technique, *Mon. Wea. Rev.*, **115**, 1773-1792.

Scofield, R. A., R. J. Kuligowski, 2003: Status and Outlook of Operational Satellite Precipitation Algorithms for Extreme-Precipitation Events. *Wea. Forecasting*, **18**, 1037– 1051.

Setvák, M., Levizzani, V., 1992. Influences of NOAA and Meteosat Spatial Resolution on Cloud Top Observations of Deep Convective Storms. Proc. 9th Meteosat Scientific Users'

Meeting, Locarno, pp. 169–174. EUM P11, ISSN 1011-3932.

Setvak, M, R. M. Rabin, C. A. Doswell III, V. Levizzani, 2003: Satellite observations of convective storm tops in the 1.6, 3.7, and 3.9 μm spectral bands. *Atmos. Res.*, **66-67,** 607-627.

Setvak, M., R. M. Rabin, and P. K. Wang (2007), Contribution of the MODIS instrument to observations of deep convective storms and stratospheric moisture detection in GOES and MSG imagery. *Atmos. Res*., **83**, 505-518.

Setvak, M., D. T. Lindsey, R. M. Rabin, P. K. Wang, A. Demeterova (2008), Indication of water vapour transport into the lower stratosphere above midlatitude convective storms: Meteosat Second Generation satellite observations and radiative transfer model simulations. *Atmos. Res.*, **89**, 170-180.

Setvak, M., A. Sokol, D. Lindsey, K. Bedka, J. Šťástka, Z. Charvat, 2010: Study of convective storm-top features using data from the A-Train satellites. The 2010 EUMETSAT Meteorological Satellite Conference, Cordoba, Spain.

Setvak, M., D. T. Lindsey, P. Novak, P. K. Wang, M. Radova, J. Kerkmann, L. Grasso, S. Su, R. M. Rabin, J. Stastka, and Z. Charvat, 2010: Satellite-observed cold-ring-shaped features atop deep convective clouds. Atmos. Research, 97, July 2010, p. 80-96, doi: 10.1016/j.atmosres.2010.03.009.

Smith, W. L. Jr., P. Minnis, H. Finney, R. Palikonda, and M. M. Khaiyer, 2008: An evaluation of operational GOES-derived single-layer cloud top heights with ARSCL data over the ARM Southern Great Plains Site. *Geophys. Res. Lett.*, **35**, DOI: 10.1029/2008GL034275

Šťástka, J., Setvák, M., 2008. Cloud top temperature and height product of the nowcasting SAF applied to tropopause-penetrating cold-ring shaped storms. The 2008 EUMETSAT Meteorological Satellite Conference, Darmstadt, Germany. ISBN: 978-92-9110-082-8. EUMETSAT P.52, ISSN 1011-3932

Stephens, G.L., D.G. Vane, R.J. Boain, G.G. Mace, K. Sassen, Z. Wang, A.J. Illingworth, E.J. O'Connor, W.B. Rossow, S.L. Durden, S.D. Miller, R.T. Austin, A. Benedetti, C. Mitrescu, and T. CloudSat Science Team, 2002: The CloudSat mission and the A-Train. *Bull. Amer. Meteor. Soc.*, **83**, 1771–1790.

Trier, S. B., R. D. Sharman, R. G. Fovell, R. G. Frehlich, 2010: Numerical Simulation of Radial Cloud Bands within the Upper-Level Outflow of an Observed Mesoscale Convective System. *J. Atmos. Sci.*, 67, 2990–2999.

Tsakraklides, Giorgos, Jenni L. Evans, 2003: Global and Regional Diurnal Variations of Organized Convection. J. Climate, 16, 1562–1572.

Vicente, G.A. and R.A. Scofield, 1996: Experimental GOES-8/9 derived rainfall estimates for flash flood and hydrological applications, Proc. 1996 Meteorological Scientific User's Conference, Vienna, Austria, EUM P19, pp.89-96.

Vila, D. A., L. A. T. Machado, H. Laurent, I. Velasco, 2008: Forecast and Tracking the Evolution of Cloud Clusters (ForTraCC) Using Satellite Infrared Imagery: Methodology and Validation. Wea. Forecasting, 23, 233–245.

Vila, D. A., and L. A. T. Machado, 2004: Shape and radiative properties of convective systems observed from infrared satellite images. Int. J. Remote Sens., 25, 4441–4456.

Walker, J. R., J. R. Mecikalski, K. R. Knupp, and W. M. MacKenzie, Jr., 2009: Development of a land surface heating index-based method to locate regions of potential mesoscale circulation formation, *J. Geophys. Res*., **114**, D16112, doi:10.1029/ 2009JD011853.

Wang, P.-H., P. Minnis, M. P. McCormick, G. S. Kent, and K. M. Skeens (1996), A 6-year climatology of cloud occurrence frequency from SAGE II observations (1985-1990), *J. Geophys. Res.*, **101**, 29,407-29,429.

Wang, P. K. (2003), Moisture plumes above thunderstorm anvils and their contribution to cross-tropopause transport of water vapour in midlatitudes. *J. Geophys. Res.* **108** (D6), AAC 51–AAC 515.

Wang, P. K. (2007), The thermodynamic structure atop a penetrating convective thunderstorm, *Atmos. Res*., **83**, 254–262

Wiens, K.C., S.A. Rutledge, and S.A. Tessendorf, 2005: The 29 June 2000 supercell observed during STEPS. Part II: Lightning and charge structure. *J. Atmos. Sci.*, **62**, 4151–4177.

Ziegler, C.L., and D.R. MacGorman, 1994: Observed lightning morphology relative to modeled space charge and electric field distributions in a tornadic storm. *J. Atmos. Sci.*, **51**, 833–851.

Zinner, T., H. Mannstein, and A. Tafferner, 2008: Cb-TRAM: Tracking and monitoring severe convection from onset over rapid development to mature phase using multi-channel Meteosat-8 SEVIRI data. *Meteor. and Atmos. Phys*., **101**, 191-210.